Adjoint Sources, Disconnected Loops and other Fruit of Lattice QCD

Martyn Stuart Foster

Theoretical Physics
Dept. of Mathematical Sciences
University of Liverpool
Liverpool L69 3BX

This thesis is submitted in accordance with the requirements of the University of Liverpool for the degree of Doctor of Philosophy

October 1998

Acknowledgments

I would like to thank my supervisor Chris Michael for his help, support, and patience during this Ph.D. together with other members of the Theoretical Physics group at Liverpool - particularly Alan and John.

My regards also go to Jude and Clare for being helpful, friendly, having a realistic perspective on life and making the office a generally more pleasant place to be. Many thanks must go to Clare for her support and assistance particularly while writing this thesis.

I would also like to thank my parents (all of them) for their support and encouragement over the last three years.

Abstract

We undertake a comprehensive study of the gluelump mass spectrum, exploring the spin structure of the state. We use five lattice spacings from which we extract continuum values for the state splittings, with high statistics employed at $\beta = 6.0$. We conduct a low statistics study of a related and previously unexamined lattice state, which we term the adjoint meson. We find that this state is fractionally more massive than the gluelump on the lattices considered, with indications that the splitting is greater than the pion mass at $\beta = 6.0$.

We investigate a sum rule approach to determining hadronic mass dependencies on the masses of the constituent quarks. We apply this formalism to the b meson spectrum, examining the derivative taken with respect to the valence quark mass in quenched lattice QCD. Subsequently we turn our attention to the pion, and its dependence on the quark mass parameter used in full QCD simulations. Here we employ a Z_2 noise method to calculate the propagators needed to construct the relevant correlation functions. Though our determination here is different from that of finite difference methods and our calculation is one of low statistics, there is some discrepancy with the finite difference approach. We see evidence that the correlators employed yield different measurements on quenched and dynamical gauge configurations which are otherwise similar in their observables.

We employ the same Z_2 method to conduct a preliminary study of the η' meson mass in full QCD. We introduce related source pairs to minimise the variance of the disconnected loop operators that are employed. We are able to obtain estimates of the mass from a very modest number of gauge configurations and purely local operators. We did not observe any evidence of unquenching from the measurements obtained, though statistical noise dominated the signal in the region where definitive effects would be seen.

Contents

Chapter 1

QCD: A Theory of the Strong Interaction

1.1 The Strong Interaction: A Brief History

`Question: Would you believe in a theory in which isolation of the fundamental objects is all but impossible?`

The strong interaction was the name initially given to the forces that bound the atomic nucleus so tightly that it could not be explained by accepted models, despite their success in treating other observed interactions (theories of electrodynamics and the weak interactions - understood to be responsible for the neutron decay, both within and outside, the nucleus).

Following observations of cosmic rays and later with the advent of the particle accelerators many particles were seen having short lifetimes, indicating that they too were subject to interactions on the strong scale.

In the early sixties Murray Gell-Mann and Yuval Ne'eman observed that this emerging plethora of light particles could be arranged into a few multiplets that had some degree of symmetry. The eightfold way, as it was termed, indicated an approximate $SU(3)$ symmetry which could have been attributable to the underlying theory of the interaction. The observation allowed the characterisation of the spectrum through electric charge and isospin and led to predictions of as yet unseen particles, such as the Ω^- baryon which is, perhaps, the most famous.

This picture, successful as it was, did not explain the observed symmetry. In 1964 it was Gell-Mann, and independently the "charlatan" [1] George Zweig, who conjectured that the symmetry was the result of a fundamental and unseen particle that came in three types. The observed eightfold way was a result of combinations of these 'flavours' of 'quarks' which had to carry an electric charge. This charge was constrained to be in fractions - one or two thirds of the electron charge. One of these flavours was heavier or 'strange' whilst the other two were very similar (up and down for the sides of a coin). Though unacceptable at the time, the theory survived - largely through its lack of competition.

In 1972 the theory of Quantum Chromodynamics (QCD) was born. Gell-Mann proposed the addition of a new SU(3) 'colour' degree of freedom to the quarks. This was motivated by the apparent violation of the Spin and Statistics theorem in baryons that contained identical quark flavours in their ground state. It also provided a mechanism to explain the lack of arbitrary many-quark states, with only colour singlet states allowed in the form of mesons and baryons. The confinement of colour was attributable to the theory being non-Abelian in nature. The construction and study of a quantum field theory in the mould of Quantum Electrodynamics (QED) followed, though with a colour-charged mediating particle, the gluon, responsible for the strong inter-quark forces.

This formulation is attractive since it uses the same framework as the stringently tested QED. Also, with the unification of QED and the weak interaction into a single symmetry group of $SU(2) \times U(1)$, there is promise that a single theory, encompassing the electroweak symmetry group and colour $SU(3)$, may unify the three interactions in some higher energy regime.

Unlike the electroweak model however, QCD exhibits the properties of confinement and asymptotic freedom. This latter property is the statement that over short distances, such as those that exist inside a hadron or in very high energy interactions, the quarks appear to behave freely inside hadrons, seeming to have no knowledge of their strong confining forces. These properties imply that at low energies, such as those in which we live, the perturbative approach, so successful for QED, is inappropriate.

The absence of perturbation theory as a tool makes a determination of the low energy spectrum of the theory from first principles difficult. The lack of a calculable inter-quark potential makes even non-relativistic computations arduous. There is obvious need to compute the hadronic spectrum to confirm the theory as correct in describing strong interaction phenomenology. Also, in order to observe deviations of experimental measurements from the standard model behaviour, an accurate first principles theoretical prediction is necessary.

In addition to these motivations, the field theoretical description allows massive states called glueballs composed purely of the mediating 'glue'. These states, which are not easily differentiated from mesons of similar quantum numbers in experimental physics, must be accurately determined from a theoretical basis in order to identify them, or the resonances to which they contribute.

1.2 The Formulation of a Field Theory

QCD is a field theory, which models particles as excitations in the fundamental fields; a collection of spin $\frac{1}{2}$ fields which correspond to the various flavours of quarks, traditionally labelled as matter, and a spin 1 field which corresponds to the gluon, the mediating field which is analogous to the photon in QED. The theory is defined by its Lagrangian density which is given by,

$$\mathcal{L}(x) = \sum_{\text{flavours}(f)} \bar{\psi}_f(x)(i\gamma^\mu D_\mu + m_f)\psi_f(x) - \frac{1}{4}\text{Tr}F^{\mu\nu}(x)F_{\mu\nu}(x) \tag{1.1}$$

where the fields ψ_f are the quark fields with mass m_f. The fields are gauged according to the colour degree of freedom such that the Lagrangian is invariant under arbitrary and local rotations, $R(x)$, in the colour space,

$$\begin{aligned} \psi(x) &\to R(x)\psi(x) \\ \bar{\psi} &\to \bar{\psi}(x)R^{-1}(x) \\ A_\mu(x) &\to R^{-1}(x)(A_\mu(x) + \frac{i}{g}\partial_\mu)R(x) \end{aligned} \tag{1.2}$$

The covariant derivative ensures that this symmetry is respected by the Lagrangian and is defined,

$$D_\mu = \partial_\mu + igA_\mu \tag{1.3}$$

The second term in Equation 1.1 describes pure glue phenomenon in terms of the field strength tensor, $F^{\mu\nu}$, which in turn is defined from the spin 1 gauge fields, A^μ as,

$$F_{\mu\nu} = \partial_\mu A_\nu - \partial_\mu A_\nu + ig[A_\mu, A_\nu] \tag{1.4}$$

Here F and A are matrix valued quantities whose elements are described in terms of the eight generators of the $SU(3)$ group, λ defined through;

$$A_\mu = \sum_{a=1}^{8} \frac{1}{2} A_\mu^a \lambda^a \quad , \quad [\frac{\lambda^a}{2}, \frac{\lambda^b}{2}] = \frac{i f^{abc}}{2} \lambda^c \tag{1.5}$$

and A_μ^a is a vector in the gauge group. Amongst other formalisms, the theory can then be represented as a path integral [2] over these fields,

$$Z = \int \mathcal{D}_{\text{fields}} e^{i \int d^4x \mathcal{L}(x)} \tag{1.6}$$

from which observables can be recovered.

The theory of QCD exhibits several features not found in the Abelian theory of QED on which it is so closely based. These include

- Ghosts. The extra degrees of freedom in the action leads to an over counting of states which should correctly be removed by gauge fixing before applying a perturbative approach to the problem. In QED the ghost fields do not contribute to observables of the theory. The larger gauge manifold of QCD requires that they must be accounted for correctly in order to recover the correct values of observables. In the Monte Carlo approach to lattice gauge theory, such over counting is irrelevant as, in the process of measurement, we consider only weighted samples of gauge invariant quantities.

- Confinement and asymptotic freedom. As we have previously mentioned QCD exhibits a strong colour-confining force. This is manifest as a property of the renormalised coupling that becomes larger with increasing distances. Consequently perturbation theory, an expansion in this coupling, fails altogether for low energy phenomenon.

- Complex topology. The gauge manifold is much larger than that of QED. One consequent property of this is that there is no unique minima from which a perturbative expansion can take place. A perturbative solution can have no knowledge of such features, which are related to processes involving the multiple vacua. The effects of this topology are manifest in the hadronic spectrum and have been related [3] to the η' mass.

1.3 Lattice Gauge Theory

The low energy behaviour of QCD implies that a non-perturbative approach to its solution, the extraction of observables, is needed.

Lattice QCD has already demonstrated a great deal of success in determining the properties of the theory. For example the inter-quark potential is easily calculable in a quarkless (or quenched) lattice theory, and shows the expected linear rise with separation that is characteristic of confinement. Studies have been made that predict the lightest glueball mass [4], leading to the suggestion of candidates for the particle in experiments.

The development of the subject is inherently linked to the ability of modern computer systems. Recent trends are towards calculations that correctly account for fermionic degrees of freedom, in contrast to the existing background of calculations in the quenched approximation.

We begin this thesis by presenting an introduction to the field of Lattice Gauge Theory (LGT), its concepts and methods over the following four chapters. We then proceed to discuss the specific methods employed in our calculations.

In Chapters 8 and 9 we perform two calculations in the quenched approximation that are primarily of interest in certain supersymmetric phenomenologies. The first is a more accurate and extensive determination of the gluelump lattice state, an adjoint sourced purely gluonic model of the glueballino. Subsequently we make a first lattice determination of the adjoint meson, a light quark-containing relative of the gluelump. This state corresponds to a model of the R-meson within the framework of the same approximations. We explore the splitting between these two states.

In Chapter 10, we discuss a 'sum' rule approach to determining mesonic mass dependence on the constituent quark mass. We apply this to a small ensemble of quenched configurations, concentrating on the heavy-light meson in the discussion. This work is extended in Chapter 12 to include the effects of dynamical (quark containing) simulations, measuring the required correlation functions with an improved Z_2 noise source formulation. We apply this technique to gauge configurations that have dynamical quark masses around that of the strange quark.

In Chapter 11 we make a precursory study of the η' meson mass using the same noise vector method. Although this study was conducted with relatively low statistics, the techniques used were successful and indicate that a more comprehensive study will provide sufficiently accurate information about the η'. The subject is of particular interest in determining the effects of unquenching and an ongoing higher statistics study is expected to give a more precise insight into the topic.

Chapter 2

Lattice Discretisation

2.1 Introduction

In this chapter we will describe the process of discretising the continuum field theory introduced in Chapter 1 so that it can be solved using the techniques described in Chapters 5 and 6.

The path integral of QCD contains an infinite number of degrees of freedom, namely the fields $A^\mu(x)$ and $\psi(x)$, defined at every point in space-time. In addition, the exact mathematical definition of the path integral is somewhat delicate and, though formal manipulation is possible, a student of such theories will quickly find themselves juggling with infinite quantities. Our aim is to define an alternative theory that is numerically well defined, resembles its continuum counterpart in features and properties and for which, corrections arising from the approximation are understood and controlled.

The method we present involves reducing the number of degrees of freedom from infinity to a more tractable, though still large, finite number. We formulate approximants to the above fields on a discrete, hypercubic grid of finite volume, the size and spacing of which can be chosen to reflect the physical problem being studied and the computational resources available.

2.2 Wick Rotation

Before we discuss the details of the discretisation process, we will note that in order to use the stochastic methods of Chapter 5, we cannot entertain the possibilities of complex probability.

With this in mind we focus on the exponent, $is(x) = i\int d^4x\mathcal{L}(x)$, of the continuum path integral; Equation 1.6. This must be realised in our theory as a real positive definite quantity. We achieve this through Wick rotation, a process first utilised in perturbation theory as a trick in contour integration (see for example [5]).

The metric, g, of conventional Minkowski space is defined by the scalar product of two space-time vectors,

$$x^\mu x_\mu = x^\mu x^\nu g_{\mu\nu} = x^1x^1 + x^2x^2 + x^3x^3 - x^0x^0 \tag{2.1}$$

We replace the time component of vector quantities with an imaginary one τ where $\tau = -it$. τ is described in index notation as x^4 and scalar products of lattice vectors are summed by convention over indices 1 through 4.

We note that the effect of this transformation on Equation 2.1 generates a new metric,

$$g^{\mu\nu} = \delta^{\mu\nu} \tag{2.2}$$

This is the metric of a four dimensional Euclidean geometry. The Lorentz transformation operator, after the Wick rotation becomes an element of $SO(4)$, the group of four dimensional rotations.

There are some necessary conditions on a Euclidean theory for it to be meaningful. The most significant of these is that of reflection positivity - the requirement that the eigenvalues of the system are positive and real, and that meaning can be given to the observables of the system. We refer the reader to [6] for a more comprehensive discussion of this.

2.3 Variables and Quantities on the Lattice

The representation of the gauge fields can be motivated by consideration of the Aharonov-Bohm integral (Equation 2.3) which describes the phase evolution of a particle through a gauge field. $\mathcal{P}$ denotes a path ordering of the fields along the curve C;

$$e^{\mathcal{P}\int_C A^\mu(x)ds^\mu} \tag{2.3}$$

On a discrete lattice the smallest unit of translation is between two adjacent lattice sites x and $x + a_\mu$ where a is the lattice spacing and a_μ is a basis vector in the μ direction. We represent the gauge fields, following Wilson's example [7], by the phase evolution of a colour charge;

$$U_\mu(x) = e^{igaA_\mu(x)} \tag{2.4}$$

moving between these two lattice sites. The U_μ fields or 'link' variables are elements of the SU(3) gauge group. We note that by convention the link is associated with the site x and is defined in the direction of increasing μ. These links are analogous to the 'connections' or 'parallel transports' of general relativity, relating the local gauge coordinate systems of the two points. It is also worth noting that traversing the link in the opposite direction is given by;

$$e^{-igaA_\mu(x)} = U_\mu^\dagger(x) = U_\mu^{-1}(x) \tag{2.5}$$

Using this prescription, it is possible to recover values for the raw gauge potentials from Equation 2.4 as,

$$U_\mu(x) = 1 + igaA_\mu(x) - \frac{1}{2}g^2a^2A_\mu^2(x) + O(a^3) \tag{2.6}$$

In practice this is not useful in hadron spectroscopy as only gauge invariant quantities are observables of the system and these are more easily constructed from the link variables. In contrast to the gauge fields, the spinor fields, $\psi(x)$, are defined on the lattice sites.

Finally it is useful to define the lattice derivative, δ_μ. This is taken as a finite difference operator (such as that below) - many specific choices can be made without breaking the continuum properties.

$$\delta_\mu\psi(x) = \frac{\psi(x + a_\mu) - \psi(x - a_\mu)}{2a} \tag{2.7}$$

The gauge transformations on these fields are given by;

$$U'_\mu(x) = \Lambda(x)U_\mu(x)\Lambda^{-1}(x + a_\mu) \tag{2.8}$$

and

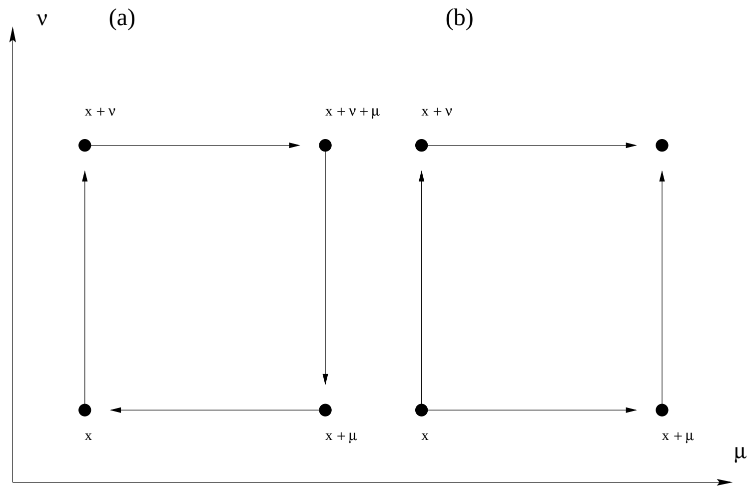

Figure 2.1: The Plaquette (a) is constructed from the link variables identified with sites as shown in (b).

$$\psi'(x) = \Lambda(x)\psi(x) \tag{2.9}$$

where the operators Λ are defined on the lattice sites and are arbitrary and independent elements of the $SU(3)$ gauge group.

2.4 Lattice Actions

From the objects defined in the previous discussion, we have the necessary ingredients to construct operators which have the correct properties, reproducing operators of continuum QCD in the $a \to 0$ limit. We first consider the path ordered product of link variables around the smallest square on the lattice, referred to as the plaquette. This is defined in the μ,ν plane, as shown diagrammatically in Figure 2.1, and given in Equation 2.10.

$$\mathrm{Tr}U_{\Box,\mu\nu}(x) = \mathrm{Tr}U_\mu(x)U_\nu(x+a_\mu)U^\dagger_\mu(x+a_\nu)U^\dagger_\nu(x) \tag{2.10}$$

It is easy to demonstrate the gauge invariance of this construct. Making a gauge transformation on an arbitrary path ordered product of links with common start and end points, we have;

$$U'_\mu(x)U'_\nu(x+a_\mu)\dots U'^{\dagger}_\rho(x) =$$
$$\Lambda(x)U_\mu(x)\Lambda^{-1}(x+a_\mu)\Lambda(x+a_\mu)U_\nu(x+a_\mu)\dots U^\dagger_\rho(x)\Lambda^{-1}(x) \quad (2.11)$$

The Λ matrices will cancel in all products except the end points. These will disappear if the trace of the product is taken, through its cyclic properties, leaving a quantity independent of the gauge transformation.

The plaquette is a product of non commuting exponentials and can be expanded using the Baker-Cambell-Hausdorff formula;

$$e^A e^B = e^{A+B+[A,B]\dots} \quad (2.12)$$

Equation 2.12, together with approximating the fields to first order in their Taylor expansion (i.e. $A_\mu(x+a_\nu) = A_\mu(x) + a\delta_\nu A_\mu(x) + O(a^2)$) reveals that;

$$\mathrm{Tr}U_{\Box,\mu\nu}(x) = e^{-iga^2 F_{\mu\nu}(x)+O(a^3)} \quad (2.13)$$

where the lattice field strength tensor is defined;

$$F_{\mu\nu}(x) = \delta_\nu A_\mu(x) - \delta_\mu A_\nu(x) + [A_\mu(x), A_\nu(x)] \quad (2.14)$$

Expanding the exponential in Equation 2.13 for the case of small a, yields;

$$\mathrm{ReTr}U_{\Box,\mu\nu}(x) = \mathrm{Tr}(1 + \frac{1}{2}a^4 F_{\mu\nu}(x)F^{\mu\nu}(x) + O(a^6)) \quad (2.15)$$

The term in $F_{\mu\nu}(x)$ has disappeared as a consequence of the tracelessness of the generators, λ, introduced in the previous chapter. We can see, by comparing this with Equation 1.1, that it is possible to construct an action that restores the continuum QCD gauge action in the limit of small a. One such choice is that shown in Equation 2.16 proposed by Wilson in 1974 [7]. Simulations made using this action are referred to as pure gauge systems.

$$S_{\mathrm{Wilson}} = \sum_x \sum_{\mu<\nu} \beta(1 - \frac{1}{3}\mathrm{ReTr}\ U_{\Box,\mu\nu}(x)) \quad (2.16)$$

Here the choice of β coincides with the QCD continuum coupling (g) before the inclusion of quantum corrections if $\beta = \frac{2N}{g}$. The factor of a^4 has been removed by summation over four spatial dimensions and N originates from the colour trace and is 3 for an SU(3) colour group.

Finally we constrain the theory to a finite volume so that the lattice will have L_μ sites in the μ dimension. In this work $L_1 = L_2 = L_3$ and lattice dimensions are given in the form $L_i^3 \times L_4$. We impose periodic boundary conditions so that,

$$U_\mu(x) = U_\mu(x + L_\nu a_\nu) \tag{2.17}$$

2.5 Lattice Units

At this point we will describe the system of units that will be used in subsequent chapters. It is inconvenient to carry factors of the lattice spacing a in expressions and, as we have seen, a does not appear explicitly in the action. It has been demoted to the status of an observable. Indeed just as in continuum physics, where the choice of natural units (where c and h are taken as equal to one) is made to simplify expressions, it is preferable to choose to describe quantities in units of a. We will call these lattice units, for example;

$$\hat{r} = \frac{r}{a} \tag{2.18}$$

$$\hat{M} = Ma \tag{2.19}$$

$$\hat{\psi}(,\hat{\bar{\psi}}) = a^{3/2}\psi(,\bar{\psi}) \tag{2.20}$$

$$\hat{\delta} = a^{5/2}\delta \tag{2.21}$$

Henceforth, we will assume that quantities are in these units and within a Euclidean framework, except where explicitly stated.

2.6 The QCD Ensemble and Regularisation

The partition function can now be written as

$$Z = \int \mathcal{D}_{\text{fields}} e^{-S} \tag{2.22}$$

We see that this resembles quite closely the formulation of the partition function of a statistical mechanics problem. The integral is a weighted sum over all possible configurations of the fields, in the case above, the set $\{U(x)\}$. We have seen through the formulation of the action that gauge invariance is retained exactly, though the Lorentz[1] symmetry has been broken. In principle it would be possible to solve a theory in this formulation by choosing a gauge invariant integration measure such as the Haar measure and integrating directly. This is reflected in the fact that the new discretised system is a quantum many body problem, with a finite number of degrees of freedom, rather than a field theory. Realistically the problem is still somewhat intractable and further approximations must be made.

We can see that making samples of the fields would provide information about the system. Indeed one could proceed by choosing samples that minimise the action. This would correspond to solving the Euler-Lagrange equations of motion and provide information about a discrete classical system. In order to study the quantum system we must make a more careful process of sampling that respects the contribution of configurations to the integral. This process of importance sampling is discussed in Chapter 5, for now we will be content to replace the integral in Equation 2.22 with a sum of our chosen configurations;

$$Z = \sum_{\text{configs}} e^{-S} \tag{2.23}$$

We have at this stage reduced the system to one that is guaranteed to provide finite numerical results for any calculations made at given lattice spacing. This has been achieved through the *regularisation* of the theory through the framework of the lattice. The lattice has imposed a scale a on the problem, that is otherwise scale free. Just as in a crystalline solid, momenta of any quanta in this scheme are limited to the first Brillouin zone,

$$P \leq \frac{2\pi}{a} \tag{2.24}$$

providing an ultra violet cut off to momentum integrals in the system. Just as in continuum field theory we must consider the implications of the physical scale we impose on the system. We consider the relationship between the lattice mass and the physical mass we are trying to measure (Equation 2.19). This together with the requirement that the physical mass has a finite continuum limit means that;

[1]Actually SO(4) and translations in a Euclidean framework.

$$\lim_{a \to 0} \hat{m}(\beta(a)) = ma + O(a^2) \tag{2.25}$$

In other words the lattice mass must also approach zero as $a \to 0$. In statistical mechanics terms, this implies that the correlation length of the system is diverging, and that a phase transition is approached. In more intuitive language the scale of features of the system has become independent of the exact details of the approximate theory. We mentioned earlier that Wilson's action is one of many possible choices. The set of lattice theories that have a phase transition with the same critical parameters in the $a = 0$ limit are said to belong to the same universality class, restoring the same physics in this limit. For a system demonstrating asymptotic freedom, such as QCD there is a fixed point in the coupling parameter at $g = 0$, where the coupling is independent of the momentum cut off, and hence we are interested in the limit of $\beta(g) \to \infty$.

In the next chapter we will proceed to include fermions and describe the lattice action with fermions present as well as some of the problems associated with their inclusion.

Chapter 3

Fermionic Fields

3.1 Introduction

In the last chapter we discussed lattice QCD in the context of gauge fields only. In this chapter we will discuss the discretisation of fermionic fields and some of the obstacles that they present. The problems described here arise ultimately from the anti-commuting nature of the fermionic field variables. Whilst the concept of anti-commuting, or Grassmann-valued, numbers is not easy to implement in computer simulations and numerical studies, these problems are further to those presented here, which are directly related to the discretisation process.

3.2 Doubling

It is fairly straight forward to write down an action containing discretised variables, such that, the continuum action is restored in the limit $a \to 0$. One such example, for a trivial free fermion theory, is;

$$S = \sum_x \bar{\psi}(x)(\gamma_\mu \delta_\mu + m)\psi(x) \tag{3.1}$$

where γ are the Euclidean space versions of the usual γ matrices of the Dirac equation and are given in Appendix A. The field variables ψ are Grassmann valued. Here there is an absence of gauge fields and the difference operator is not covariant in any sense. Although at first glance this appeared a painless process, the resultant system is quite ill behaved as an approximation to the continuum theory at all finite lattice spacings. This means that even $a \to 0$ extrapolation is meaningless.

The main feature of this action is the introduction of flavour doublers. We consider the propagator in momentum space of a continuum theory which we seek to approximate,

$$G(p) = \frac{1}{p^2 + m^2} \tag{3.2}$$

We contrast this with its equivalent in a discretised theory. We obtain this by defining a lattice Fourier transform on the fields $\psi(x)$, and rewriting Equation 3.1 in terms of the fields $\psi(p)$. We find a Green function of the form,

$$G_f(p) = \frac{-\frac{i}{a}\gamma_\mu \sin(ap_\mu) + m}{m^2 + \Sigma_\mu \frac{1}{a} \sin^2(ap_\mu)} \tag{3.3}$$

In contrast, the discretised propagator of the lattice Klein-Gordon equation corresponding to a scalar bosonic particle is;

$$G_b(p) = \frac{1}{m^2 + \Sigma_\mu \frac{1}{a^2} \sin^2(\frac{ap_\mu}{2})} \tag{3.4}$$

In Figure 3.1 we plot these functions. We can see quite clearly that the effect of discretisation on the scalar field is that at large momenta in the allowed range, the approximation is poor. However, as the continuum limit is taken, for a fixed momentum, the approximation improves. For the fermion fields extra zeros have appeared in the function at $p_\mu = \pm\frac{\pi}{a}$. These extra poles correspond to the duplication of particle states. There will be a doubling in the number of these extra states for each dimension of the system, corresponding to the 'corners' of the first Brillouin zone. These states are not removed in the continuum limit and so must be more carefully treated.

Before tackling this problem we extend Equation 3.1 to QCD by introducing the lattice covariant derivative to replace the difference operator in that expression;

$$\delta_\mu\psi \to \overrightarrow{\Delta}_\mu\psi = \frac{1}{a}(U_\mu(x)\psi(x + a_\mu) - \psi(x)) \tag{3.5}$$

This makes the expression invariant under local gauge transformations. In practice the derivative is taken as the average of acting in both left and right directions on the $\bar{\psi}$ and ψ fields respectively, here written $\overleftrightarrow{\Delta}$. Thus the naive QCD action can be written;

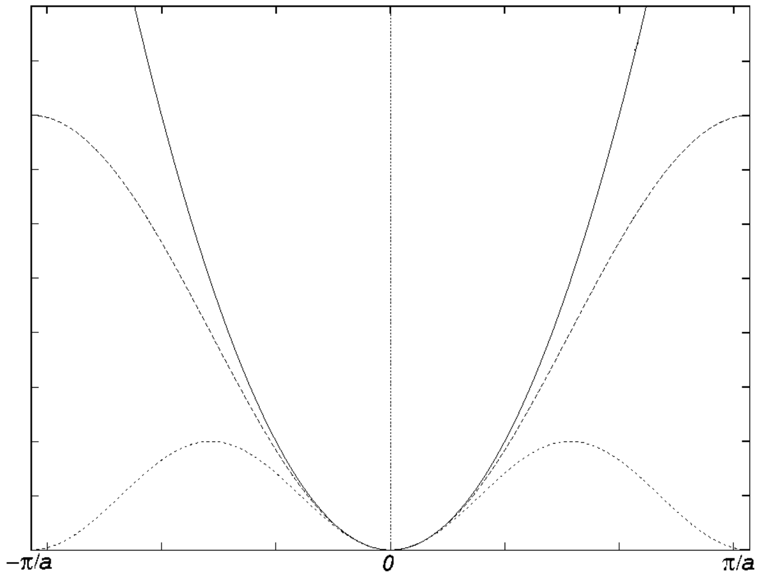

Figure 3.1: The denominator of the propagator versus momentum shown for one dimension. The curves correspond to continuum particles (solid), lattice bosons (dashed), and naive lattice fermions (dotted).

$$S = S_{\text{Wilson}} + \sum_x \psi^*(x)(\gamma_\mu \overleftrightarrow{\Delta}_\mu + m)\psi(x) \tag{3.6}$$

3.3 Wilson's Fermions

It was shown by Nielsen and Ninomiya in their famous *no-go* theorum [8] that no lattice regularisation that preserved all of the desired symmetries (including chiral and gauge symmetries), whilst maintaining the U(1) axial anomaly and locality of the action, could be found for which the doubling problem was avoided.

Several formulations of lattice QCD that deal with the doubling problem have been proposed and used successfully. One example is the non-local action of Kogut and Susskind [9] which recycle the fermion doublers as chiral pairs of different flavours. We will concentrate only on that proposed by Wilson [10] which is employed in the work described herein.

Wilson proposed the addition of an extra term to Equation 3.6 of the form;

$$-\frac{r}{2}\Sigma_{x\mu}\bar{\psi}(x)\nabla\psi x \quad (3.7)$$

Here ∇ is the Laplacian operator. The choice of $0 < r \leq 1$ is arbitrary and $r = 0$ corresponds to the naive action above. In the Fourier decomposition sketched above one finds that this term lifts the degeneracy of the unwanted states with the 'real' particle, essentially giving the doublers a mass. In the continuum limit this mass contribution is infinite and the doublers do not propagate or contribute to the spectrum of the system.

3.4 The Clover Term

Whilst the Wilson formulation of fermions above reproduces the QCD action in the continuum limit, it does so less well than the gauge counterpart of Chapter 2. At finite lattice spacing the presence of $O(a)$ artifacts that arise from the Wilson term in the fermion action makes finer grained lattices essential in order to determine the spectrum accurately. Many studies have been made in alternative actions that are better behaved at finite lattice spacings, both for the gauge and fermion parts of the theory. Such techniques include tadpole improvement [11], perfect (or fixed point) actions [12]. The effects of such improvements are compared concisely in [16] in the context of a practical application. Such techniques are beyond the scope of this discussion but we will briefly introduce the technique known as clover improvement used in subsequent calculations.

Heuristically one can understand clover improvement as adding a term that is leading order in a and reduces or removes $O(a)$ terms in the action through fine tuning. The term used in the clover action has the form,

$$-\frac{i}{4}C_{\mathrm{SW}}\Sigma_{x,\mu,\nu}\psi^*(x)\sigma_{\mu\nu}F_{\mu\nu}(x)\psi(x) \quad (3.8)$$

where $F_{\mu\nu} = \frac{1}{4}\Sigma(U_{\Box,\mu\nu}(x) - U^{\dagger}_{\Box,\mu\nu}(x))$ and the sum is over the possible choices of the plaquette with origin x as shown in Figure 3.2. This is known as Sheikholeslami Wohlert improvement [13]. The choice of C_{SW} should be made to minimise $O(a)$ errors. This coefficient can be estimated in lattice perturbation theory (e.g. tree level improvement: $C_{\mathrm{SW}} = 1$ [14]), or more fashionably using some non-perturbative technique, such as demanding the PCAC relation holds to the required order [15]. In general the value of C_{SW} is a function of the coupling β, and also changes the physical interpretation of the quark mass in the action.

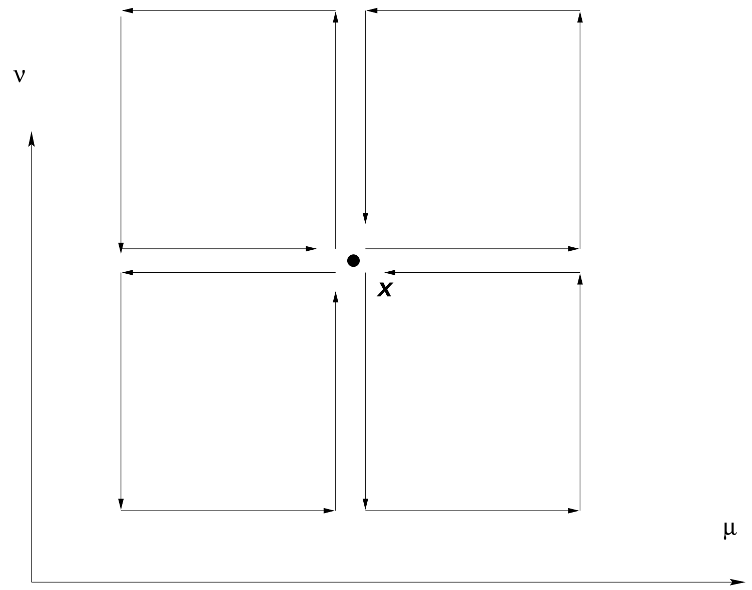

Figure 3.2: The 'Clover' sum: schematically.

3.5 The Quark Matrix

Finally we put these things together. The Clover fermion action has become a rather cumbersome expression and we will define a new mass parameter; κ

$$\kappa = \frac{1}{8r + 2m} \tag{3.9}$$

in order to write the action in a more compact form,

$$\begin{aligned} S_{C_{\mathrm{SW}}} &= \Sigma_{xy}\bar{\psi}(x)(\delta_{xy} - \kappa\Sigma_{\mu}((\gamma_{\mu}+r)U_{\mu}(x)\delta_{x(x+a_{\mu})} \\ &\quad + (\gamma_{\mu}+r)U^{\dagger}_{\mu}(x-a_{\mu})\delta_{(x-a_{\mu})x}) - \frac{iC_{\mathrm{SW}}}{4}U_{\boxplus}\delta_{xy})\psi(y) \\ &= \psi^{*}_{i}M_{ij}\psi_{j} \end{aligned} \tag{3.10}$$

In the indices i, and j we imply all relevant indices; site, colour, spin and flavour and the SU(3) matrix, $U_{\boxplus}$ is the clover expression described in Equation 3.8. M_{ij} is called the quark matrix.

We make final note that the relationship between the continuum fermion mass and the discretised version has been somewhat altered by the addition of extra terms. It is useful to define a parameter κ_C the critical value of κ for which chiral symmetry is restored, and corresponds to massless continuum fermions. κ_C must be determined by measurements of the pion mass. The pion is the massless Goldstone boson associated with chiral symmetry and by extrapolation through several choices of κ to this case, a value of κ_C may be estimated.

Chapter 4

Stochastic Simulations

4.1 Introduction

We have so far seen that it is possible to express the path integral on a discrete lattice, subject to corrections of higher orders in the lattice spacing. We have suggested that solution of the discretised integral is unnecessary provided that we sample possible configurations carefully according to their Boltzmann weights. Such probabilistically determined importance sampling methods are called 'Monte Carlo Simulations'. The term 'simulation', however, is not really applicable in this context, as we are merely approximately evaluating an integral. We will discuss in this chapter the concepts behind the Monte Carlo simulation and the requirements that make such simulations a mechanism for the correct sampling of configurations.

4.2 Quenching

Before going on to discuss the methods themselves, we will discuss the role of the fermionic fields. Simulations that treat the fermionic variables on the same footing as the gauge fields are disproportionately difficult in terms of computational implementation. This is because the variables are Grassmann valued and require a different treatment to bosonic (commuting) variables.

As discussed earlier, it is possible to integrate the discrete path integral directly. Due to the difficulty involved with Grassmann variables, we proceed by integrating the fermionic degrees of freedom out of the system directly. This leaves a partition function that contains only bosonic variables. We can then proceed to evaluate it using the methods of the next few sections.

We restate the path integral;

$$Z = \int \mathcal{D}U\mathcal{D}\bar{\psi}\mathcal{D}\psi e^{-S_{\text{gauge}}-\bar{\psi}_i M_{ij}\psi_j} \tag{4.1}$$

We can perform the integral over $\bar{\psi}$ and ψ, as shown in Appendix B, to give

$$Z = \int \mathcal{D}U \det[M(U)]e^{-S_{\text{gauge}}} \tag{4.2}$$

The simulation can now take place with an effective action, $S_{\text{eff}} = S_{\text{gauge}} - \text{Tr}\log M(U)$. Whilst the matrix $M(U)$ is large ($O(10^6)$ square for lattices with size and spacing appropriate for hadronic physics), it is sparse, containing only spatially diagonal and next to diagonal terms and can be inverted using iterative methods. As we will discuss, however, this determinant must be evaluated many times in order to generate a large enough sample of the gauge fields to make accurate measurements.

One solution to this problem is to merely neglect the fermion term in the integral by setting the determinant equal to 1. This brutal 'approximation', known as quenching, effectively removes quark pair production processes from the theory. This means that only gluonic effects are accounted for in measurements of, e.g. binding energies, and many processes are disallowed altogether such as meson/glueball mixing. It does however reduce the computational overhead by a factor of about 1000 for a given lattice dimension, making physically plausible lattices available for studying hadronic physics. This is at the expense of introducing uncontrolled systematic errors at all orders in a. The magnitude of these systematic errors is estimated to be around 15% from comparisons with experimental determinations of the spectrum. Also some required properties of the system are lost such as reflection positivity (of the quark sector) to which we have previously referred. Nevertheless a large number of studies have been made in the quenched approximation with which spectral comparisons can be made.

4.3 The Markov Chain

Returning to the main focus of the chapter, we wish to make samples of the gauge fields that are correctly weighted according to the path integral. We proceed by taking a gauge configuration and generating a new one from it according to some prescription. This chain usually starts with either a 'hot' (random), or 'cold' (uniform) lattice. The temperature label relates to the interpretation of β as an inverse temperature, and an infinitely hot system implies thermal fluctuations on a smaller scale than any other in the system. After many iterations (or updates) of this process we hope to generate a set of configurations which are in thermal equilibrium according to the coupling chosen, and uncorrelated from each other i.e. that we will have generated our set of statistically independent samples of the fields from which measurements can be made. This sequence of configurations, subject to the requirements detailed below is known as the Markov Chain.

In order to generate samples $\{U\}$, which have the correct distribution about the minimum of the action, they must be distributed with probability $P(\{U\})$;

$$P(\{U\}) = \frac{1}{Z} e^{-\beta S} \tag{4.3}$$

Here we have extracted the coupling parameter from the action to highlight its role in the process. For a system in thermal equilibrium, the probability of choosing a configuration U_A is related to the probability of choosing any other U_B by,

$$P(\{U\}_A) = \sum_{\text{All B}} P_{AB} P(\{U\}_B) \tag{4.4}$$

where P_{AB} is the matrix of probabilities of moving between two equilibrium states. From this we arrive at a sufficient condition, that of detailed balance;

$$P_{AB} e^{-\beta S_A} = P_{BA} e^{-\beta S_B} \tag{4.5}$$

We note that it is the difference between the actions associated with the two configurations $\{U\}_A$ and $\{U\}_B$ that will feature in algorithms designed to migrate us between thermalised configurations. In general any updating procedure satisfying this relationship will converge the system into equilibrium, though the efficiency of this process depends upon the particular algorithm.

There are further requirements that must be satisfied for the updating procedure to qualify as a Markov process, we list them here referring the reader to more comprehensive texts [17] for their specific discussion;

- $P_{AB} > 0$ for all configurations A and B.
- P_{AB} is a function of only A and B.

Summarily the former ensures that all regions of the configuration space are accessible to the algorithm and that the choice of initial configuration is irrelevant provided sufficient thermalisation updates are allowed. It should also be noted that although this criterion implies that the whole of the lattice must be updated simultaneously it is allowable to use an algorithm that updates variables locally, provided that some compound of these steps satisfies the condition. This distinction is referred to as strong vs. local ergodicity. The second statement implies that the trajectory of the chain through configurational space is not biased by its history.

4.4 Algorithms

Here we discuss some specific algorithms, that are employed in the generation of configurations used in subsequent calculations. In practice it is often preferable to use some combination of the algorithms in turn, due to their individual properties and computational expense.

4.4.1 The Metropolis Algorithm

The simplest of algorithms that conforms to the requirements of detailed balance is the Metropolis method [18]. A gauge configuration can simply be chosen at random by choosing link variables that are randomly distributed over the gauge manifold. The probabilistic requirements of detailed balance are imposed afterward by an accept-reject step, which either discards the new configuration or accepts it as the next one in the Markov chain. We compare the change in action $\Delta S = S(U_{\text{trial}}) - S(U_{\text{orig}})$ by comparison with a uniformly distributed random number P in the range $0 \to 1$,

$$\begin{array}{ll} \left.\begin{array}{l} \Delta S < 0 \\ 0 \leq e^{-\beta\Delta S} \leq P \end{array}\right\} & \text{Accept the new configuration} \\ e^{-\beta\Delta S} > P & \text{Reject the new configuration} \end{array} \tag{4.6}$$

It should be noted that although we do not implement the Metropolis algorithm in this way directly, the accept-reject step is a useful tool for forcing other update mechanisms into satisfying the detailed balance requirements. Also, the selection of whole trial configurations is inefficient and we note that by updating links individually, whole 'sweeps' of the lattice satisfy the ergodicity requirements.

4.4.2 The Heatbath Algorithm

The Metropolis method, though computationally simple, has a quite poor acceptance rate, with the trial links not reflecting the thermal properties of the system at all. The approach of the heat-bath algorithm is to try to distribute the new gauge variables according to the required distribution, that of Equation 4.3, which satisfies the detailed balance requirements trivially so that;

$$\int_0^P dp = \int \mathcal{D}U e^{-\beta S(U)} \tag{4.7}$$

In practice this approach requires integration over the gauge manifold for the whole lattice as shown in Equation 4.7. This is not trivial for an SU(3) gauge group where an exact solution is not known. We can however perform the update locally examining the contributions to the action of a single trial link. These contributions come only from the surrounding 'staples', products of links that form plaquettes with the subject link. In addition the update is performed on some number of SU(2) subgroups of the link in question, for which an approximate form of the integral is known. This form of the Heatbath (or pseudo-Heatbath) replacement is known as Cabibbo-Marinari updating [19]. In general where only an approximate form of the gauge integral is known the system can be corrected by including an appropriate Metropolis style reject-accept step as described above.

4.4.3 The Overrelaxation Algorithm

The overrelaxation algorithm, in contrast to the previous two, does not generate a change in the action of the system. Certainly this is of no use in thermalising a Markov chain, nor does it satisfy ergodicity, as it clearly cannot explore the full configurational space. However it does provide a service in correctly thermalised systems. In finely spaced lattices, the larger scale features involved become harder to dislodge by local Heatbath updates, and large correlations between configurations in the Markov chain occur. The (simulation) time τ, taken to obtain uncorrelated configurations becomes very large. This process is known as critical slowdown and becomes worse as the phase transition (which we have associated with continuum physics) is approached.

Overrelaxation is a form of the Metropolis update employed to combat critical slowdown. The problem can be viewed as a reluctance of the system to accept changes other than very minor rotations in the fields. For the overrelaxation method, through lack of a change in the action, acceptance is guaranteed. The replacement links are chosen to be far away in the gauge manifold from the original so that the configurations evolve rapidly through configuration space, and promote larger changes to the features of the configuration. In SU(3) the identification of such points of equal action in the gauge manifold is non trivial. In the update mechanisms used to generate gauges used here, we identify simpler SU(2) subgroups and operate the update on these individually. It is known that for SU(2) opposite points in the gauge manifold (which forms the surface of a 3-sphere) are suitable for this purpose.

In quenched lattices we employ in this thesis 4 overrelaxation sweeps are performed for every Cabibbo-Marinari Heatbath update. The updates are performed on three SU(2) subgroups which encompass all elements of the SU(3) group.

4.5 Fermions Revisited: Dynamical Fermions

We surmised earlier in this chapter that the computational expense of including the fermion determinant was great. In Monte Carlo simulations the change to the action must also include measuring the change in the action due to the determinant of Equation 4.2;

$$\Delta S_f = \mathrm{Tr}\log\frac{M(U_{\mathrm{new}})}{M(U_{\mathrm{old}})} \tag{4.8}$$

We note that the fermion matrix is not real and in practice this is corrected by simulating with a matrix $\det\tilde{M} = (\det M)^{N_f}$. This process is equivalent to a system containing N_f degenerate flavours of fermion. If N_f is even, then the reality is ensured. The dynamical systems we consider have $N_f = 2$ corresponding to up and down quarks, though at strange quark masses, due to computational limitations in the speed of solving the equations of motion (the lattice Dirac equation) for lighter quarks.

We can also use the reality of $\det\tilde{M}$ to write the matrix as

$$\det\tilde{M} = \det(M^\dagger M)^{\frac{1}{2}} \tag{4.9}$$

Simulations made with the matrix $M^\dagger M$ are pseudofermionic (read bosonic) in nature. This method is discussed more fully in Chapter 7. The specific simulation methods employed in the generation of dynamical gauges are more complex. As they are not directly related to the subject of study here, we will omit them for brevity. We refer the reader to the standard texts that discuss Hybrid Monte Carlo algorithms ([22, 23]). A discussion of the specific implementation used to generate the dynamical gauges, which we use in Chapters 11 and 12, is given in [24].

Chapter 5

Hadron Spectroscopy

5.1 Introduction

We have so far discussed the simulation of QCD on a discrete lattice and the generation of sets of configurations of the fields that accurately represent the QCD vacuum. In order to extract meaningful results from the lattice theory, we must compare its observables with those typically examined in experimental physics, namely; masses, matrix elements, the renormalised coupling and so on. In this section we will examine the process of recovering these quantities from our vacuum samples.

5.2 The Correlation Function

The observables of field theories take the form of expectation values of operators,

$$\hat{x} = \langle \Omega | X | \Omega \rangle \tag{5.1}$$

acting on the vacuum state Ω. In lattice QCD the situation is entirely analogous, the expectation values of operators can be measured directly on the samples of vacuum fields we have generated. This follows from the interpretation of the path integral as a Boltzmann probability distribution such that,

$$\begin{aligned}\langle X\rangle &= \frac{1}{Z}\int \mathcal{D}U X(U)e^{-\beta S(U)} \\ &\approx \frac{1}{N_{\text{samples}}}\sum_{\text{samples}} X(U)\end{aligned} \tag{5.2}$$

where the second line follows from the fact that the samples, $\{U\}$, are already chosen to occur with the distribution of the Boltzmann factor.

One of the most important questions to ask of the theory is, 'What is the spectrum of bound states that it contains?'. We will examine in more detail the method of extracting bound state masses.

In the continuum we expect a wave-like behaviour of particles;

$$\langle\bar{\Psi}_0|\Psi_t\rangle \propto e^{iEt} \tag{5.3}$$

In a Euclidean system the oscillations will be reduced to an exponential decay. Furthermore if the state is constrained to have zero momentum we expect the correlation between states at two different times to be,

$$\sum_x \langle\bar{\Psi}_0|O_\Psi(x,t)|0\rangle = c^2 e^{-mt} \tag{5.4}$$

where $O_\Psi(x,t)$ is some ideal operator that creates only the required state from the vacuum $|0\rangle$. In practice the situation is not so straight forward. The operator Ψ is unknown and, though tuning other arbitrary operators to have the correct properties is a useful technique, we must accommodate the fact that a chosen operator O may have overlap with other states in addition to the one of interest. In particular it will overlap with its more massive excited modes. We can insert a complete set of propagating states n into Equation 5.4 to obtain,

$$\sum_{x,x'}\langle O^\dagger(U;x,0)|n\rangle\langle n|O(U;x',t)\rangle = \sum_n c^{(n)2}e^{-m_n t} \tag{5.5}$$

The spatial sum over lattice sites for the source and sink generates a zero momentum operator as this is the lattice Fourier transform of a delta function in momentum space. The role of $c^{(n)}$ can now be regarded as a measure of the overlap between the chosen operator and the states under inspection, so that maximising $c^{(0)}$ provides the best operator for examining ground state masses.

We see that as the time extent of the correlator is taken to infinity the smallest massed state m_0 will dominate the correlation function. This is hampered by the variance of the measurements which remains constant with time, resulting in a rapidly declining signal to noise ratio. This is worse for heavier states which have a shorter correlation length. One approach to this latter case is to employ lattices with asymmetric spacings, such that the temporal spacing is shorter. We do not employ these methods as the lattices used are generated for general purposes rather than particular study of such heavy states.

5.3 Observables with Quarks

We have so far discussed operators in a very general sense. The operators we have described have been functions of $U(x)$. In general we need to construct states containing quark fields, ψ_i, where i contains both spatial and internal indices. We observe that we must perform the integral,

$$\langle \bar{\psi}_i \psi_j \rangle = \frac{1}{Z} \int \mathcal{D}U \mathcal{D}\bar{\psi} \mathcal{D}\psi \, \bar{\psi}_i \psi_j e^{-S_G - \bar{\psi} M \psi} \tag{5.6}$$

We can evaluate the fermionic part of this integral by taking derivatives of Equation 4.2 with respect to source terms for the fermion fields (as shown in Appendix B) to give (for each gauge configuration);

$$\langle \bar{\psi}_i \psi_j \rangle = M^{-1}_{ji} \tag{5.7}$$

We have found (perhaps unsurprisingly) that the result of interest is the Green function corresponding to the quark propagator. Of course the inversion of this matrix is still tricky and we discuss the methods used further in Chapter 7. Equation 5.7 can be extended trivially to pairs of independent flavours of quark, identified by their subscript u,d etc. e.g.

$$\langle \bar{\psi}_{u,i} \psi_{u,j} \bar{\psi}_{d,k} \psi_{d,l} \rangle = M^{-1}_{u,ji} M^{-1}_{d,lk} \tag{5.8}$$

The combination of propagators of similar flavour must include all possible contractions between the fields, e.g.

$$\langle \bar{\psi}_{ui}\psi_{uj}\bar{\psi}_{uk}\psi_{ul}\rangle = M^{-1}_{uji}M^{-1}_{ulk} - M^{-1}_{uki}M^{-1}_{ulj} \tag{5.9}$$

The minus sign is a result of commuting the fields and is essentially the same minus sign arising in quark loops in perturbative approaches. We see that the process of evaluating these expectation values involves inversion of the matrix $M(U)$. It is worth noting here that the measurement of these propagators examines how a quark characterised by the matrix $M(\kappa, C_{SW})$ propagates in the vacuum configurations $\{U\}$. These samples may have been generated with an unrelated action which may or may not contain fermion contributions natively. This freedom to choose the parameters of M differently at the gauge generation and measurement stages it useful. It allows us to examine the response of the observables of the system to changes in both the simulation quark mass (κ_{sea}) which contributes to vacuum loops, and the mass of the quarks introduced to the system in correlators (κ_{valance}) independently.

5.4 Correlations in Practice

We have hitherto discussed the principles of constructing a correlator function. In this section we will provide examples of how correlations are obtained in practice and some of the tricks used in improving the estimators.

5.4.1 The Interpolating Field

The creation and annihilation operators of Equation 5.5 that are used to couple to the propagating states are referred to as interpolating fields. Operators that have the correct quantum numbers (parity, charge conjugation, spin representation, flavour content etc) are suitable candidates for an interpolating field as they will overlap with the state of interest. There are however still many choices available, and indeed advantages in using more that one operator in order to retrieve more information as we shall later discuss.

Particular choices for an operator with given symmetries might reflect the physical size of the state under inspection and the energy and properties of its excited states. One technique used in this work is that of fuzzing [20]. We construct link variables that are gauge covariant replacements of the original links, and implicitly include information from choosing alternative

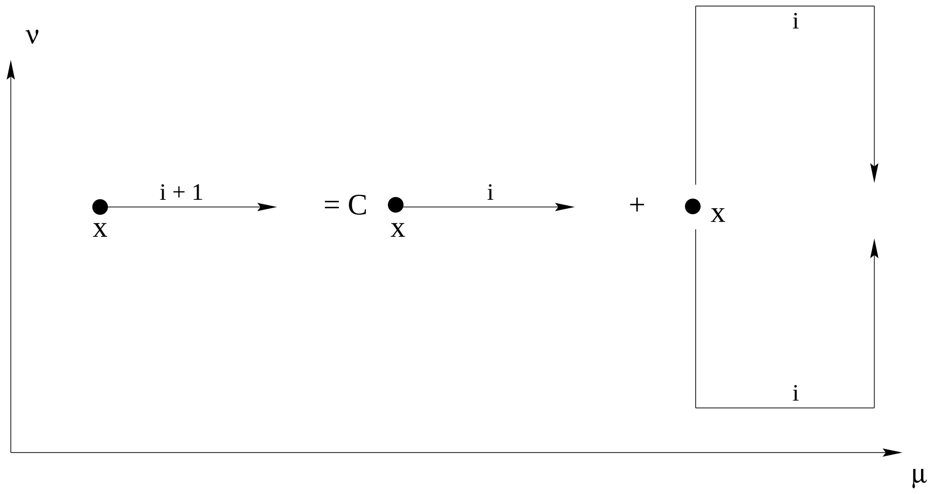

Figure 5.1: The replacement of link variables by the iterative fuzzing procedure

routes between the two points. Additionally this can be regarded as giving the link a spatial extension that might reflect the spatial distribution of the fields of interest.

The prescription for generating a fuzzed link is an iterative one as given by,

$$U_\mu^i(x) = P_{SU(3)}\left(CU_\mu^{(i-1)}(x) + \sum_\nu U_\nu^{(i-1)}(x) U_\mu^{(i-1)}(x + a_\nu) U_\nu^{\dagger(i-1)}(x + a_\mu) \right) \tag{5.10}$$

where U^0 is the original gauge link and the summation ν is implicitly taken over both positive and negative ν directions. $P_{SU(3)}$ is a projection operator that projects the sum back onto the SU(3) manifold otherwise the resulting sum will not be an SU(3) element. We see that a fuzzed link is parameterised both by the coefficient C and the number of iterations performed. The summation is shown pictorially in Figure 5.1.

5.4.2 The Representations of Lattice Symmetries

The process of discretisation, as we have discussed, breaks the general Lorentz invariance of the vacuum. One consequence of this loss of symmetry is that the degeneracy of physical particles of the system, which occur as irreducible representations of $SO(3)$ group, is also broken. Generally the $2J + 1$ degenerate continuum states are labelled J^{PC} according to their spin representation, J, behaviour under parity inversion, P, and charge conjugation C.

In lattice calculations the symmetries of the lattice, the cubic group, O are respected, together

Table 5.1: Elements of the cubic group, O and their notation

Element	Abbreviation	No. of elements
Identity	I	1
Rotation $\pm\frac{\pi}{2}$ about OX,OY,OZ	C_4	6
Rotation $\pm\pi$ about OX,OY,OZ	C_2^1	3
Rotation $\pm\pi$ about $y = x, z = 0$, and permutations	C_2^2	6
Rotation $\pm\frac{2\pi}{3}$ about $y = x = z$ etc	C_3	8

with charge and parity conjugation. The cubic group contains elements that are rotations about the various spatial axes (OX,OY,OZ) of the system as described in Table 5.1.

Particle states in lattice QCD will transform as irreducible representations of the group $O \bigotimes Z_{2,\mathrm{P}} \bigotimes Z_{2,\mathrm{C}}$ rather than the usual Legendre polynomials. There are five independent irreducible representations in the group O leading to a total of 20 independent states in this basis. The character (or trace) of elements in these representations for each of the types of rotations is given in the Character Table 5.2 and its derivation can be found in many standard group theory texts (e.g. [21]).

Operators can be constructed in the irreducible representations of $O \bigotimes Z_{2,\mathrm{P}} \bigotimes Z_{2,\mathrm{C}}$ by projecting them according to the table given in Appendix C. The effects of the two conjugation operators can be included by symmetrising the interpolating field under the actions of the operators. For example the action of Charge Conjugation on an operator is Hermitian Conjugation such that $CU_\mu(x) = U_\mu^\dagger(x)$ and in general any path ordered product of links, under the action of C, becomes the reverse path with elements $U^\dagger$. Thus a plaquette operator, for example, can be projected into a state of definite charge conjugacy,

Table 5.2: Character table of the cubic group, O.

Representation	Dimension	I	C_4	C_2^1	C_2^2	C_3
A_1	1	1	1	1	1	1
A_2	1	1	-1	1	-1	1
E	2	2	0	2	0	-1
T_1	3	3	1	-1	-1	0
T_2	3	3	-1	-1	1	0

$$
\begin{aligned}
U_{\square}^{(C=\pm)}(x) &= U_{\square}(x) \pm C U_{\square}(x) \\
&= U_{\square}(x) \pm U_{\square}^{\dagger}(x)
\end{aligned}
\tag{5.11}
$$

The breaking of the Lorentz symmetry is a result of discretisation errors. As the continuum limit is restored so is the full rotational symmetry. One expects the spectra of lattice observables to evolve smoothly toward the continuum spectra restoring the continuum degeneracies and structure. With this in mind, we construct connections between the states of O, and those of SO(3). The process is called subduction and is carried out by embedding the O group into SO(3). Each continuum representation is found to contain one or more of the cubic group representations and this connection is tabulated in Table 5.3.

One indication of the restoration of continuum physics is the recovery of the expected degeneracies in the spectrum. For example the 2 dimensional E states and 3 dimensional T_2 states with similar C and P should converge as the regularisation is removed providing a 5 fold degenerate spin 2 multiplet.

Table 5.3: Spin Content of the O irreducible representations

O Representation	Dimension	Spin Content
A_1	1	0, 4, 6, 8 ...
A_2	1	3, 6, 7, 9 ...
E	2	2, 4, 5, 6 ...
T_1	3	1, 3, 4, 5, 5 ...
T_2	3	2, 3, 4, 5 ...

5.4.3 An Example: The Wilson Loop

We turn our attention to some example operators, starting with the Wilson loop. The Wilson loop is the name given to that general form of a traced product of links forming a closed path. The simplest example of this is the plaquette which features in the Wilson action. Of particular interest is the set of rectangular paths with time extent T, and spatial extent R, given by $W(R,T)$.

$$\langle W(R,T)\rangle = \frac{1}{L^3 N_{\text{configs}}} \sum_{\text{configs,x}} \text{Tr}(\prod U)(x,R,T) \tag{5.12}$$

for products of links originating at x. We expect this to have some functional form,

$$\langle W(R,T)\rangle = c^2 e^{-E_0(R)T} + \ldots \tag{5.13}$$

where we can obtain the ground state energy by consideration of the correlation at different values of T, e.g.

$$E_0(R) = \lim_{T\to\infty} \log \frac{\langle W(R,T)\rangle}{\langle W(R,T+1)\rangle} \tag{5.14}$$

The Wilson loop operator describes the potential between two colour sources, as we will discuss later and the behaviour of $E_0(R)$ determines whether or not the system has confining properties. If $E_0(R)$ has a part proportional to R then the Wilson loop is said to obey an area law. For large R, $E_0 \sim kR$. This represents an indefinitely rising energy cost in separating the quarks, thus confining colour charged particles into bound singlet states. This is one of the simplest lattice calculations and is also one of the most important results of lattice QCD. The colour sources behave as if joined by a string with a string tension k. k is a well measured dimensionful quantity and is often used to set the scale of other lattice measurements.

5.4.4 An Example: The Pion Correlator

Our second example is that of the pion. This is the lightest bound state in lattice QCD as it is the lightest of the hadrons in continuum physics. Because of this it has a long correlation length and measurements at higher t are easily attainable.

The pion has pseudoscalar quantum numbers ($J^{PC} = J^{-+}$), as does the bilinear $\bar{u}\gamma_5 d$ where u and d denote spinor fields of different flavours. It is natural then to assume an interpolating field of the form,

$$\pi = \bar{u}\gamma_5 d \tag{5.15}$$

and a gauge invariant correlator,

$$\begin{aligned} C(t) &= \langle \sum_{x,x'} \mathrm{Tr}\left((\bar{u}(x,0)\gamma_5 d(x,0))^\dagger (\bar{u}(x'.t)\gamma_5 d(x',t)) \right) \rangle \\ &= \langle \sum_{x,x'} \mathrm{Tr}\left(\bar{d}(x,0)\gamma_5 u(x,0)\bar{u}(x',t)\gamma_5 d(x',t) \right) \rangle \\ &= \langle \sum_{x,x'} \mathrm{Tr}\left(M^{-1}_{x'x}\gamma_5 M^{-1}_{xx'}\gamma_5 \right) \rangle \end{aligned} \tag{5.16}$$

We have used the cyclic properties of the trace and the relationship, given in Equation 5.8 to obtain the last line. The trace is taken over colour and Dirac indices. Here the quark components of the pion are explicitly different flavours corresponding to a $\pi^\pm$ state. If we had stipulated a flavour singlet meson we would have had to consider the other possible contractions of the quark fields according to Equation 5.9. This is studied in Chapter 11.

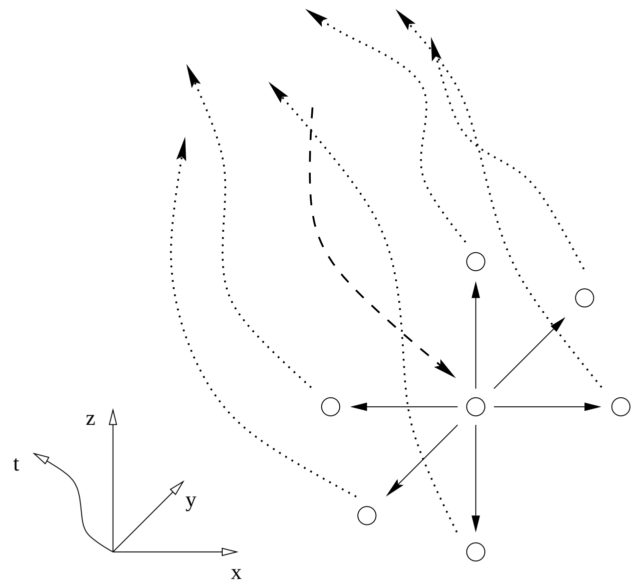

Figure 5.2: Schematic representation of a fuzzed extended operator. The dotted(dashed) curves are representations of the quark propagator sourced(annihilated) at the site indicated, whilst the solid legs are products of fuzzed gauge links. Each leg is included with a coefficient appropriate for projection into a given cubic group representation. Some components are omitted for clarity.

We notice that alternatives for the interpolating field include separating the quarks at the source and/or sink maintaining gauge invariance by the insertion of a product of gauge links between the two. A spatially extended operator such as this is suitable for projection into the O irreducible representations as described in the last section. We show this schematically in Figure 5.2. Another trick often employed is to observe that the Quark Matrix is hermitian up to factors in γ_5 so that,

$$M_{yx} = \gamma_5 M^{\dagger}_{yx} \gamma_5 \tag{5.17}$$

Then Equation 5.16 can be rewritten;

$$\begin{aligned} C(t) &= \langle \sum_{x,x'} \mathrm{Tr} M^{-1}_{xx'} (M^{-1}_{xx'})^{*} \rangle \\ &= \langle \sum_{x,x'} |M^{-1}_{xx'}|^{2} \rangle \end{aligned} \tag{5.18}$$

This is useful if the propagator is only known from one lattice site, as an approximate calculation may be made omitting the spatial sum over sources.

Chapter 6

Quark Matrix Inversion

6.1 Introduction

In the previous chapter we discussed hadron correlators that contained explicit representations of the fermionic fields. We discussed that, despite the possible absence of explicit fermion fields in the simulation, the propagation of quark containing states can still be studied by the direct evaluation of the Greens function of a discretised wave equation, in the context of specific configurations of the gauge fields.

Traditionally, due to the large computational overhead and storage requirements, the quark matrix M is inverted only in part. The lattice Dirac equation is solved for a unit source charge of single colour and spin by approximate techniques. A set of such propagators from each of the 12 spin-colour sources can be employed to construct gauge invariant operators, with perhaps, a handful of nearby sourced propagators for studies using extended operators.

For two point correlation functions, corresponding to hadrons that are light quark systems such as the pion, this approach works well. A single measurement with each propagator includes a self averaging factor, sampling the fields L^3 different sites of the correlators sink, for each time value. For the correlators discussed later in this work that use the static approximation for heavy fermions, the propagator from a unit point source makes only one such contribution, resulting in far lower statistics. In the case of disconnected loop operators, which we need to examine for the η' meson, we require a set of propagators from different sources. For cases such as these the traditional approach is inefficient. In this chapter we review the process of matrix inversion, and go on to discuss two different methods of obtaining estimates of the propagator that are more tuned to the type of calculation we wish to perform.

6.2 Matrix Inversion

The quark matrix we introduced in Equation 3.10 is connected to the expectation value of fermion bilinears as described in Equations 5.8 and 5.9. We have already discussed that the size of this complex matrix is large - $L^4 \times N_{\text{colour}} \times N_{\text{spin}}$ square for a lattice of side La. Direct evaluation of the inverse either in whole or part is certainly impractical. The sparsity of the matrix, however, makes it a good candidate for evaluating components of the inverse using iterative methods.

The propagator, G, from a source η is given by the lattice Dirac equation as,

$$MG = \eta \tag{6.1}$$

or

$$G = M^{-1}\eta \tag{6.2}$$

If the source vector is prescribed as $\eta_i = \delta_i$ then G can be explicitly seen as a single column of the matrix M^{-1} which is the unit sourced propagator described in the introduction to this chapter. We proceed to solve Equation 6.1 using some iterative algorithm, such as the Minimal Residual method (MR) which is employed in subsequent calculations, though it should be noted that other algorithms, such as the Stabilised Bi-Conjugate Gradient are more efficient in this application - we use the better known MR method for simplicity. The features of such algorithms are discussed in [25].

A general property of this type of algorithm is that convergence occurs less rapidly with increasing κ (decreasing fermion mass) which weights the off-diagonal elements, so that more realistic fermion masses are traded off against time and speed depending on the computing resources available. Hopping parameters used in this work correspond typically to strange quark masses or higher, though we may still label them up and down. Light quark values of the hadronic masses are obtained by suitable extrapolation.

6.3 Stochastic Pseudofermion Techniques

In this section we describe a well known stochastic method of obtaining estimates of the quark propagator [26], together with maximal variance reduction proposed by Michael and Peisa in [27].

We recall that the results of Gaussian integration for a general complex scalar field ϕ and positive-definite Hermitian matrix A (See Appendix B), lead to the expression,

$$\begin{aligned} \frac{1}{Z}\int\prod(d\phi^\dagger d\phi)\phi_i^\dagger\phi_j e^{-\phi^\dagger A\phi} &= \langle\phi_i^\dagger\phi_j\rangle \\ &= A^{-1}_{ji} \end{aligned} \tag{6.3}$$

The obvious similarity between the left hand side and the discretised path integral of QCD (Equation 2.22) suggests that evaluation using Monte-Carlo sampling is appropriate in order to evaluate the inverse matrix, A^{-1}. For the quark matrix, M, a Monte Carlo simulation is not directly possible as M is not a Hermitian positive definite matrix. However, we can construct a matrix $M^\dagger(U)M(U)$ that has the correct properties required for a simulation of this type. Substituting this matrix into Equation 6.3 gives;

$$\frac{1}{Z}\int\prod(d\phi^\dagger d\phi)\ \phi_i^*\phi_j e^{-\phi(M^*(U)M(U))\phi} = (M^\dagger M)^{-1}_{ji} \tag{6.4}$$

This can be tailored to our need by examining a different correlation of the bosonic (or pseudofermionic) ϕ fields such as,

$$\frac{1}{Z}\int\prod(d\phi^\dagger d\phi)(M\phi_i)^*\phi_j e^{-\phi^*(M^\dagger(U)M(U))\phi} = (M^\dagger M)^{-1}_{jk}M^\dagger_{ki} \tag{6.5}$$

We see that the correlator $\langle(M\phi_i)^*\phi_j\rangle$ is an estimator of the fermion propagator we require. In contrast to the direct solution approach, the correlation is available for all combinations of source and sink as desired. However, these naive estimators described above are rather noisy with the resulting ϕ fields having variance $O(1)$. This is compared to the conventional method, in which the Dirac equation is solved to a level of accuracy that the variance of operators between gauge configurations is huge in contrast to any systematic errors in the propagator solution. The number of samples of the ϕ fields required to accurately determine meson correlators at realistically large time values is rather large. The correlation follows an exponential decay rule as previously discussed. This implies that when the signal has fallen to $O(10^{-2})$ several thousand independent configurations need to be generated and stored n order to obtain useful measurements.

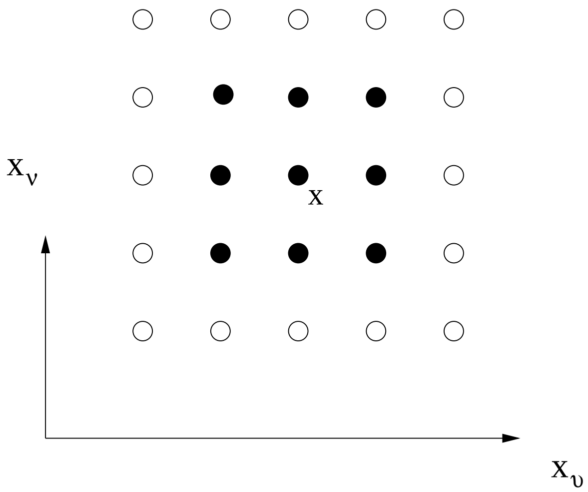

Figure 6.1: The lattice sites, marked solid, to which a given field variable, ϕ, at a site x, is connected, through the local matrix $M^\dagger M$. M contributes links to nearest neighbours so that $M^\dagger M$ potentially includes next to nearest neighbours, including those connected through an L shaped path (diagonal from the point x). Points two away do not contribute, however, due to the symmetries of M.

6.3.1 Variance Reduction

The problems of the high noise level associated with the stochastic estimators above are addressed in part by the process of Maximal Variance Reduction.

The principle of variance reduction revolves around a realization that a particular field variable, say ϕ_i may have taken any value within its manifold in a Monte-Carlo update. The probability of a field variable taking a given value is dictated by the (effective) local action, A, and the surrounding field variables to which it is coupled by the action as shown schematically in Figure 6.1.

We are free to replace any ϕ variable without bias by repeated local Monte Carlo updates generating new values for ϕ_i with probability given by;

$$P(\phi_i) \sim e^{-\phi_i^* A_{ii} \phi_i + (\phi_i^* A_{ik} \phi_{k,\mathrm{fixed}} + \mathrm{h.c.})} \tag{6.6}$$

In this expression A is the sub-matrix of $M^\dagger M$ connecting the fixed surrounding variables to the subject site, i. We can average over the replacement variables - effectively taking more samples of the fields and reducing the variance thereof. Being Gaussian in nature, Equation 6.6 can be integrated directly to give,

$$\phi_i^{\text{improved}} = -A_{kk}^{-1} A_{ij} \phi_j, \ i \neq j \tag{6.7}$$

We note that $M^\dagger M$ connects next to nearest neighbour sites. The penalty of this exercise is that the correlations between two improved sites, connected by the matrix A, are disallowed. Elucidating on this point, if one of the two sites formed part of the fixed boundary conditions to the second, the the original premise of 'fixed' is clearly invalidated. This scheme is known as a local multi-hit improvement and is discussed in [26].

In [27] it was proposed that in order to reduce the variance of large time correlations, a greater region than a single site should be subjected to the process. The lattice is partitioned into two regions, v and w and the boundary s fixed as boundary conditions to the resulting sub-lattices. The matrix $M^\dagger M$ is decomposed into parts that connect the boundary to the regions ($\tilde{A}$) and that connecting sites within a region ($\bar{A}$). Application of Gaussian integration results in an expression for the improved fields v_i,

$$v_i = -\bar{A}_{ij}^{-1} \tilde{A}_{jk} s_k \tag{6.8}$$

Thus an inversion of the matrix $\bar{A}$ is necessary for each of the samples of the fields. This is performed iteratively as described in Section 6.2 with source term, $\tilde{A}s$. The resultant field configurations can be used to construct estimators of the propagator matrix between points in each of the two regions or on the boundary, where the fields are unimproved.

The process of constructing correlators using this technique involves generating samples of the gauge fields, generating samples of the pseudofermionic fields for each gauge, and then performing a matrix inversion for each of these samples. It has been found by Michael *et al.* that 24 samples of the fields gives vastly improved estimates of heavy-light quarkonia over single propagator inversions at a cost of twice the storage and 4 times the computational requirements per gauge. The overall advantage of the method is given by Michael *et al.* to be a reduction in the error on measured quantities of 7/2 for similar computational time.

6.4 Noise Vector Sources

We mentioned in the previous chapter that fermionic correlations involving flavour singlet mesons, such as the η and η', involve contractions of the fermion fields; M^{-1}_{xx}, where the index x refers to spatial components. This type of operator, the propagator from a lattice site to itself, is also involved in the three point functions which we discuss in Chapter 11. We call these contractions disconnected loops.

Whilst the Monte-Carlo methods discussed in the previous section provide estimates of disconnected loops, the maximal variance reduction technique is of no use as correlations must be constructed between pseudofermionic fields in the same improvement region. The raw or locally improved field estimators themselves are too noisy to measure correlations of the type required. We turn instead to noise vector methods which have been employed as estimators of inverse matrix elements previously (see for example [28, 29]) and have proved effective in studies of the η'.

The general form of these disconnected loop operators is,

$$L_P(t,x_1) = \sum_{x_2} M^{-1}_{aj,bk}(x_2,x_1) P_{ab}(x_2,x_1) \Gamma_{jk} \tag{6.9}$$

where we have separated the space-time, spin and colour indices for clarity. $P_{ab}(x_2,x_1)$ is some path ordered product of link variables that spatially extends the operator. In this preliminary study we do not construct extended operators, and attempt to use other methods to remove contamination from excited states in measured quantities. The Γ matrix may be any of the 16 independent combinations of the γ matrices described in Appendix A.

We construct an extended source vector $\zeta_{bk}(x,t)$ which is zero for all sites not located on the timeslice t. Then the Dirac equation $MG = \zeta$ may be solved using the conventional techniques described in Section 6.2.

We examine constructions of the form,

$$\zeta^*_i G_j = \zeta^*_i M^{-1}_{jk} \zeta_k \tag{6.10}$$

or with specific regard to the loop operators described in Equation 6.9

$$\begin{aligned} \mathcal{L}_P &= \zeta^*_{ci}(x_3) P_{ac}(x_2,x_3) \Gamma_{ji} G_{aj}(x_2) \\ &= \zeta^*_{ci}(x_3) P_{ac}(x_2,x_3) \Gamma_{ji} M^{-1}_{aj,bk}(x_2,x_1) \zeta_{bk}(x_1) \end{aligned} \tag{6.11}$$

In general, even without the scalar product with the ζ^* term in the above equations, gauge invariance ensures that only the terms of interest contribute to $\mathcal{L}_P$, all others being noisy estimators of a gauge variant quantity, and hence have an expectation of zero. However we expect to find improved results over this method by demanding that $\mathcal{L}_P$ is independently an unbiased estimator of L_P, by using the properties of the source vector. We observe that if,

$$\langle \zeta^*_{aj}(x_1)\zeta_{bk}(x_2)\rangle = \delta_{ab}\delta_{jk}\delta_{x_1x_2} \tag{6.12}$$

then, by substitution into Equation 6.11

$$\langle \mathcal{L}_P\rangle = L_P \tag{6.13}$$

where the expectation implies an average taken with regard to evaluations with many different independent source vectors. This can be satisfied by the source vectors being taken as noise. Each element is independent and chosen randomly from a range of values that have the expectation of Equation 6.12.

6.4.1 Variance Analysis

We redefine the local observable in question; $M^{-1}_{\mu,\nu}(x,x)\Gamma_{\nu\mu}$, to be H_{ii} and have discussed that $\mathcal{L}_P$ is an estimator of H such that,

$$\mathcal{L}_P = \zeta^*_i H_{ij}\zeta_j \tag{6.14}$$

and that

$$\langle \mathcal{L}_P\rangle = H_{ii} \tag{6.15}$$

provided that the normalisation of ζ is given by Equation 6.12 where we have abbreviated our previous notation for simplicity. The variance of the estimator can be written as

$$\begin{aligned}\sigma^2_{\mathcal{L}_P} &= \langle \zeta^*_i H_{ij}\zeta_j\zeta^*_k H_{kl}\zeta_l\rangle - \langle \zeta^*_m H_{mn}\zeta_n\rangle^2 \\ &= (H_{ii}H_{jj} + H_{ij}H_{ji})_{i\neq j} + \sum_i (H_{ii}H_{ii}\langle \zeta^*_i\zeta_i\zeta^*_i\zeta_i\rangle) - (H_{ii})^2\end{aligned} \tag{6.16}$$

The second line follows by breaking down the possible arrangements of indices and using the normalisation of Equation 6.12. This variance is minimised by the choice of source vector to be elements of $Z_2 \otimes Z_2$ which removes the remaining term in ζ. Specifically the choice of ζ is defined to be,

$$\begin{aligned} \text{Re } \zeta_i &= \pm\frac{1}{\sqrt{2}} \\ \text{Im } \zeta_i &= \pm\frac{1}{\sqrt{2}} \end{aligned} \tag{6.17}$$

where the choice of sign is made randomly for each site, spin, colour, and reality index. Thus the resulting variance is given by,

$$\sigma^2_{\mathcal{L}_P} = (H_{ij}H_{ji})_{i\neq j} \tag{6.18}$$

We choose to make use of a γ_5 Hermitian basis for the Γ matrices. Thus H_{ii} is Hermitian and the reality of the operator is guaranteed overall. We can also rewrite the previous equations, giving,

$$\mathcal{L}_P = \zeta_i^*(H_{ij} + H_{ij}^\dagger)\zeta_j \tag{6.19}$$

and

$$\begin{aligned} \sigma^2_{\mathcal{L}_P} &= (H_{ij}H_{ji} + H_{ij}H_{ji}^\dagger)_{i\neq j} \\ &= (M^{-1}\Gamma M^{-1}\Gamma \pm M^{-1}\gamma_5 M^{-1}\gamma_5) \end{aligned} \tag{6.20}$$

This shows that the variance has a form identical to the mesonic correlator, which is given for the pseudoscalar case ($\Gamma = \gamma_5$) in Equation 5.16, and that contributions from terms with large spatial separation are exponentially zero. Thus the variance increases with L^3 once the lattice has reached a certain saturation size (given by the length of the correlator) rather than L^6 as one might naively have expected.

6.4.2 Variance Reduction

This Z_2 noise method entails a large number of inversions in order to obtain a reasonable signal for correlations between disconnected loops. Thus we seek to minimise the variance of the operators. We introduce a new technique with this objective in mind.

We identify the largest component of M^{-1} as being the diagonal elements (in all indices). We have discussed that the variance of the Z_2 estimators of disconnected loop terms is given by the summation of off-diagonal elements (Equation 6.18). For the cases where $H = M^{-1}\Gamma$, which we later study, these large elements are off diagonal in H, except for the case $\Gamma = 1$.

We attempt to reduce the variance of these quantities by utilising a second source related to the first as

$$\zeta' = V\zeta \tag{6.21}$$

where $V^\dagger V = 1$. Averaging over contributions from both the first and second sources gives;

$$\mathcal{L}_P = \frac{\zeta_i^*(H_{ij} + V^\dagger H_{ij} V)\zeta_j}{2} \tag{6.22}$$

The contribution of the diagonal terms in M^{-1} to the variance of the sum of the two operators behaves as, $\sigma^2_{\mathrm{diag}(M)} \sim (\Gamma + V^\dagger \Gamma V)$. If V and Γ anticommute then this contribution will vanish. For example, if we choose $V = \gamma_i$, then measurements of loops with $\Gamma = \gamma_5$ (which corresponds to an operator that creates the η' meson) will see a reduction in variance from this source.

Chapter 7

Statistical Analysis and Estimation Of Errors

7.1 Introduction

In this chapter we briefly describe the methods used in the estimation of statistical errors. We then proceed to examine the two methods employed to obtain estimates of the masses (and other quantities) and the reduction of contamination from excited state contributions at finite t correlations.

Finally we consider some of the systematic errors that are introduced when evaluating any quantity in a lattice calculation.

7.2 Estimation of Errors

The measurement of quantities using Monte-Carlo methods is subject to statistical fluctuations or noise, which unfortunately, is much more prominent in the large t region where extraction of uncontaminated masses is simpler. This noise gives rise to a measurement error on any quantities considered. For a sample of independent measurements of an observable O, the statistical error is given by,

$$\sigma(O) = \sqrt{\langle O^2 \rangle - \langle O \rangle^2} \tag{7.1}$$

and we expect the error on the mean to decrease with the number of measurements as

$$\mathrm{err}(O) = \frac{\sigma(O)}{\sqrt{N}} \tag{7.2}$$

This formula, implied by the Central Limit Theorem, relies implicitly on measurements being uncorrelated.

In practice, gauge configurations are generated from previous samples through the Markov chain. Although the auto correlation length of some trial observable, such as the plaquette, may be shorter than the separation between gauges used, the configurations may exhibit memory of other long range features. In principle we should simply separate configurations by sufficient update sweeps so that they are identifiably decorrelated. Computational limitations often prevent this. There are other factors which may also influence the interpretation of the error. An overly small sample, which does not thoroughly explore the configurational space may lead to systematic errors. Correlations in measurements from nearby timeslices may also provide misleading results (see for example [31]).

In general we use the bootstrap and jackknife procedures in order to estimate errors. These methods account for non-independent measurements, though this does not preclude effects from timeslice correlations from introducing systematic errors.

7.2.1 Bootstrap and Jackknife Analysis

Both bootstrap and jackknife (discussed in [30]) utilise a simple concept of resampling. In the jackknife case, the set of possible samples with $N-1$ data points is taken from the N measurements. In a bootstrap analysis, the corresponding set contains N elements, generated by selecting measurements randomly from the available points. Any degree of duplication in the data - including the same measurement many times, is permitted. We consider a large set of these resamples.

For the bootstrap case the error on the mean can be considered as the mean deviation of the subsamples mean from the mean of the complete data set, or;

$$\mathrm{err}(O) = \sqrt{\langle \bar{O_i}^2 \rangle - \langle \bar{O_i} \rangle^2} \tag{7.3}$$

where $\bar{O}_i$ is the mean of the ith subsample. These methods form a simple mechanism of estimating errors without making assumptions about the data distributions and correlations in the data.

7.3 The Raleigh-Ritz Variational Basis

Here we discuss a technique that allows us to extract ground state masses more effectively than simply choosing an operator and extracting masses, using Equation 5.5 directly. It is a discrete continuation of the usual Raleigh Ritz method of quantum mechanics. Bounds on eigenstates are obtained by the consideration of trial wave functions, which depend on certain parameters, a_i. Bounds can be placed on the eigenvalues of the system, such that,

$$E_0 < \frac{\langle \psi(a_i)|H|\psi(a_i)\rangle}{\langle \psi(a_i)|\psi(a_i)\rangle} \tag{7.4}$$

In lattice field theory the transfer matrix, T, is that operator which evolves the lattice fields from one time slice to the next. We consider the matrix of correlations between different creation and annihilation operators, $|O_j\rangle$ that have the quantum numbers of the state under investigation. Generally these operators differ in parameters such as fuzzing iterations and physical size. We define this correlation matrix as,

$$C_{ij}(t) = \langle O_i|T^t|O_j\rangle \tag{7.5}$$

We remind ourselves that the quantities of interest are the ratios of the correlations at consecutive time values. We note that the optimum operator path is some normalised linear combination of our measured paths $|\phi\rangle = a_i|O_i\rangle$. The ratio can then be rewritten,

$$\begin{aligned} C_{ij}(t)a_j &= \lambda C_{ij}(t-1)a_j \\ (C^{-1}(t-1)C(t))_{ji}a_i &= \lambda a_j \end{aligned} \tag{7.6}$$

where λ is the ratio evaluated at time t. We can compute the eigenvalues and eigenvectors using this equation. In practice we find the eigenvectors at small time values where C_{ij} is well defined and accurately determined. We use these eigenvectors of the operators to determine masses at larger time extents where the excited state mass content is reduced.

7.4 Data Fits

Another approach to the extraction of masses is simply to fit the data to the expected functional behaviour. This has advantages in that it allows the quotation of a single estimate and error for quantities of interest. It also uses a greater amount of the measured data rather than the variational method which uses data from only two adjacent time slices. The fitting code (originally written by C. Michael, see for example [32]) supports different models of identifying correlations. Where we have used this approach however, we have chosen the simplest method of not assuming any correlation. We use the χ^2 of the fit as a guide as to the appropriateness of the functional form used and the quality of the data.

For example, data for two-point correlations is fitted using a least squares approach to a function of the form

$$C_{ij}(t) \rightarrow \sum_k \left[c_i^{(k)} e^{-m_k t} c_j^{(k)} + c_i^{(k)} e^{-m_k (T-t)} c_j^{(k)} \right] \tag{7.7}$$

where again i,j indicate different operator paths at source and sink. The second term corresponds to the propagation of states in the negative t direction and (through the periodic boundary conditions) manifesting themselves at some time apparently in the future. For some correlations (such as where the static approximation is employed) the state cannot propagate in this manner.

We examine the χ^2 of the fit to determine the suitability of the fitted form. For example at low times the data contains large quantities of excited states. For a typical fit where, perhaps, two exponentials are considered, this data is unsuitable as it does not fit the truncated functional form. Utilising it will result in a large value of χ^2. We generally vary $T_{\min}$ used in fits tuning the value until χ^2 is minimised.

Estimation of errors on the fitted parameters are calculated by making many repeated fits to bootstrap subsamples. We then calculate the error from the distribution of these re-fit parameters.

7.5 Systematic Errors

We have previously considered statistical errors and touched upon some of the systematic errors that can arise from correlated data in the opening paragraph. Here we focus on systematic errors intrinsic to the parameters of the gauge configurations and operators that we use for measurements.

- Lattice Spacing Errors

  Discretisation errors contribute to quantities evaluated at a finite lattice spacing. Like any regularisation mechanism, the theory is expected to restore the correct theory as the cut off is removed. At the typical lattice spacings used in subsequent calculations we must identify the continuum limit by fitting data from lattices of different spacings and making some suitable extrapolation to the $a = 0$ case. For example, for a pure gauge system with the Wilson action, determinations of mass ratios are subject to $O(a^2)$ corrections. After setting the scale of quantities measured in lattice units with some other measured, dimensionful quantity, we can plot the data against some parameter with explicit a^2 dependence. This plot should exhibit linear behaviour to order $O(a^2)$. In Chapter 8 and elsewhere, we use the observable $\hat{r}_0(a)$ to eliminate explicit a dependence in measured masses and choose $\hat{r}^{-2} = r^{-2}a^2 + O(a^4)$ as the ordinate. For light quark systems the corrections are $O(a)$ as we have previously discussed. With the correct choice of the C_{SW} improvement coefficient, we expect such systems to exhibit the same errors as their pure gauge counterparts, however we employ no such dataset in our calculations.

- Finite Volume Errors

  In addition to finite lattice spacing effects we are also constrained in the size of the lattice by the computational resources required. Simulations at larger β are closer to the continuum limit but, by necessity shrink the overall physical size of the lattice for a given number of sites. We must ensure that the size of the lattice is large enough to contain the state or states investigated. We might expect the largest of the correlation lengths of the system, that of the pion to be much shorter than the dimension of the lattice. For physically realistic light quarks this would necessitate extremely large volumes compared to contemporary calculations. However attainable quark masses are heavier and volumetric requirements are consequently smaller. We can explicitly check for finite size errors by comparing the results of calculations made on lattices of identical spacing but physically different size. If no determinable differences are observed then we infer that further increases in the physical size would not have any impact on the quantities measured.

- Quenching

  The quenching process introduces a systematic and uncontrolled error. The exact contribution of the neglected quark vacuum loops in a non-perturbative regime is not known and remains a subject of much study. In principle a gradual unquenching of the theory should give insight into these errors but for Wilson/Clover type fermions no systematic study has yet been performed that details the unquenching effect. Studies with Kogut-Susskind type fermions and experimental measurements agree with errors on a 10-15% level in the quenched approximation.

- Unphysical kappa

  We are computationally constrained to performing simulations with unphysically heavy fermions, both for dynamical simulations and valence quarks. The computational cost of solving lattice equations of motion increases dramatically with decreasing mass. For valence quarks we are able to extrapolate to more physically interesting regimes as we do for the adjoint meson in Chapter 9. For dynamical simulations with Wilson/Clover fermions little is known about the chiral behaviour of the sea quarks.

- Excited states

  Whilst care is taken to maximise the removal of excited state contamination through multi-exponential fits or variational techniques, some residual contamination should be expected. For the fitting procedure we can consider adding more exponential terms to the fitting function to ensure that such an addition does not affect the predicted ground state mass. Where variational results are quoted we inspect the effective masses for a plateau as we describe in Chapter 8 ensuring that the quoted errors encompass any residual effect from higher mass contributions.

Chapter 8

The Gluelump Mass Spectrum

8.1 Introduction

The gluelump is the generic name given to the set of states that arise as a result of placing a heavy adjoint source in the gluonic vacuum.

Whilst such a source does not exist in the standard model, the spectrum is of interest both for phenomenological models of QCD, and also can be regarded as an approximation to a supersymmetric standard model state, the glueballino. The glueballino is constructed from a gluino ($\tilde{g}$) - a fermion in the adjoint representation and the supersymmetric partner of the gluon (g), together with gluonic components.

As a bound state, any estimate of the glueballino ($\tilde{g}g$) mass spectrum must be made non-perturbatively. The lattice provides a framework for such an estimate with most systematic errors being understood and physical quantities recoverable in the continuum limit.

In constructing a model of the $\tilde{g}g$ state we will make several approximations. The gluino is treated in the static limit, that is, it is considered in its infinite mass limit. We will discuss this approximation in the next section. We justify this by consideration that, in all supersymmetric models, the gluino is believed to be heavy on the scale of all standard model quanta in the system, being O(1 GeV), even in the zero bare mass case. Thus we also neglect gluino vacuum loops, expecting their contributions to be correspondingly small. We also neglect the spin degrees of freedom of the gluino treating the propagator as bosonic.

Calculations are performed in the quenched approximation as at the current time, the dynamical gauge configurations available which contain light quark vacuum effects, are believed to have little impact on the hadron spectrum as the quark masses used are heavy. We acknowledge the 10-15% systematic errors this introduces.

8.2 The Static Adjoint Source

The static approximation is well understood and often employed in studies of b meson physics - approximating the higher massed b quark. It also features in Wilson loop calculations which we discussed in Chapter 5 and will return to later in this chapter. There the static approximation is used to model the potential between two infinitely massed quark sources at fixed physical separation.

The propagator of a static fermion is the Green function of the wave equation of an infinitely heavy fermion.

$$M_{\kappa\to 0} G_f = \eta \tag{8.1}$$

Spatial derivatives of the Dirac equation can be discarded in this limit and the propagator can be written (see, for example, [22] for a detailed derivation),

$$G_f = \delta^3(x^i - x'^i) \prod_{x_4 \to x'_4} (U_4) P_\pm e^{\mp M_Q (x_4 - x'_4)} \tag{8.2}$$

where $P_\pm$ is the helicity projection operator and the sign depends on the direction of particle evolution. We note that the propagation in time of an infinitely heavy fermion is governed primarily by the path ordered product of time directed link variables between the two points.

For our heavy gluino model, we can also utilise the static approximation. We demand that the product of time-like gauge links is made with links that transform as the adjoint representation of the gauge group.

We can construct such adjoint links using the prescription;

$$U_4^{\mathrm{Adj}\ \alpha\beta} = \frac{1}{2}\mathrm{Tr}(U_4 \lambda^\alpha U_4^\dagger \lambda^\beta) \tag{8.3}$$

where the colour λ matrices are the generators of SU(3) defined as

$$[\lambda^i, \lambda^j] = 2i f_{ijk} \lambda^k \tag{8.4}$$

with antisymmetric structure constants, f, and are normalised,

$$\mathrm{Tr}(\lambda^{\alpha}\lambda^{\beta}) = 2\delta^{ab} \tag{8.5}$$

In the static limit, interactions with the gluino spin degrees of freedom, such as spin-spin and spin-orbit couplings become negligible. Hence we disregard the term $P_{\pm}$ in the propagator so that in our approximation the gluino carries no Dirac indices and should be considered bosonic. We can also expand expressions in the adjoint representations using the identity relationship,

$$\frac{1}{2}\lambda^{\alpha}_{ij}\lambda^{\alpha}_{kl} = \delta_{il}\delta_{jk} - \frac{1}{3}\delta_{ij}\delta_{kl} \tag{8.6}$$

We use this, both as an algorithmic check, and later in the chapter to examine the connection of the Wilson loop to the gluelump state.

8.3 Local Multi-hit

We have seen that correlators using the static approximation, either in the fundamental or adjoint representation involve a product of time orientated links. Such products are liable to cumulative errors from the variance intrinsic to each link. It has been found [33] that adjoint links are more susceptible to this effect.

The contribution of each link variable to the gauge action involves no other in the static propagator. As such, the time links can be subjected to a local multi-hit procedure. This was suggested by Parisi *et al.* [34] and is analogous to that which we described for scalar fields in Chapter 6. We observe that the contribution to the action of each time link is described by the six plaquettes that contain the given link. The fixed neighbouring links or 'staples', $S_{\mu=\pm1,3}$, are depicted in Figure 8.1.

Whilst analytical integration of the local action is possible in this case, for simplicity, we explicitly perform many local heat-bath updates on each of the fundamental time links, U_4 with their distribution given by,

$$\langle U_4 \rangle = \frac{1}{Z}\int \mathcal{D}U \; U_4 \; e^{\beta \sum_{\mu=1,3}(U_4 S^{\dagger}_{\mu+} + U^{\dagger}_4 S_{\mu-})} \tag{8.7}$$

We use the Cabibbo-Marinari procedure on three SU(2) subgroups of each link, generating 15 alternative fundamental links. From these we construct adjoint links as described and employ the average of these in the calculation.

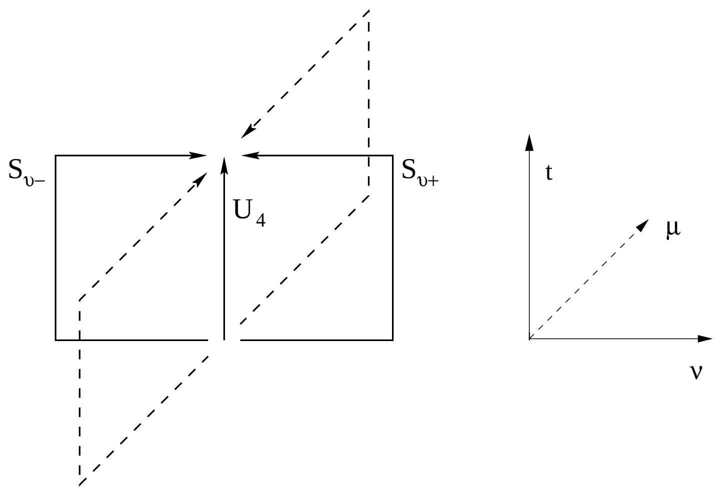

Figure 8.1: Fixed staples involved in choosing a time-link variable in a Monte-Carlo update.

8.4 Constructing the Gluelump Operator

We wish to construct operators that couple the static adjoint source to the gluonic vacuum effectively. Previous studies of the glueball [4] and gluelump spectra [35, 36, 37] have used Wilson loop-like structures in order to excite the gluonic vacuum. We follow these examples which lead, in the adjoint sourced case, to dumbell-like correlation functions.

We choose operators that are sums of these loops in irreducible representations of O_h using the projection table given in Appendix C. This allows us to both explore the spin structure of the gluelump and to improve the signal, as by definition, the operators from different representations are orthogonal and so some higher mass state contamination is removed.

We proceed by constructing untraced plaquettes $U_\Box(x)$ of various sizes which are open at the point x. They are built from links that have been 'fuzzed' according to Equation 5.10. These plaquettes are the fundamental building blocks from which we construct th operators. We form sums of the plaquettes in the required representations by considering the origin of the projection to be the point x. This results in clover-like operators which are matrices centered at x. Whilst this is computationally fast and easier to implement than a more complex structure, certain O^{PC} combinations cancel exactly due to the planar nature of the basic object. We are then left with 10 from the possible 20 observable states, details of which are presented later. We believe that these ten include the lower lying states, both from previous studies (given above and [38]), and their simpler more symmetric nature.

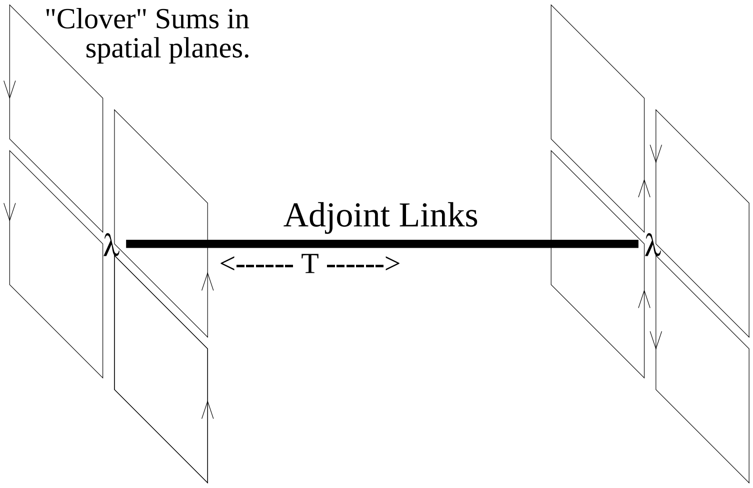

Figure 8.2: Schematic gluelump sum.

We project these clover-like operators into purely imaginary adjoint representations of definite charge conjugation using the prescription,

$$\mathcal{P}^{\alpha} = \mathrm{Tr}(\lambda^{\alpha} U_{\Box} \pm \lambda^{\alpha} U_{\Box}^{\dagger}) \tag{8.8}$$

where the sign $(\pm)$ corresponds to either positive or negative charge conjugation respectively. The complete correlation function is given by,

$$C(t = t_2 - t_1) = \sum_{x} \mathcal{P}^{\alpha\dagger}(x, t_1) \left(\prod_{t'=t_1}^{t_2-1} U_4^{\mathrm{Adj}}(x, t') \right)^{\alpha\beta} \mathcal{P}^{\beta}(x, t_2) \tag{8.9}$$

Schematically, the correlator is shown for (one spatial dimension of) the T_1^{+-} state in Figure 8.2.

8.5 Computational Details

We construct the gluelump correlator on gauge configurations of several lattice spacings, a, in order to study the lattice spacing dependence on the state. Although the raw lattice masses obtained contain an unphysical self energy (E_A) that diverges in the continuum limit, we are able to gain estimates of the continuum energy differences between the spin operators, by examining the dependence on a, of these quantities.

Table 8.1: Lattices used in calculation

β	Size	Number of lattices	Square sizes	C	Fuzzing iterations
5.7	$8^3 \times 16$	20	1,2	4.0	10,20
5.7	$12^3 \times 24$	99	1,2	4.0	10,20
5.9	$12^3 \times 24$	20	1,2	4.0	8,18
6.0	$16^3 \times 48$	202	2,3	4.0	20,30
6.2	$24^3 \times 48$	60	2,3	4.0	30,45

We construct a 4×4 matrix of correlation functions for each operator by creating different paths for the source and sink operators. We achieve this by choosing different 2 different fuzzing parameters combined with two different sizes of plaquette for the functions $\mathcal{P}^{\alpha}$. The specific choice of these parameters is tuned to give the best signal for each lattice spacing.

We detail the parameters used in the measurements together with the ensemble sizes in Table 8.1. Correlations were made for $t = 0 \to 5$ on all lattice sites and timeslices giving a self averaging factor for each gauge configurations of $L_3^3 \times L_4$ measurements of the function.

We employ the Raleigh-Ritz variational method described in Chapter 7, diagonalising the transfer matrix between $T = 0$ and $T = 1$, and using these combinations of paths to measure the spectrum at higher T values.

8.6 The Mass Spectrum

The mass spectrum is obtained by measuring the effective mass as $m_{\text{eff}}(t) = -\log\left(\frac{C(t)}{C(t-1)}\right)$ for the calculated operator eigenvectors. We inspect these results for a plateau. That is, we examine the effective masses at increasing time values. We determine the point at which the increasing measurement noise implies that higher t measurements of m_{eff} provides no statistically significant different estimate of the mass. We assume that at this point mass estimates are largely free from systematic errors from higher mass state contamination.

In Table 8.2 we present the raw lattice masses from $t = 2 \to 4$ where such determination was possible.

Table 8.2: Gluelump effective masses in lattice units.

O^{PC}	β	$t = 2$	$t = 3$	$t = 4$
T_1^{+-}	$5.7(8^3)$	1.731(22)	1.655(51)	1.545(160)
	$5.7(12^3)$	1.844(6)	1.816(15)	1.805(49)
	5.9	1.441(18)	1.476(18)	1.306(10)
	6.0	1.339(3)	1.329(5)	1.326(5)
	6.2	1.152(2)	1.142(3)	1.145(3)
T_1^{--}	$5.7(8^3)$	1.961(42)	1.842(106)	
	$5.7(12^3)$	2.099(7)	2.004(29)	2.057(137)
	5.9	1.604(16)	1.568(29)	1.351(61)
	6.0	1.505(2)	1.486(4)	1.486(8)
	6.2	1.276(3)	1.261(5)	1.247(8)
T_2^{--}	$5.7(8^3)$	2.143(38)	2.221(168)	
	$5.7(12^3)$	2.243(11)	2.268(52)	2.14(296)
	5.9	1.737(30)	1.730(37)	1.518(128)
	6.0	1.593(2)	1.579(4)	1.549(10)
	6.2	1.346(3)	1.331(7)	1.322(14)
E^{+-}	$5.7(8^3)$	2.256(64)		
	$5.7(12^3)$	2.489(16)	2.256(84)	1.689(431)
	5.9	1.974(17)	1.815(117)	1.068(187)
	6.0	1.759(3)	1.735(8)	1.744(22)
	6.2	1.469(4)	1.452(9)	1.451(23)
A_2^{+-}	$5.7(8^3)$	2.742(164)		
	$5.7(12^3)$	2.554(26)	3.123(457)	
	5.9	1.996(35)	2.440(368)	
continued ...				

... continued				
O^{PC}	β	$t=2$	$t=3$	$t=4$
	6.0	1.779(4)	1.775(13)	1.684(33)
	6.2	1.499(6)	1.477(9)	1.460(28)
A_1^{++}	5.7(8^3)	2.307(149)		
	5.7(12^3)	2.334(48)	2.515(288)	
	5.9	1.958(58)	1.827(124)	
	6.0	1.786(5)	1.762(16)	1.721(48)
	6.2	1.502(7)	1.457(15)	1.474(41)
E^{++}	5.7(8^3)	2.632(211)		
	5.7(12^3)	2.654(75)		
	5.9	2.215(67)	2.263(223)	
	6.0	1.936(6)	1.883(16)	1.927(60)
	6.2	1.603(6)	1.575(14)	1.563(28)
T_1^{-+}	5.7(8^3)	2.988(181)		
	5.7(12^3)	1.873(513)		
	5.9	2.158(48)	1.867(77)	1.241(314)
	6.0	1.966(4)	1.918(14)	1.918(45)
	6.2	1.641(5)	1.613(11)	1.599(34)
T_2^{-+}	5.7(8^3)	2.711(138)		
	5.7(12^3)	3.118(48)		
	5.9	2.379(81)		
	6.0	2.085(5)	2.057(18)	2.216(104)
	6.2	1.727(5)	1.698(18)	1.683(46)
T_2^{++}	5.7(8^3)	3.131(217)		
	5.7(12^3)	2.142(138)		
	5.9	2.307(43)	1.666(133)	1.876(506)
	6.0	2.148(5)	2.130(18)	2.142(98)
	6.2	1.788(6)	1.700(20)	1.749(81)

In Figure 8.3 we show the spectrum of states calculated at $\beta = 6.0$, which is the most accurately determined spectrum of the lattice spacings examined. We use $m_{\text{eff}}(t)$ where the data has reached a plateau as described above. It should be noted that although the masses have rather

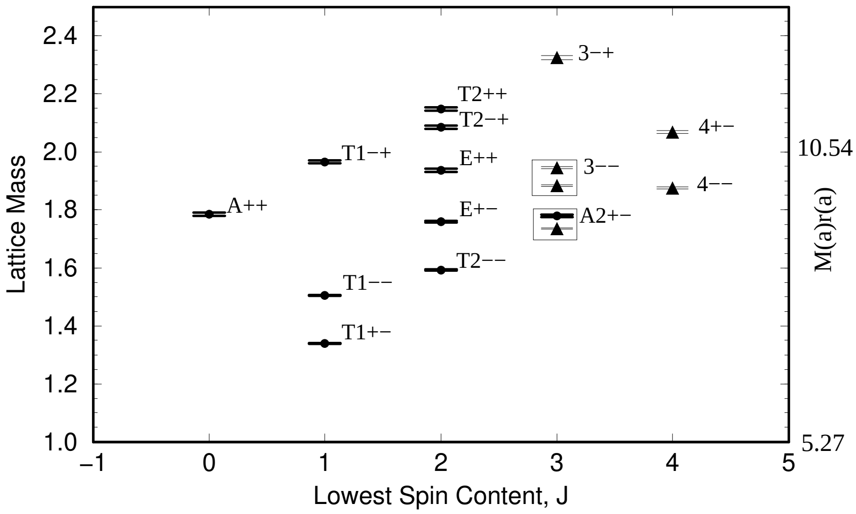

Figure 8.3: Gluelump spectrum at $\beta = 6.0$

low errors, finite lattice spacing effects, imply that this structure is not a priori, carried through to the continuum spectrum. For example, as we discussed in Chapter 5, the T_2^{++} and E^{++} states which are expected to be degenerate in this limit are separated at $\beta = 6.0$ by around 400MeV. The points marked with circles are the lowest eigenvalues of the ten measured representations from the variational analysis. They are plotted against J assuming the lowest spin contained in the O_h representation, as give in Table 5.3.

The points marked with a solid triangle are masses corresponding to higher eigenvalues from the variational analysis. With an infinitely large basis for the correlation matrix, these eigenvalues correspond exactly to other eigenstates of the transfer matrix, higher spin representations or radial excitations. In a finite basis we expect a correlation between the excited states of the system and our eigenvalues - though with increasing contamination from other higher states. We have assumed that there is a trivial relationship between the continuum spin values and the mass ordering of these states and have shown them as spin excitations as they appear consistent with that hypothesis. We include these values for illustrative purposes to give indication of the continued spectrum. We see that with our 4×4 basis there is close correspondence between estimates from different operators (boxed), with evidence of systematic errors $O(2\%)$ in using second eigenvalues from the analysis.

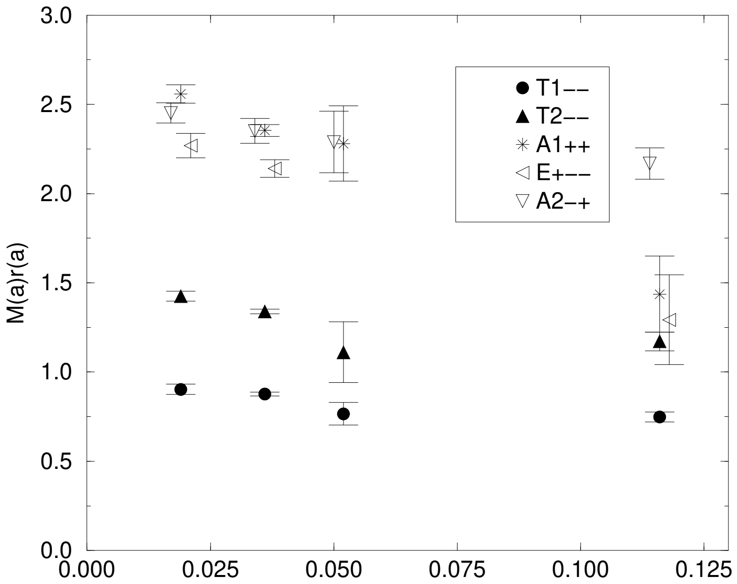

Figure 8.4: Lattice spacing dependence of the spectra. The mass splitting from the ground state is shown scaled by $r_0(a)$. The abscissa is $r_0^{-2}(a)$ in lattice units which behaves as $a^2/r_0^2(0)+O(a^3)$ including the lattice spacing explicitly.

We extrapolate the mass differences in the spectrum to the continuum limit. We scale the obtained lattice masses by $r_0(a)$ [39], where as a length in lattice units, we expect that the product should be free of explicit a dependences. r_0 is defined from the force between static quarks as $F(r_0)r_0^2 = 1.65$, corresponding to about $\frac{1}{2}$fm. At finite lattice spacing this is determined from Wilson loop calculations. Several accurate calculations of the quantity have been undertaken. We use values that have been interpolated between determinations from various sources and lattice spacings. The interpolated values agree well with measurements by Sommer *et al.* [40] where comparison is available. We perform a fit to $(M(a) - M_{T+-}(a))r_0(a)$ versus $r_0^{-2}(a)$ which we expect be linear for small a. This data is shown in Figure 8.4. The values of r_0 used are given in Table 8.3 while estimates of the continuum mass splittings are given in Table 8.4.

8.7 The Thin Wilson Loop Connection

The Wilson Loop was introduced in Section 5.4.3 as a method of determining whether the theory has confining properties. It models two heavy quarks at fixed separation using the same static

Table 8.3: Interpolated values of r_0 used to set the mass scale.

β	$r_0(a)$	$r_0(a)$ (From [40])
5.7	2.940	2.922(1)
5.9	4.402	-
6.0	5.272	-
6.2	7.319	7.380(26)

Table 8.4: Continuum Limit estimation of the $O^{PC} - T_1^{+-}$ mass splitting.

State	$\Delta(Mr_0)_{a=0}$	Energy(MeV)	χ^2/DoF
T_1^{--}	0.933(18)	368(7)	0.874
T_2^{--}	1.438(25)	584(10)	1.749
E^{+-}	2.467(92)	973(36)	0.312
A_2^{+-}	2.468(60)	972(24)	0.113
A_1^{++}	2.771(72)	1092(28)	0.137

approximation with which we constructed the heavy gluino propagator.

The spatial links of the Wilson loops can be cast into irreducible representations of the group D_{4h}. This group is the subgroup of O_h that arises by demanding a preferred axis. In this application the preferred axis is that of the quark separation. The projections onto D_{4h} represents the construction of operators with a pair of quarks in the presence of a spin excited gluonic field. Such a spectrum has been widely studied [42, 43, 44]. In this section we examine the connection between these excited Wilson loops and the gluelump spectrum we have obtained.

The continuum group associated with D_{4h} is the group $D_{\infty h}$ and the states of this group are labelled for their spin content Σ, Π, Δ etc about the preferred axis J_z. They carry a label, g, or u, corresponding to CP being ± 1 and an additional label for the one dimensional Σ states given by $P(-1)^J$. The connection between the gluelump J^{PC} and the $D_{\infty h}$ representations is given in Table 8.5

Using the relationship of Equation 8.6 we can expand the products of λ matrices in the gluelump correlator function. This yields a sum of two fundamentally traced correlation functions and is shown pictorially in Figure 8.5. Here the circled line is the adjoint traced gluino propagator and the left hand side is a fundamental dumbell-like structure that can be considered to be an excited Wilson loop at the point $R = 0$. We can see that this 'thin' Wilson loop must have mass content as described by the Equation 8.10. The other term is a glueball correlator. The glueball is a colour singlet state and corresponds to the propagation of a bound state of gluons.

$$\lim_{R\to 0} W(R,t) = ce^{-M_{\text{gluelump}}t} + \frac{1}{3}c'e^{-M_{\text{glueball}}t} \tag{8.10}$$

The masses described correspond to excited states described by the operators involved. At large time, the lighter mass of the glueball and gluelump will dominate contributions to the thin Wilson loop. The dominant state will vary, both with particular spin representations and lattice spacing. However for the lowest lying excited states at the lattice spacings considered, we see that the lighter gluelump will feature.

Although the above group relationships between the O_h and $D_{\infty h}$ groups indicate the expected behaviour of the excited gluonic potentials at small R, the limit as $R \to 0$ of the excited gluonic potential is not trivial to extract from lattice data with $R = a,\ R = 2a, \ldots$. In particular as data at $R = 0$ is not available (often $R = 1$ is also omitted for technical reasons), the small R ($R < 1$) behaviour is not immediately apparent.

Table 8.5: Connection between gluelump J^{PC} and two-body potential as $R \to 0$.

Gluelump J^{PC}	Two-body potential states
1^{+-}	Π_u, Σ_u^-
1^{--}	Π_g, Σ_g^+
2^{--}	Π_g, Σ_g^-, Δ_g

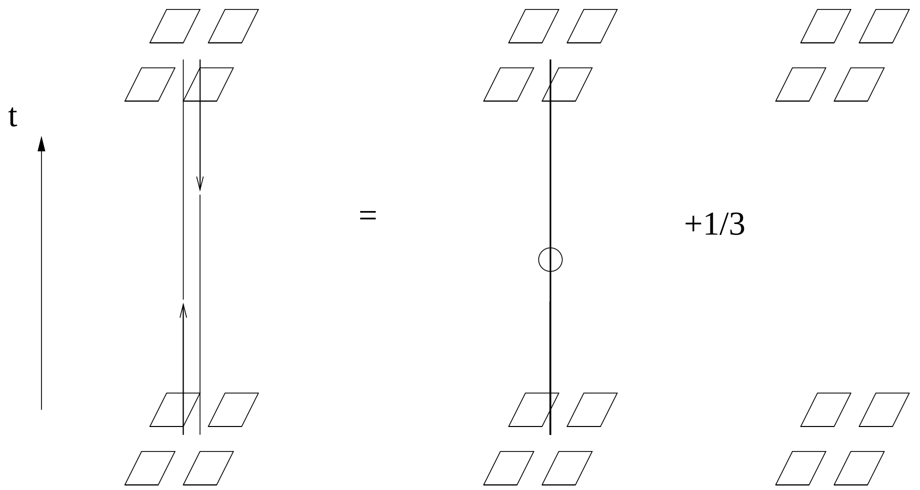

Figure 8.5: Gluelump decomposition: The diagrams represent Wilson loop (at R=0), gluelump (octet), and glueball (singlet) correlators from left to right.

Table 8.6: Comparison between SU(2) Wilson loop data (E_u) with previous calculations of the gluelump in SU(2) at $\beta = 2.4$

Gluelump mass	Wilson loop data for the E_u state		
(T^{+-})	$R = 1$	$R = 2$	$R = 3$
1.558(26)	1.381(6)	1.322(5)	1.310(4)

We examine further theoretical arguments to predict the small R behaviour of the potential. We consider one gluon exchange contributions to the self energies of the static adjoint source compared to the two fundamental sources of the Wilson loop. The self energies of the static sources E_A (adjoint) and E_F (fundamental) are not equal. Examination of the self energies at the lowest order indicates that the difference arises as $E_A = \frac{9}{4}E_F$ so that, accounting for both fundamental sources, there will be a mismatch in the self energies of the system of $\frac{1}{8}(2E_F)$. This indicates that the potentials must take an upturn to match at $R = 0$

This is evident from various data available ([44] for example). Another approach is to consider that in the decomposition described, the gluonic fields must exist in either adjoint or singlet (for the glueball) representations. Consequently in the former case the static quarks must also form an adjoint representation so that the system can form a colour singlet overall. The Coulombic interaction for states bound into an adjoint state is given to one gluon exchange level as $-\frac{1}{8}$ that of the singlet binding. This arises from consideration of the gluon exchange diagrams that we discuss in the next chapter and are depicted in Figure 9.1. For the trivial ground state representation the small R behaviour is approximately given by $-0.25/R$ from quenched lattice studies. So we might expect a rise $\sim 0.03/R$ as $R \to 0$.

Lattice data for the E_u representation for small R from SU(2) colour studies [41] at $\beta = 2.4$ do qualitatively support these estimates and are consistent with a limit as $R \to 0$ which agrees with the lattice gluelump energy [37] and is given in Table 8.6.

In Figure 8.6 we show data from various lattice regularisations which demonstrates the group-

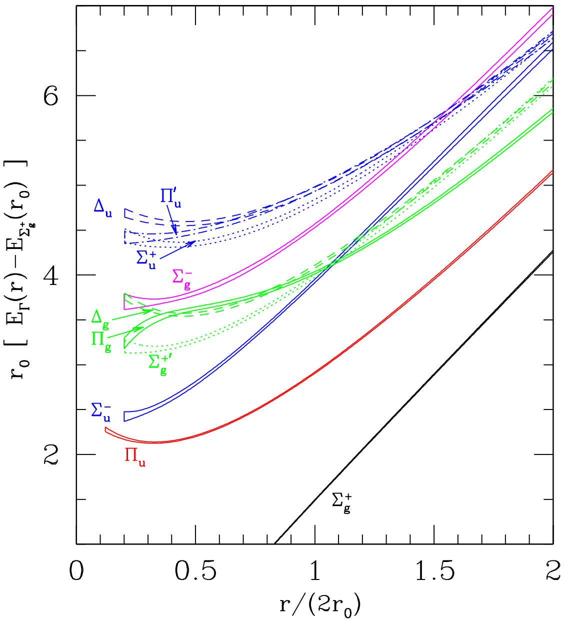

Figure 8.6: Lattice potentials from various lattice regularisations. Taken from Morningstar [44]

ing of the Wilson loop states as we have described for small R. This data is not directly comparable with our own as the contribution to the masses of the self energy is dependent on the lattice regularisation (β etc). The differences between states is comparable when scaled by appropriate dimensionless quantities however, and this agrees with our own data for the gluelump energy differences.

We compare the gluelump spectrum at $\beta = 6.2$ with the corresponding Wilson loop data in SU(3), (taken from [43]) and shown in Figure 8.7. Although the data at $R = 1$ is not available from this source, the two states shown Π_u and Σ_u^- (E_u and A_{1u}) clearly converge as $R \to 0$ and an upturn toward the lowest (T^{+-}) gluelump state is apparent.

8.8 Conclusions

We have performed an accurate determination of the gluelump spectrum using several lattice regulators, and determined continuum limit mass splittings between the six lowest states in quenched QCD.

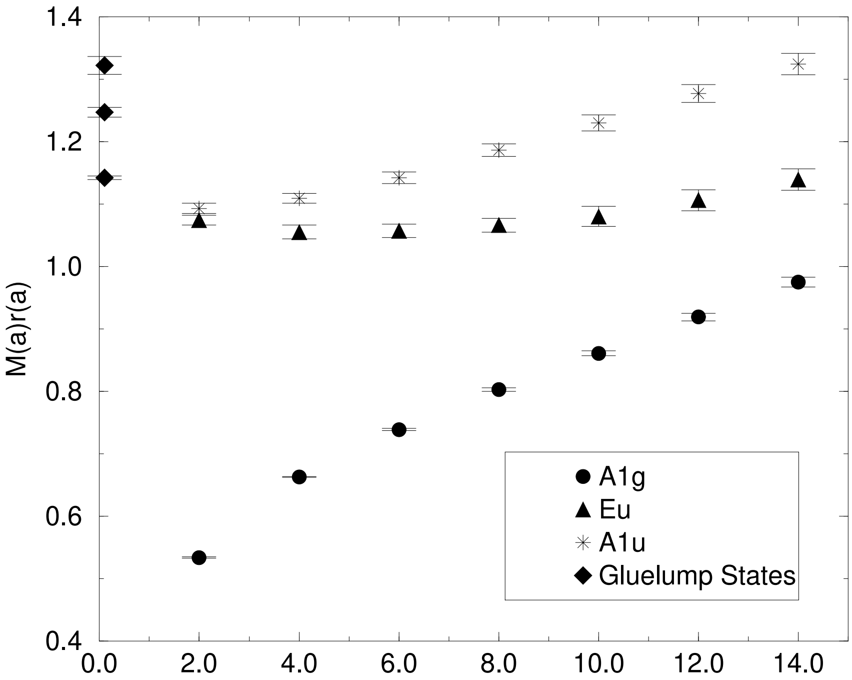

Figure 8.7: The static Quark potential at $\beta = 6.2$. The leftmost points are the gluelump energies for the T_1^{+-}, T_1^{--}, and T_2^{--} states in ascending order. The abscissa is the spacing between the static quarks in lattice units.

The spectrum agrees with previous determinations [36] at $\beta = 5.7$ of the lowest two states, supporting the assertion of the T^{+-} being the lightest state. We provide a lower estimate, which is an upper bound, for the ground state using a larger ensemble than in this previous calculation. This might be attributable to a better choice of operators and a larger basis.

We have compared our results with available data for the two body potential, obtained through Wilson loop calculations. We have determined that for such spin representations where the gluelump is lighter than the glueball, the excited two body potential states can be related to the gluelump spectrum in the limit of small quark separations. Direct comparisons between the gluelump spectrum and Wilson loop data using the same lattice regularisation upholds this hypothesis, though in the general case, the regularisation dependent self energies must be subtracted before comparisons between scale independent potentials can be made.

Chapter 9

The Adjoint Meson Spectrum

9.1 Introduction

We discuss a second state with an adjoint source, the adjoint meson. This is a bound colour singlet state of the same static adjoint source, used in the previous chapter, and a quark - antiquark bilinear, also bound in the adjoint. This state might be regarded as a model of the supersymmetric $\tilde{g}q\bar{q}$ system (that has been referred to as the R-meson [45]), in the same manner that the gluelump can be considered the infinite gluino mass limit of the glueballino. It also could perhaps be referred to as a hybridino for its similarity to the $gq\bar{q}$ system that is widely studied [46, 47] and known as a hybrid meson.

This state has not been previously studied using a lattice regularisation though other non-perturbative estimates of the $\tilde{g}q\bar{q}$ state have been made. We proceed to make such a determination using the Wilson-clover action. We contrast our measurements of the state ordering of the adjoint meson with that of Chanowitz *et al.* who have made their calculation using the MIT bag model [38].

Similar approximations and assumptions are made with regard to the static approximation and quenching as were discussed in Section 8.1. In this calculation there also arise new systematic errors from unrealistically heavy 'light' quarks used for the $q\bar{q}$ components as well as the possibility of significant O(a) effects from the fermionic components. We attempt to explore the former, using a chiral extrapolation from mass determinations at heavier masses, and the second by examination of the β dependence of the spectrum.

9.2 The Adjoint Meson

In the following study, the J^{PC} states of the system are labelled according to the symmetry properties of the light quark bilinear. We note that this does not correspond to the continuum R-meson. Notably the charge conjugation will differ between the two as a consequence of the intrinsic charge conjugation of the gluino which is not present in our calculation. Also the state will be fermionic rather than the scalar and vector-like states we generate. Following Chanowitz *et al.* our states might be labelled R_π, R_ρ which corresponds to our labelling, P_A, V_A etc.

In one of the first analyses of this state [38], Chanowitz and Sharpe presented a bag model calculation of the R-meson mass spectra, over a range of M_{gluino}. In contrast to the conventional standard model mesonic spectrum, they find that the J^{PC} ordering of the vector and pseudoscalar states, places the vector like particle as being the lighter of the two over the range of M_{gluino} that they investigated. Interestingly, their determination of the spectrum places the gluelump (glueballino) as slightly heavier than the adjoint meson for larger M_{gluino}. We shall explore this mass splitting in our calculation.

The ordering of the conventional meson spectrum can be understood qualitatively from the colour-spin interactions arising from one gluon exchange [48]. This interaction goes some way towards describing the features of the mesonic spectrum and has been shown to give reasonable agreement with the $\rho - \pi$ splitting [49].

The binding energy includes a term arising from spin interactions of the form $k\frac{\alpha_s \pi}{2}\frac{16 S_i S_j}{3 m_i m_j}$. Here the quarks are labelled i, j with masses m and spin S. The factor k represents a group theory term associated with the SU(3) one gluon exchange diagram. This will differ between the meson and adjoint meson states as it depends upon the overall colour representation of the two quarks. The adjoint meson quarks are bound in an octet rather than a singlet.

We can explore the difference between the spectra by evaluating this colour component. The exchange diagrams are shown in Figure 9.1 both for the mesonic case and the adjoint meson. We can see this model predicts the splitting;

$$\Delta E_{\text{adj.meson}} = -\frac{1}{8}\Delta E_{\text{meson}} \tag{9.1}$$

This colour-spin interaction then predicts that the V_A state will be slightly lighter than the P_A state in the continuum limit. We shall investigate this hypothesis in our calculation.

It is worth noting that the simple model of the mass splitting from one gluon exchange between

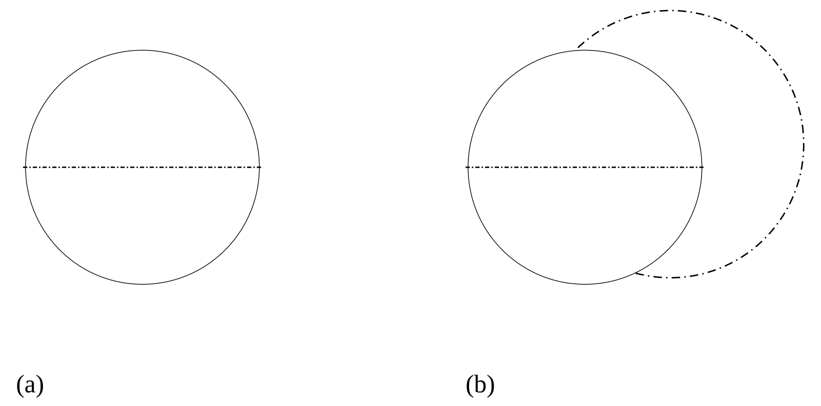

Figure 9.1: Feynman diagrams representing one gluon exchange between two quarks bound in a singlet (a) and the adjoint (b). Adjoint vector lines are represented as a dashed line. The diagrams should be averaged over initial states giving a factor of $\frac{1}{8}$ for the adjoint which has 8 colour possibilities and $\frac{1}{3}$ for the fundamental for the 3 possible colour states of the normal meson. This gives colour factors for the two diagrams of $\frac{8}{3}$ and $-\frac{1}{3}$ respectively.

the fundamental quarks is not isolatable in the data of Chanowitz *et al.* In this calculation they use a finite gluino mass, which we expect to include gluino-quark spin-spin interactions. These effects become more significant with lighter gluinos and complicate the simple one gluon exchange picture.

9.3 Adjoint Meson Correlators

Correlators employing the static fermion approximation and light quark propagators use only one element of a conventional point sourced propagator. Hence we use an alternative approach. The method of maximally variance reduced stochastic propagators described in Section 6.3 allows the construction of correlators with the static source at any spatial position on the lattice though not between arbitrary timeslices as in the case of the gluelump. This implementation includes an SW-clover improvement term which reduces and potentially removes $O(a)$ corrections.

It is not consistent to use multi-hit improvement for the time-links of the static source as we have used previously for the gluelump. This is because the inverse of the fermion matrix (the light quark propagator) is determined in the context of the original lattice.

We construct creation operators for the adjoint quark bilinear according to,

$$\mathcal{M}^{\alpha}_{\mathrm{Adj}} = \bar{\psi}(x)\lambda^{\alpha}\Gamma\psi(x) \tag{9.2}$$

such that the correlation function is given by combining this with the static adjoint source, G^A, and replacing quark propagator terms, $\bar{\psi}_i\psi_j$ with $\langle\phi_j(M_{ik}\phi_k)^*\rangle$ which we described in Section 6.3. The correlation function is given in Equation 9.3.

$$\begin{aligned} C(\Gamma, t_2 - t_1) &= \sum_x \left(\bar{\psi}(x,t_1)\lambda^{\alpha}\Gamma\psi(x,t_1)\right)^{\dagger} \left(\bar{\psi}(x,t_2)\lambda^{\beta}\Gamma\psi(x,t_2)\right) G^A_{\alpha\beta}(t_1,t_2) \\ &= \sum_x \sum_{i\neq j} \mathrm{Tr}\left(\phi_j(x,t_1)\lambda^{\alpha}\Gamma(M\phi_i(x,t_1))^*\phi_i(x,t_2)\lambda^{\beta}\Gamma(M\phi_j(x,t_2))^*\right) G^A_{\alpha\beta}(t_1,t_2) \end{aligned} \tag{9.3}$$

Here i and j are different samples of the pseudofermion fields and $i = j$ is undefined. The trace is over fundamental colour and spin indices. We symmetrise the placement of t_1 and t_2 about the boundaries of the improvement region. Where $t_2 - t_1$ is odd we average over the two possible placements. Using this prescription, time correlations of $t_2 - t_1 \leq 2$ are unobtainable as they contain systematic errors. This is a result of $M\phi$ containing elements from adjacent time-slices.

9.4 Computational Details

We examine a range of gamma matrices for any mass dependence on the nature of the current. We focus on observables with $\Gamma = \gamma_5,\ \gamma_i$ and I, corresponding to P_A, V_A and S_A (scalar) mesons, respectively. We present measurements for these Γ combinations, averaging over the components of γ_i for the V_A case. Other J^{PC} combinations were more poorly determined on the dataset with masses compatible with the scalar case, S_A, or higher.

We are limited in our range of lattices for this calculation as the technology for the stochastic inversion process is available only on vector type machines at the current time, which is limiting, both in speed, memory and cost. Consequently we must acknowledge the possibility of systematic error through an inadequate ensemble size. We appeal to the determination of other quantities (such as the pion mass) on the same data set which give reasonable agreement with higher statistics determinations.

We confine ourselves to a range of coarser lattices detailed in Table 9.1. At $\beta = 5.7$ we use two values of the hopping parameter, the lighter of which corresponds approximately to the

Table 9.1: Lattices used in adjoint meson calculation

β	Size	Propagator Samples	κ	C_{SW}	Gauge Configurations
5.7	$8^3 \times 16$	24	0.13843	1.57	20
5.7	$12^3 \times 24$	24	0.13843	1.57	20
5.7	$8^3 \times 16$	24	0.14077	1.57	20
5.7	$12^3 \times 24$	24	0.14077	1.57	20
5.9	$12^3 \times 24$	24	0.13750	1.50	20
6.0	$16^3 \times 24$	24	0.13714	1.76	10

strange quark mass. This enables us to make a rough examination of the dependence on κ of the spectrum, and an extrapolation to the chiral limit. A small sample of lattices at a finer spacing was generated following the relatively large disagreement between results for $\beta = 5.9$ and $\beta = 5.7$ and the relatively poor determination of the state at $\beta = 5.9$. With this third data point we are also able to explore the lattice spacing dependence with more certainty.

We focus in this calculation on the most symmetric operator the A_1^{++}, using a combination of local and extended operators to create a 2×2 correlation matrix. We construct extended (fuzzed) operators by replacing the ϕ and $M\phi$ fields in Equation 9.3, using the symmetric fuzzing prescription,

$$\psi_l(x)^{\text{fuzzed}} = \psi(x) + \Sigma_{\pm(\mu=1,3)} U_\mu^{(l)}(x)\psi(x + la_\mu) \tag{9.4}$$

where $U_{-\mu}(x) = U_\mu^\dagger(x - \hat{\mu})$ in this context. Here $U^{(l)}$ is a product of fuzzed links of length la, each link defined according to Equation 5.10. We use links of varying lengths and fuzzing parameters as described in Table 9.2.

Table 9.2: Extended operator parameters for the adjoint meson

β	Fuzzing Length	C	Fuzzing Iterations
5.7	1	4.0	12
5.9	1	4.0	20
6.0	2	2.5	6

9.5 The Adjoint Meson Spectrum

As in the gluelump case, we performed a variational analysis on the data and were able to obtain, in most cases, an estimate of the ground state mass. For this we use an operator basis determined between $t = 2$ and 3. For the larger lattices, $12^3 \times 24$ and bigger, a 2 exponential fit was performed. That is, the correlation data was fit to the function,

$$C_{ij}(t) = \sum_{i,j} \sum_{k=1,2} c_i^{(k)} e^{-m_k t} c_j^{(k)} \tag{9.5}$$

for correlations between source and sink operators, i and j. Errors on the estimates of the six parameters in the fit were made by bootstrap resampling methods using 99 resamples of the configurations. We find the V_A mass is more accurately determined largely because it is taken as the average of three independent components. The obtained masses are presented in Table 9.3. The variational analysis masses are given at the point at which plateau is seen, except where comments indicate otherwise.

We find that the P_A and V_A states are lightest with the scalar state having a weaker signal and lying significantly higher on the lattice spacings considered. We concentrate in our discussions on these lighter states.

There are several systematic errors that contribute to the measurements of the states. Namely they are finite lattice volume and lattice spacing, unphysically large quark mass and errors from

Table 9.3: Ground state adjoint meson masses

Γ	β	Size	κ	Lattice masses: Var. analysis	Fit	t-range	χ^2/DoF
γ_5 (P_A)							
	5.7	$8^3 \times 16$	0.13843	1.892(57)			
	5.7	$12^3 \times 24$	0.13843	1.913(40)	1.870(164)	$6 \to 8$	1.29
	5.7	$8^3 \times 16$	0.14077	1.889(40)			
	5.7	$12^3 \times 24$	0.14077	1.905(23)	1.894(30)	$3 \to 8$	1.43
	5.9	$12^3 \times 24$	0.13750	1.668(103)*	1.650(87)	$5 \to 8$	0.03
	6.0	$16^3 \times 24$	0.13417	1.695(44)	1.468(153)	$5 \to 10$	0.86
γ_i (V_A)							
	5.7	$8^3 \times 16$	0.13843	1.877(19)			
	5.7	$12^3 \times 24$	0.13843	1.921(54)	1.965(36)	$5 \to 8$	0.71
	5.7	$8^3 \times 16$	0.14077	1.875(24)			
	5.7	$12^3 \times 24$	0.14077	1.851(55)	1.867(56)	$4 \to 8$	0.32
	5.9	$12^3 \times 24$	0.13750	1.779(46)	1.780(28)	$4 \to 8$	1.04
	6.0	$16^3 \times 24$	0.13417	1.578(114)	1.440(70)	$5 \to 10$	1.03
I (S_A)							
	5.7	$8^3 \times 16$	0.13843	2.262(73)			
	5.7	$12^3 \times 24$	0.13843	2.273(38)			
	5.7	$8^3 \times 16$	0.14077	2.337(173)			
	5.7	$12^3 \times 24$	0.14077	2.280(51)			
	5.9	$12^3 \times 24$	01.13750	1.953(134)	1.941(145)	$4 \to 8$	1.09

* No plateau observed.

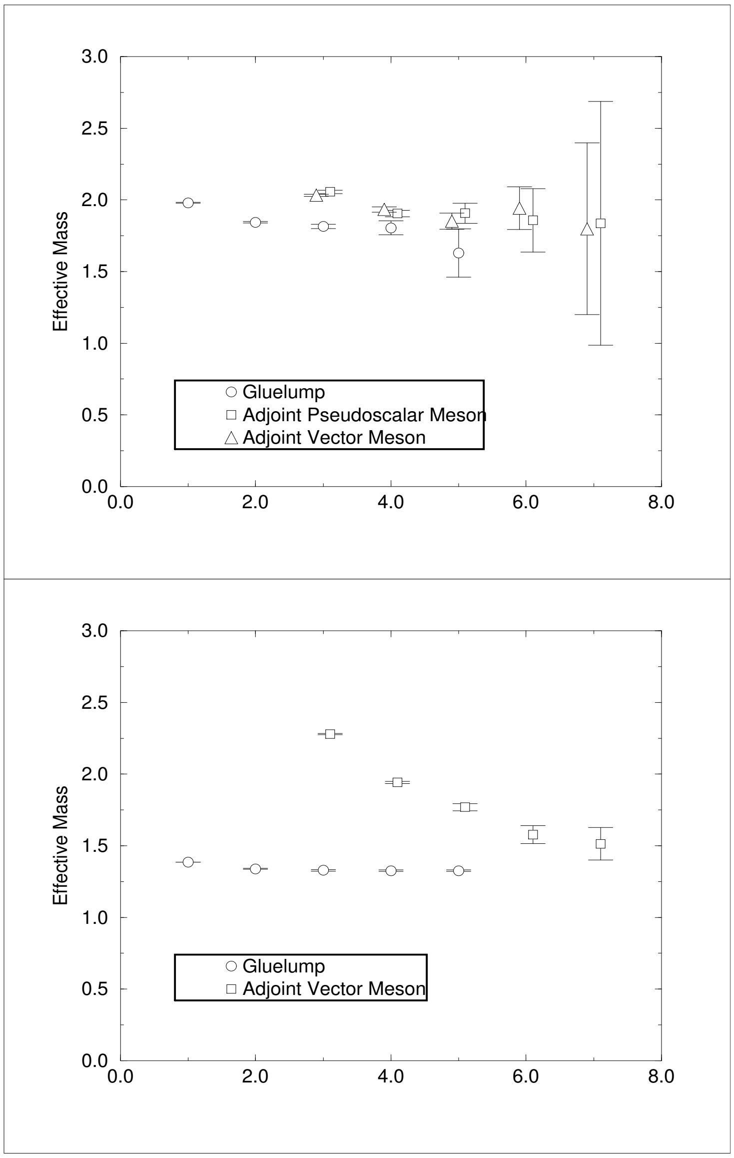

Figure 9.2: Effective lattice mass vs. lattice time for P_A, V_A, and T_1^{+-} gluelump states for $\beta = 5.7$ (top) and $\beta = 6.0$ (bottom).

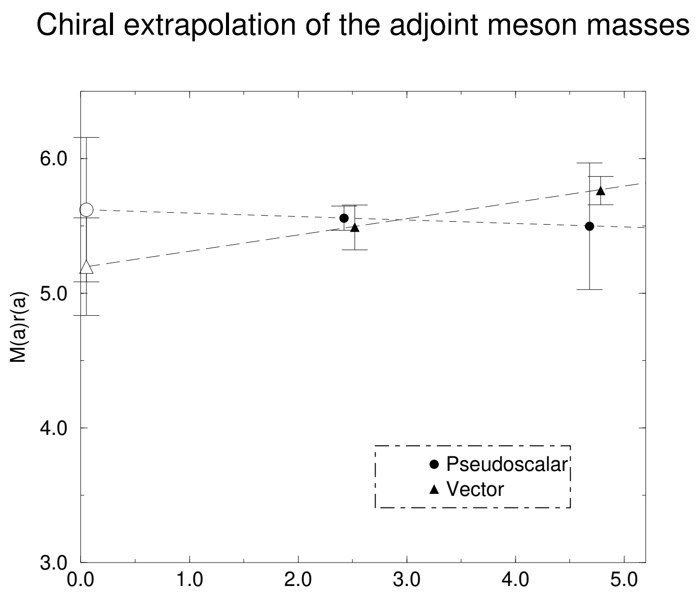

Figure 9.3: Dependence of the P_A and V_A on κ at $\beta = 5.7$. The ordinate is $r_o^2 m_\pi^2$

Table 9.4: Pion Masses at $\beta = 5.7$ ($C_{SW} = 1.57$) and $\beta = 6.0$ ($C_{SW} = 1.77$) from [50] and [51] respectively.

β	κ	Mass
5.7	0.13843	0.736(2)
5.7	0.14077	0.529(2)
6.0	0.13417	0.309(2)

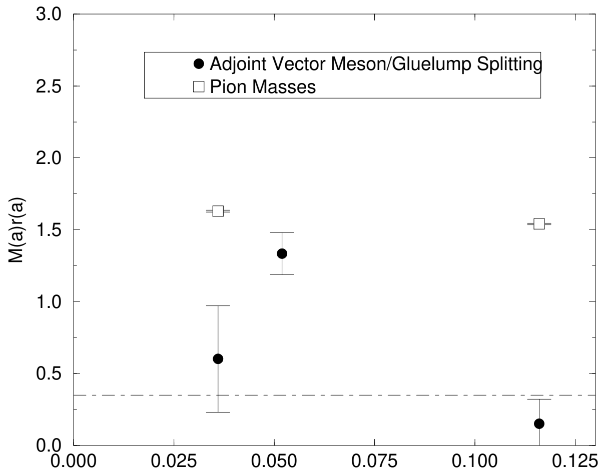

Figure 9.4: Lattice Spacing Dependence of the adjoint meson/gluelump splitting. The abscissa is $r_o^{-2}(a) \sim a^2$. The horizontal line is the experimental pion mass (0.35 in units of Mr_0). Pion masses from lattice determinations are also plotted using the same quark mass and improvement coefficient as the adjoint meson measurement at the same lattice spacing.

the determination of the masses. We will discuss these in reverse order.

The raw effective masses are plotted in Figure 9.2. These masses are generated from the combination of paths used in the variational analysis and are plotted as a function of lattice time. We see that in both cases presented a plateau is attained indicating that excited state mass contributions are controlled. For the pseudoscalar case at $\beta = 5.9$ and $\beta = 6.0$ the signal is considerably more noisy. It is not clear that these determinations are free of such contamination, though there are fewer measurements of the operator which may explain the larger errors. In these cases we may consider the presented measurements as upper bounds. There is more excited state contamination in the $\beta = 6.0$ measurements. This is related to the physical time extent of the operator which is considerably shorter for a given lattice time in the $\beta = 6.0$ case (a factor of approximately 1.8). Effective masses for $t < 3$ were not accessible using this method.

The κ used in the calculation corresponded to rather heavy quarks (strange quark or heavier). The adjoint meson, which we model, is composed of u and d quarks. At $\beta = 5.7$ we used two values of the quark mass. This enables us to make an extrapolation toward physically more interesting light quarks. We sketch the layout of these states in Figure 9.3. We plot the fitted data as $m(\kappa, a)r_0(a)$ against $(m_\pi(\kappa, a)r_0(a))^2$. From chiral symmetry arguments we expect the abscissa, $(m_\pi^2 r_0)$, to be linear in the constituent quark mass, whilst other masses of hadronic states should behave as $M_H \sim m_q$. Thus the figure enables us to make a linear extrapolation in the light quark mass with the chiral limit being the point at which $(m_\pi(\kappa, a)r_0(a))^2 = 0$. Values for the pion mass at $\beta = 5.7$ were taken from [50] and are given in Table 9.4. We see little dependence on κ at this lattice spacing which is consistent with lattice determinations of the Λ baryon [27] which is treated as a heavy-light-light quark system antisymmetric in the colour fields. We have not calculated the adjoint meson mass at more than one κ for any other lattice spacing, so we are unable to determine if this behaviour is different at finer lattice spacings.

We move on to consider finite spacing effects. We examine differences between the gluelump and adjoint meson masses at identical β. Thus the self energy of the adjoint source should be removed and we can consider the effects of the lattice spacing on this splitting. In the previous chapter we were able to make a linear extrapolation for the splittings between gluelump excited states. Here we cannot as the measurements contain O(a) lattice artifacts which differ between the measurements. The $\beta = 6.0$ measurement uses a non-perturbative improvement coefficient, $C_{\rm SW}$, which should remove O(a) effects completely. It is also the finest lattice used and as such we might expect this to provide the best estimate of the splitting. Unfortunately it is also the smallest ensemble which we have considered. We plot the states a^2 dependence in Figure 9.4 on the same scale as we used in the previous chapter to facilitate comparisons, though as stated we do not *a priori* expect any linearity.

Finally we consider finite lattice size effects. At $\beta = 5.7$ we have two lattice volumes available for direct comparisons. We see no significant discrepancies between the adjoint meson masses on these lattices. $\beta = 6.0$ with a volume of $(16a)^3$ has been used in previous determinations of the hadronic spectrum [51]. No finite size effects were seen here and we infer from this that the volume is sufficiently large. In previous unpublished work, by C. Michael and J. Peisa, finite size effects were seen in determinations of the b meson mass at $\beta = 5.9$ on a $12^3 \times 24$ lattice. We may expect that the adjoint meson is at least comparable in size to the b meson and this may explain the rather high estimate of its mass on these lattices. We should perhaps disregard this measurement, but with the small range of available lattices with stochastic propagators for comparison, we include it with this caveat.

9.6 Discussion

It is of some phenomenological interest to determine the relative ordering of the $\tilde{g}g$ and $\tilde{g}q\bar{q}$ states. Of particular interest is how the magnitude of any splitting compares with the rest mass of the pion. This may dictate the lightest observable supersymmetric state in some models, and almost certainly the lightest super-hadron. The comparison with the pion mass is of relevance to the examination of strong decay channels available to the states.

The data obtained is insufficient to make an accurate estimation of the ordering between the states in the light quark limit. For strange quark masses, we examine the effective masses given in Figure 9.2 and compare them with those obtained for the gluelump which are also plotted. It can be seen that for the $\beta = 5.7$ case the gluelump appears fractionally lighter over the range of t for which comparison is possible. This is consistent with the fitted determination shown in Figure 9.4, though, as can be seen, the result is not statistically significant. At $\beta = 6.0$, the splitting appears slightly larger, though a region of plateau is less clear. The corresponding determination from the fit indicates that the adjoint meson is the more massive, with some statistical significance. The expectation is that the splitting in this case is 236(146)MeV which is comparable with the experimental pion mass of 140MeV.

We see no statistically significant ordering of the pseudoscalar and vector states. Application of the one gluon exchange model described predicts the vector to be the lighter. The substitution of experimental values for the π and ρ masses indicates that this splitting should be 0.2 in units of Mr_0 or 0.1 from quenched lattice determinations of the state at $\beta = 6.0$. This expected splitting is comparable or smaller than the errors on our determinations of the masses which is consistent with the ambiguous ordering

We have investigated a new lattice state, which, though having an unphysical continuum limit mass, does give rise to quantities that do survive to the continuum limit. We have formulated the state as a heavy mass limit approximation to a supersymmetric state that is believed to be one of the lighter super-hadrons and contrasted our results with another non perturbative determination of its spectrum. Our calculations suggests that the mass ordering with respect to the determination of the gluelump state in the previous chapter differs from this calculation. We note that our measurement is one of considerably low statistics and employs different assumptions and errors to the bag model formulation used in this previous determination.

Chapter 10

Mass Dependence of the b Meson on κ_v

10.1 Introduction

The introduction of the variance reduced pseudofermionic propagators opens up the possibility of studying other observables where propagators from many points are necessary, or at least provide an improved measurement through a greater self averaging.

One such area of study is that of three point correlation functions. These correspond to evaluating matrix elements in lattice QCD. The pseudofermion method has been used in such studies with regard to b meson decay processes [52].

We proceed to investigate a method of determining mesonic mass dependences on the constituent quark masses, using an explicit formal differentiation of the discretised path integral, and Monte-Carlo evaluation of the resulting three point correlation functions. The procedure is analogous to the methods previously used to study flux distributions [53, 54], and this general approach is known as a 'sum' rule. We are able to contrast the resulting matrix element with finite difference estimates of the same quantity, the meson mass, measured at different κ_v.

We explain the method for the case of the b meson, where the results from mass spectroscopy with pseudofermionic propagators showed most improvement over conventional methods. The process has also been carried out independently for light-light vector and pseudoscalar mesons using the same procedure.

10.2 Differentiating the Functional Integral

The b meson is a bound state of two quarks, one bottom and one light quark, up or down (e.g. $b\bar{u}$ or $u\bar{b}$). In lattice calculations, such systems of heavy-light mesons are often studied using the static approximation to represent the heavier quark, and a light quark propagator for the u quark. The pseudofermion propagators that we use in this calculation allow the construction of three point functions. There is also in existence an existing comparative and detailed measurement of the b meson spectrum.

The correlator used to measure the b meson is given by

$$\begin{aligned} C(t = t_2 - t_1) &= \langle B(t_1)^\dagger B(t_2) \rangle \\ &= \langle (Q(t_1)\Gamma\bar{\psi}(t_1))^\dagger ((Q(t_2)\Gamma\bar{\psi}(t_2))) \rangle \\ &= \langle G(t_2, t_1)\Gamma(1+\gamma_4) \prod_{t_4=t_1}^{t_2-1} U_4(x, t_4)\Gamma \rangle \end{aligned} \tag{10.1}$$

where we represent the light quark propagator as G, which connects the two ends of the static source. There is also a summation over spatial points implied, together with a trace over spin and colour indices. Q(ψ) represent the heavy(light) quark fields. We replace $\bar{Q}(t_1)Q(t_2)$ in the second line with the static approximation chosen to define the heavy quark as propagating forward in time ($b\bar{u}$). Recalling the definitions of the correlation function we can write this as,

$$\begin{aligned} C(t) &= \int \mathcal{D}U B(t_1)^\dagger B(t_2) e^{-S} \\ &= \int \mathcal{D}U \mathrm{Tr} \left(G\Gamma(1+\gamma_4) \prod_{t_4=t_1}^{t_2-1} U_4(x, t_4)\Gamma \right) e^{-S} \end{aligned} \tag{10.2}$$

or using the mass expansion of the correlator,

$$C(t) = c_0^2 e^{-m_0 t} + c_1^2 e^{-m_1 t} + \ldots \tag{10.3}$$

We wish to differentiate this equation with respect to κ^{-1}, which is related to the quark mass in Equation 3.9, in order to extract the overall ground state mass dependence on κ^{-1}, $\frac{dm_0}{d\kappa^{-1}}$. In order to simplify this procedure we rescale the ψ fields in the usual action. The quark matrix 3.10 can be written schematically as,

$$M = 1 + \kappa D \tag{10.4}$$

where D includes all finite difference terms, gauge fields and the clover improvement expression but no explicit dependence on κ. Through the rescaling $\tilde{\psi} = \sqrt{\kappa}\psi$ we can write

$$\tilde{M} = \kappa^{-1} + D \tag{10.5}$$

We recall that the propagator, G, is the Green function of M, and hence we examine the properties of the Green function of the new matrix $\tilde{M}$. We have,

$$MG = \tilde{M}\tilde{G} = 1 \tag{10.6}$$

$\tilde{M}$ has very simple dependence on κ and thus we are able to proceed to differentiate this equation, obtaining a relationship between the light quark propagator and κ^{-1},

$$\begin{aligned} \frac{d}{d\kappa^{-1}}(\tilde{M}\tilde{G}) &= \frac{d\tilde{M}}{d\kappa^{-1}}\tilde{G} + \tilde{M}\frac{d\tilde{G}}{d\kappa^{-1}} \\ &= \tilde{G} + \tilde{M}\frac{d\tilde{G}}{d\kappa^{-1}} = 0 \end{aligned} \tag{10.7}$$

and upon eliminating $\tilde{M}$ using Equation 10.6

$$\frac{d\tilde{G}}{d\kappa^{-1}} = -\tilde{G}.\tilde{G} \tag{10.8}$$

Returning to the original topic, Equation 10.2 is now easy to differentiate. In quenched QCD there is no dependence upon κ in the action. We can thus work within the framework where the quark degrees of freedom have been integrated out. In dynamical QCD we must consider terms arising from the κ dependence upon the action and we will discuss this in Chapter 12. Proceeding, we have,

$$\begin{aligned} \frac{dC(t)}{d\kappa^{-1}} &= \int \mathcal{D}U \mathrm{Tr}\left(\frac{dG}{d\kappa^{-1}}\Gamma(1+\gamma_4)\prod_{t_4=t_1}^{t_2-1} U_4(x,t_4)\Gamma\right) e^{-S} \\ &= -\int \mathcal{D}U \sum_t \mathrm{Tr}\left(G.GF(\Gamma)\prod_{t_4=t_1}^{t_2-1} U_4(x,t_4)\right) e^{-S} \end{aligned} \tag{10.9}$$

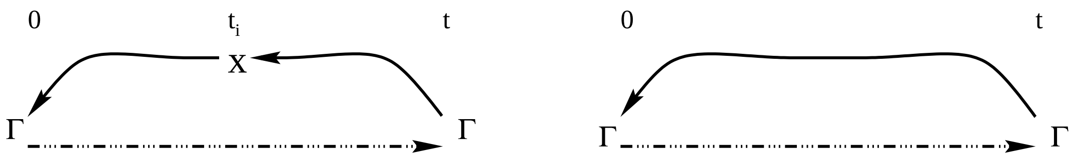

(a) Connected 3-point Mesonic Correlator (C3) (b) Connected 2-point Mesonic Correlator (C)

Figure 10.1: Connected Diagrams involved in the differentiation of the b meson correlation function.

where we have replaced the $\Gamma(1+\gamma_4)\Gamma$ with $F(\Gamma)$ for conciseness. Similarly Equation 10.3 gives,

$$\frac{dC(t)}{d\kappa^{-1}} = c_0^2 \frac{dm_0}{d\kappa^{-1}} t e^{-m_0 t} + c_0^2 \frac{dc_0^2}{d\kappa^{-1}} e^{-m_0 t} + \ldots \tag{10.10}$$

In the above derivation $G.G$ is a usual matrix product. Thus the summation implied is over all lattice sites. We denote the 3 point correlation function $C_3(t, t_i)$ as the subset of the correlation function appearing in Equation 10.9 with the $G.G$ summation performed over all spatial sites but localised to one time-plane t_i. C_3 and C are depicted in Figure 10.1

$$C_3(t, t_i) = \langle \sum_x -G(t, t_i).G(t_i, 0)\Gamma(1+\gamma_4) \prod_{t_4=t_1}^{t_2-1} U_4(x, t_4)\Gamma \rangle \tag{10.11}$$

We consider the set of intermediate states arising from the function, C_3. Factors of $e^{-m(t_2-t_i)}$, $e^{-m(t_i-t_1)}$ arise from the intermediate propagating states together with the usual overlap coefficients at source and sink, c. Between the two states at the insertion the unknown process is represented as matrix, X, corresponding to transitions between mass eigenstates in the two propagating sections. In the large t limit, C_3 will be dominated by the ground state such that,

$$\sum_{t_i} C_3(t, t_i) = c_0^2 t X_{00} e^{-m_0 t} + \ldots \tag{10.12}$$

where X_{00} is the matrix element between ground states. We equate the coefficients in $te^{-m_0 t}$ in Equations 10.12 and 10.10 to give,

$$\frac{dm_0}{d\kappa^{-1}} = X_{00} = \lim_{t,t_i \to \infty} \frac{C_3(t,t_i)}{C(t)} \tag{10.13}$$

We see that we have removed the summation over the insertion point in the L.H.S of Equation 10.12. We may in general average over choices of the insertion plane, however, in order to minimise contamination from excited states we make the selection that $t_2 - t_i = t_i - t_1 \sim t/2$.

10.3 Operators

We construct both C_3 and C correlation functions using the pseudofermionic fields previously described. In order to follow the rules for the improved pseudofermion correlations prescribed in Chapter 6, we must place the insertion on the improvement region boundary as it is from here only that correlations can be made with fields in both domains of improvement. Furthermore the fields multiplied by the fermion matrix, M, contain nearest neighbour terms. We are thus constrained to place the $M\phi$ operators at the extremes of the correlator, at t_1 and t_2, rather than at the insertion. Thus, the two point function is given by;

$$\begin{aligned} C(t) &= \langle \sum_x \mathrm{Tr}\bar{\psi}(x,t_2)\psi(x,t_1)F(\Gamma)\prod_{t_4=t_1}^{t_2-1} U_4(x,t_4)\rangle \\ &= \langle \sum_x \sum_i \mathrm{Tr}\phi_i(x,t_1)(M\phi_i(x,t_2))^* \left(F(\Gamma)\prod_{t_4=t_1}^{t_2-1} U_4(x,t_4)\right)\rangle \end{aligned} \tag{10.14}$$

where i represents a sum over pseudofermionic samples. For the 3 point function,

$$\begin{aligned} C_3(t,t_i \sim t/2) &= \langle \sum_x \sum_{x_i} \mathrm{Tr}\bar{\psi}(x,t_2)\psi(x_i,t_i)\bar{\psi}(x_i,t_i)\psi(x,t_1)\left(F(\Gamma)\prod_{t_4=t_1}^{t_2-1} U_4(x,t_4)\right)\rangle \\ &= \langle \sum_{i\neq j}\sum_x \sum_{x_i} \mathrm{Tr}\phi_i(x_i,t_i)(M\phi_i(x,t_2))^*(x,t_2)\gamma_5(M\phi_j(x,t_1))\phi_j^*(x_i,t_i)\gamma_5 \\ &\qquad \left(F(\Gamma)\prod_{t_4=t_1}^{t_2-1} U_4(x,t_4)\right)\rangle \end{aligned} \tag{10.15}$$

where j and k are indices on the fermionic samples as before, and we have used the relationship Equation 5.17 to write down the propagator estimate so that the $M\phi$ fields are not sited on the improvement boundary, t_i. Where t is odd, the average of the two asymmetric placements of the correlator is made. This implies that excited state contamination will arise primarily from the shorter of the two legs.

Table 10.1: Lattices used for computation of C and C_3

β	Size	Prop. Samples	κ	C_{SW}	Number
5.7	$8^3 \times 16$	24	0.13843	1.57	20
5.7	$12^3 \times 24$	24	0.13843	1.57	20
5.7	$8^3 \times 16$	24	0.14077	1.57	20
5.7	$12^3 \times 24$	24	0.14077	1.57	20

As for the adjoint meson, we construct fuzzed and local operators at both source and sink using the same fuzzing prescription given in Equation 9.4. The ϕ fields at the insertion remain local.

10.4 Computational Details

We construct the two and three point correlators for $t = 2$ to $L_4/2$. We use the same ensemble of lattices (Table 10.1) for which we have pseudofermion samples available at $\beta = 5.7$. In choosing this data set we have two hopping parameters at which we are able to contrast the measurement with the finite difference prediction. Fuzzing parameters are detailed in Table 10.2

10.5 Extracting the Matrix Element

We examine two approaches to extract the desired Matrix element, X_{00}, from the calculated correlation functions. The first, and more direct, approach is to perform a simultaneous fit to both two and three point functions. For a two exponential model this provides a total of ten free parameters for the fitting function. We constrain this to nine by demanding symmetry in the matrix $X_{01} = X_{10}$ though this seen to have little effect on the fit. We might also expect the excited state to have a similar dependence on the quark mass. Thus, it is conjectured that

Table 10.2: Extended Operator Parameters for the b meson 2 and 3 point functions

β	Fuzzing Length	C	Fuzzing Iterations
$5.7(8^3)$	2	4.0	10
$5.7(12^3)$	2	4.0	12

setting $X_{00} = X_{11}$ is also a valid constraint to the fit. This was considered for the lighter of the two hopping parameters in order to improve the result though again had little effect on the estimate of the matrix element. The presented results do not include this latter constraint. The general functional form of the fitting function is taken to be;

$$C_{ij}(t) = \sum_{k=0,1} c_i^{(k)} e^{-m_k t} c_j^{(k)} \tag{10.16}$$

and either

$$C_{3,ij}(t, t/2) = \sum_{k,l=0,1} c_i^{(k)} e^{-\frac{m_k t}{2}} X_{lk} e^{-\frac{m_l t}{2}} c_j^{(l)} \tag{10.17}$$

for even t and

$$C_{3,ij}(t, \sim t/2) = \frac{1}{2} \sum_{k,l=0,1} c_i^{(k)} \left(e^{-\frac{m_k (t-1)/2}{2}} X_{lk} e^{-\frac{m_l ((t-1)/2+1)}{2}} + e^{-\frac{m_k ((t-1)/2)+1}{2}} X_{lk} e^{-\frac{m_l (t-1)/2}{2}} \right) c_j^{(l)} \tag{10.18}$$

for odd t. In this fit the masses, coefficients, and matrix elements are fixed between the two expressions and are all free in the least squares minimisation process. This takes place with regard to all data and functions without bias. Evaluated parameters are quoted with errors from 99 bootstrap fits and given in Table 10.3. The term X_{00} is the required ground state matrix

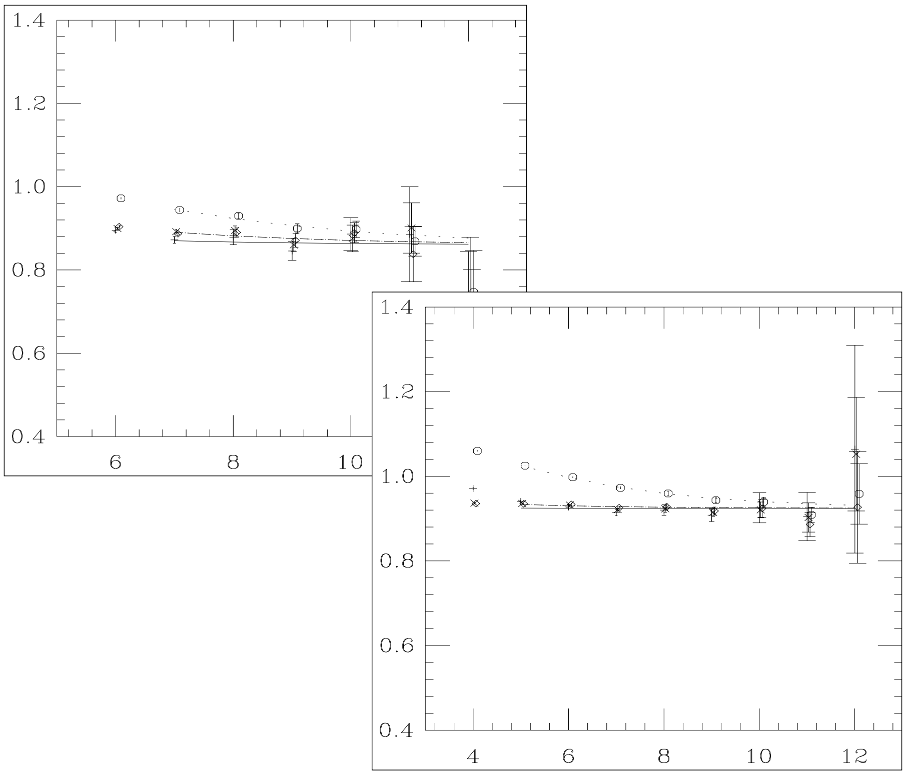

Figure 10.2: b meson two exponential mass fit for $\kappa = 0.14077$ (top right), and $\kappa = 0.13843$

element. The data was fit from different minimum time values, $T_{\min}$, and $T^3_{\min}$ for the two and three point data respectively. Two and one exponential fits were made to ensure consistency and stability of the fit. The two point data is compared with the parameters obtained from the simultaneous fit in Figure 10.2.

A second approach is to examine the ratio of 3-point to 2-point functions directly. This ratio, as given in Equation 10.13, provides the matrix element of interest though it is subject to excited state contamination. We attempt to control this contamination in the ratio by suitable choice of operator path combinations. For ground state mass computation, as discussed in Chapter 7, we have previously sought to generate maximal overlap of the operator paths with the ground state. Here we choose an alternative, we construct the combination which corresponds to a basis orthogonal to the excited state to minimise this source of error. We use the overlap coefficients

Table 10.3: Fitted parameters to the two/three point simultaneous fit. Suffix 0 corresponds to the ground state, while l and f to local and fuzzed overlap coefficients.

Lattice Size	κ	X_{00}	$c_l^{(1)}$	$c_f^{(1)}$	T_{min}	T^3_{min}	T_{max}	χ^2/ DoF
$8^3 \times 16$	0.13843	0.36(5)	0.60(7)	0.33(3)	6	6	8	0.36
$12^3 \times 24$	0.13843	0.21(8)	0.06(2)	0.31(1)	4	8	12	0.76
$8^3 \times 16$	0.14077	0.15(4)	0.18(30)	0.26(4)	6	6	8	0.12
$12^3 \times 24$	0.14077	0.11(5)	0.14(4)	0.32(6)	4	8	12	0.43

Table 10.4: The ratio $\frac{C_3(t)}{C(t)}$

κ	$t = 2, 3, 4 \ldots$						
0.13843	0.166(11)	0.190(9)	0.210(9)	0.241(11)	0.279(18)	0.289(29)	0.300(66)
0.14077	0.104(21)	0.120(23)	0.144(22)	0.159(28)	0.129(47)	0.140(48)	0.134(93)

generated by the fitting procedure $c_l^{(1)}$, $c_f^{(1)}$ (given in Table 10.3) to construct such a vector,

$$e_\perp^{(1)} = \begin{pmatrix} c_f^{(1)} \\ -c_l^{(1)} \end{pmatrix} \tag{10.19}$$

We apply this basis to produce a 1^{st} excited state free correlation vector,

$$R(t) = \frac{e_\perp^{(1)} C_3(t, \sim t/2) e_\perp^{(1)}}{e_\perp^{(1)} C(t) e_\perp^{(1)}} \tag{10.20}$$

We show this ratio as a function of lattice time, both numerically and graphically, in Table 10.4 and Figure 10.3.

Figure 10.3: The ratio, R, plotted versus time. $\kappa = 0.13843$ is above, $\kappa = 0.14077$ below.

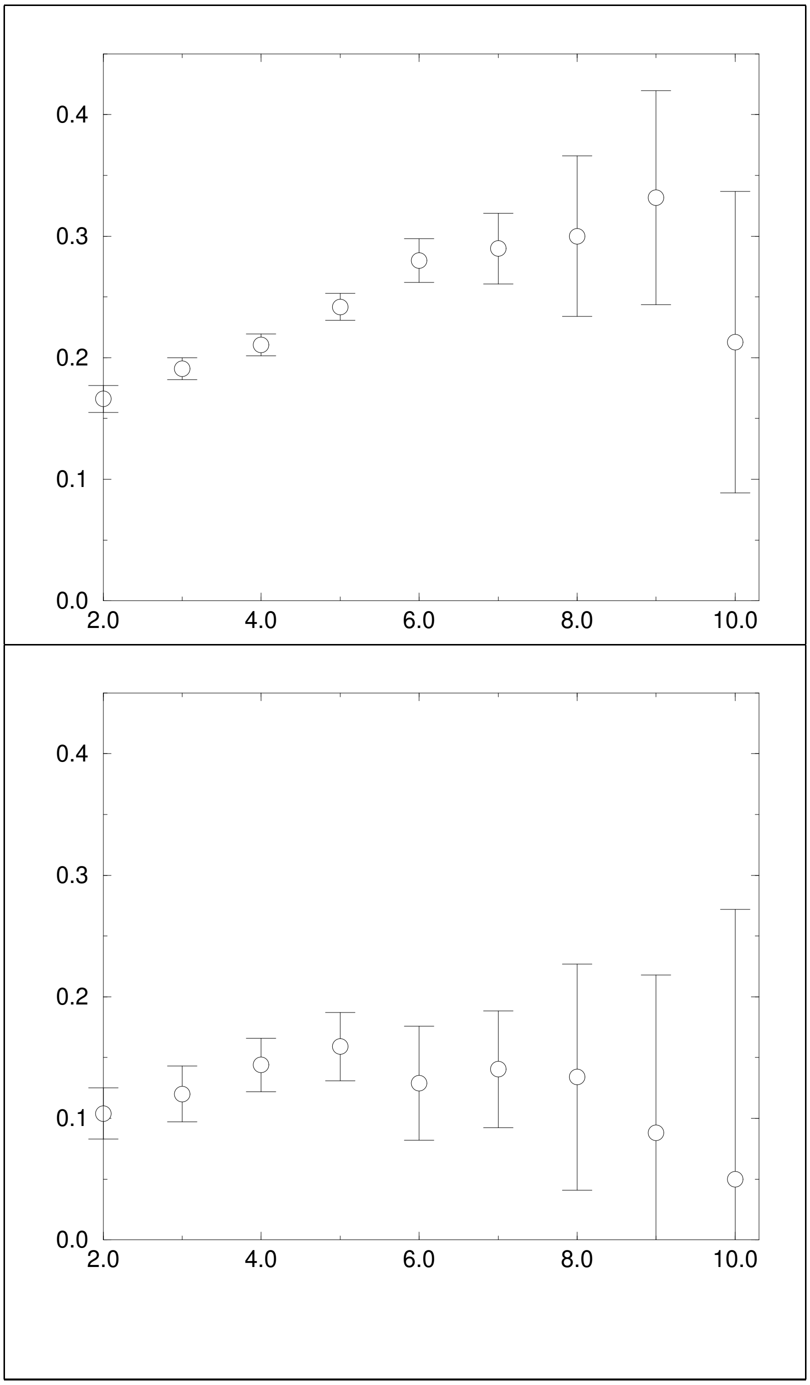

Table 10.5: b meson masses taken from [27] and simultaneous fits at $\beta = 5.7$

κ	Mass from [27]	Mass from our Fits
0.13843	0.912(6)	0.924(3)
0.14077	0.875(6)	0.883(9)

10.6 Discussion

We compare the results obtained with the finite differences between the masses calculated at the two hopping parameters. These masses were calculated by Michael and Peisa in [27]. We also compare these measurements with the results of the fitting procedure for the two exponential fits on the larger lattices. This data is presented in Table 10.5.

The finite difference estimate from this data is 0.31(6) (or from our own determination the masses from the fitting procedure, 0.34(8)) which should be compared with our determination of X_{00}.

For the heavier hopping parameter a good agreement with the finite difference result was obtained. The plateau is clearly seen in the ratio, $R(t)$, using the improved basis. This gives a measurement of 0.30(6) at $t = 8$. Errors are comparable with the finite difference method and this indicates that the two methods are at least comparable in efficiency. The fitting method produced a slightly low estimation of the matrix element (0.20(8)) though not one that is statistically significant. This could be improved by using more rigorous determination of the coefficients and excited state masses from the two point functions which is an approach we take in other three point correlation fits in later chapters.

The lighter hopping parameter provided a slightly more disappointing result. It is clear from the graph of the ratio as a function of lattice time that, as well as being significantly more noisy, a plateau is not seen to develop in the same time region as for the heavier case and larger time correlations appear unreliable. We attribute this to the small statistics of the study and the

Table 10.6: Determinations of $\frac{dM}{d\kappa^{-1}}$ for vector and pseudoscalar mesons.

κ	M_{PS}	$\frac{dM_{\mathrm{PS}}}{d\kappa^{-1}}$	M_{Vec}	$\frac{dM_{\mathrm{Vec}}}{d\kappa^{-1}}$
0.13843	0.736(2)	1.56(22)	0.938(3)	0.3(4)
0.14077	0.529(2)	1.97(27)	0.815(5)	1.9(9)

increased noise of the stochastic estimators with decreasing quark mass. Both methods give estimates of around 1.0 - 1.5 with similar errors. We expect the value to be roughly constant over this range of κ.

The equivalent procedure has been performed for light-light vector and pseudoscalar mesons using the same ensemble by my collaborator C. Michael. This is discussed in more detail in [56] and we present these results in Table 10.6 as they are of interest for comparison. Here the finite difference in the same units are given by 1.48 and 0.88(1) for the two states respectively. The determined derivatives agree well with the finite difference method. In Chapter 12 we will go on to apply the sum rule in QCD with dynamical fermions where the sea and valance quark masses can be varied independently. There we will examine the role of the sea quarks in hadron masses.

Chapter 11

Hadron Spectroscopy with Disconnected Loops

11.1 Introduction

In Chapter 6 we introduced a method of estimating elements of the inverse fermion matrix using Z_2 noise vector sources. The elements we focussed on in that discussion were those involved in the construction of disconnected loop operators. In this, and the next chapter, we apply this method to spectroscopic topics to examine both the efficiency of the method and to try to determine quantities that are otherwise inaccessible using other approaches and realistic computational time.

In Chapter 5 we stated that in order to properly determine the mesonic correlation functions for flavour singlet mesons, we had correctly, to evaluate all possible contractions of the quark fields arising in the operators. This includes both the connected and disconnected two point correlation functions. We identify the disconnected correlation functions as those in which the quark lines are traced to the same point on the lattice (for local operators such as those considered here). In usual determinations of the mesonic spectrum only the connected part is evaluated corresponding to flavour non singlet mesons such as the $\pi^{\pm}$. This is appropriate, even for the flavourless π_0 which is approximately degenerate with the others in the triplet. In the real world the flavour singlet mesons are not degenerate with the pions, and we explore this feature in the context of flavour symmetric quarks. In this regime the mass splitting occurs as a result of disconnected loop correlations contributing to the meson masses.

In contrast to the flavour non-singlet hadron spectrum, of which many lattice calculations have been made, first principles determinations of the flavour singlet sector are rare - a testimony to the difficulties involved. Notable measurements of the η' mass and/or the η invariant (m_0) include that of the Japanese collaboration, using both 'brute force' - through many propagator inversions [57], and gauge invariance with an extended volume source [58]. They have performed a relatively high statistics calculation in quenched QCD which can be regarded as the benchmark for subsequent work in this area. In the dynamical simulation sector, Kilcup *et al.* [59] have calculated the η' mass in full QCD with staggered fermions. Their measurements demonstrate the effects of unquenching quite conclusively. Other approaches to the problem include that of Frezzotti *et al.* who have used a pseudofermion technique not unlike that which we described in Chapter 6. They see little dependence on flavour number in the parameter regime investigated. To date no calculation has been published for dynamical QCD with clover improved Wilson fermions. We provide an investigation with modest statistics suggesting that a more comprehensive calculation with this method would provide a framework for an accurate measurement.

In this chapter we use the Z_2 noise vector sources to construct disconnected correlator functions and attempt to estimate the $\eta' - \pi_0$ mass splitting through the consideration of correlation ratios. We examine the spectrum on (clover improved) Wilson dynamical fermion lattices which have two degenerate flavours of light quark and hence contain two flavourless eigenstates. We examine the splitting between these two states, which we label the π^0 and η'. We also comment on the method as a probe, examining the effects of dynamical fermions on the simulation.

11.2 The η' Meson

In the continuum QCD vacuum there are three mass eigenstates of flavourless mesons associated with an approximate SU(3) flavour symmetry. For the pseudoscalar octet they are the isospin 1, π^0 and isospin 0, η and η'. In the quark model they are mixings of $u\bar{u}$, $d\bar{d}$ and $s\bar{s}$ states. The mixings of these states correspond to the diagonalisation of the mass matrix. There are two sources of contribution to the mass matrix that cause such a mixing of the naive basis; a breaking of the SU(3) flavour symmetry and the consideration of both connected and disconnected diagrams. The second of these terms is significant because it represents off diagonal elements of the mass matrix in the naive basis.

In reality the flavour symmetry is broken and we see the u and d quarks with an approximate degeneracy and a higher massed strange quark. If the effect of the disconnected terms is small in contrast with the mass splitting, then one might expect a heavier meson whose higher mass is due to its basis being almost entirely $s\bar{s}$. This is experimentally seen to be the case for the vector octet, which has a correspondingly heavy 'hidden strange' ϕ state. This is termed 'magic mixing'.

In the pseudoscalar case the mesons are not seen to be magically mixed and thus we deduce that the matrix diagonalisation must be heavily influenced by the disconnected terms.

In lattice QCD we do not represent the quark masses realistically, indeed at the current time only dynamical simulations with mass degenerate sea quarks are available. This has some advantages in that it allows us to examine the disconnected contribution directly.

For N_f degenerate flavours of fermions the elements of the matrix will not depend on the flavours of the quarks in the basis, and we label the two types of contribution, C (connected) and D (disconnected). In the naive basis, $u\bar{u}$, $d\bar{d}$ etc the correlation matrix $\mathcal{M}$ is;

$$\begin{aligned} \mathcal{M}_{ij}(i \neq j) &= -D \\ \mathcal{M}_{ii} &= C - D \end{aligned} \tag{11.1}$$

This matrix can be diagonalised easily so that the diagonal elements corresponding to the eigenstates of the system are C and $C - N_f D$. Ideally, we would like to take gauges with $N_f = 3$ so that our calculation is directly comparable with the experimentally observed quantities - states which are mixings of the three lighter flavours, up down and strange. Unfortunately, this is infeasible using current methods of Monte Carlo evaluation, where we are limited to even numbers of dynamical flavours. For $N_f = 2$, this corresponds to a basis of $\frac{1}{\sqrt{2}}(\bar{u}u - \bar{d}d)$ and $\frac{1}{\sqrt{2}}(\bar{u}u + \bar{d}d)$ respectively.

We investigate these two correlation functions on $N_f = 2$ lattice gauge theory, assessing the relevance of the disconnected term to the pseudoscalar octet. We label the heavy singlet state the η' for its comparable role to the η' in experimental high energy physics. The lighter flavourless meson is the π^0 as it is degenerate with the flavoursome $\pi^{\pm}$ and maintains its role in completing the isospin triplet.

We expect the behaviour of the correlations to describe the masses of the state in the usual way, that is,

$$\langle C(t) \rangle = c_0^2 e^{-m_{\pi^0} t} + \dots \tag{11.2}$$

$$\langle C(t) - N_f D(t) \rangle = c_0^2(\eta') e^{-m_{\eta'} t} + \dots \tag{11.3}$$

Whilst in principle it is possible to evaluate the η' mass from the correlation function in the usual manner we do not expect to obtain a definitive calculation of the mass, as the disconnected correlator is exceedingly noisy. We proceed by examining the ratio of the two correlation functions which is a quantity examined in other comparable studies.

$$\begin{aligned} \frac{N_f D(t)}{C(t)} &= \frac{C(t) - c_0^2(\eta') e^{-m_{\eta'} t} + \dots}{c_0^2 e^{-m_{\pi^0} t} + \dots} \\ &\approx 1 - \frac{c_0^2(\eta')}{c_0^2} e^{-\Delta m t} \end{aligned} \tag{11.4}$$

Here the second line follows from the neglect of excited state contamination which we expect to be true for larger t (though we acknowledge that we have no guide as to the proximity of the excited states). Δm is the mass difference between the flavourless mass states. One immediate feature of this formalism is the expected saturation of the ratio for large t. This is an indication of the correct behaviour of a dynamical theory and a condition of unitarity in the theory, absent in quenched studies. For the quenched case the relationship is linear in t. We can understand this as being a consequence of the inability of the vacuum to generate quark loops in the vacuum. We can follow the example of the previous chapter, parameterising the process as a matrix element, X, such that the correlation function $D = \sum_t e^{-m_\pi (t-t_1)} X e^{-m_\pi (t_2 - t)}$ so that the quenched behaviour is given by,

$$\frac{D(t)}{C(t)} \propto t \tag{11.5}$$

The properties and origin of X can be understood through the summation of virtual vacuum quark loops. This results in an effective propagator $G_{\eta'}$ whose pole is shifted by some amount m_0 in quadrature with respect to the usual octet mass, which in this simple model, is the lighter flavourless state, rather than the η state of experimental physics. This shift has been studied in large N_C perturbation theory and is believed to be related to instanton effects through through

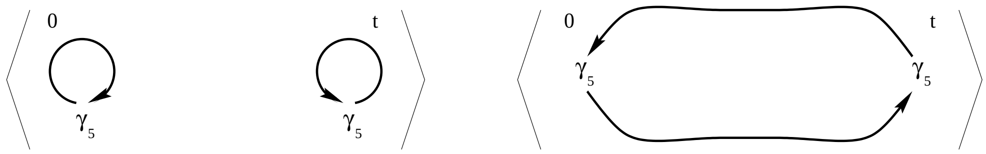

(a) Disconnected two point corrolator (D2) (b) Connected Pion Correlator (C)

Figure 11.1: Schematic representation of the disconnected and connected pseudoscalar correlation functions

the Witten-Veneziano formula [3]. For the quenched case the generation of vacuum loops is impossible, other than those inserted by hand through an interpolating field. The functional behaviour in this case arises directly from the truncation of the summation and the slope of $R(t)$ is expected to be $m_0^2/2m_\pi$.

11.3 Disconnected Correlation Functions

In Chapter 6 we discussed the use of Z_2 noise in constructing the disconnected loop operators. We employ this technique here in generating the appropriate correlation functions described above. Z_2 source vectors are generated on a timeslice (t) and the lattice Dirac equation is solved with this source. The resulting propagator (G) obtained is used to calculate the relevant products which are constructed inside the solver program and recorded before discarding the propagator. Relevant to this calculation we calculate both the disconnected two point function projected onto zero momentum;

$$\mathcal{L}_{\mathcal{PS}}(t) = \sum_x \mathrm{Tr}\zeta_i(x,t)^*(G(x,t)\gamma_5)_i \tag{11.6}$$

where $\mathcal{L}_{\mathcal{PS}}(t)$ is an estimator of the disconnected loop. Here the source is distributed over the timeslice, t, and other indices (spin, colour etc.) are represented in the index i. We average over both the usual source (given above) and the same when a source $\gamma_i\gamma_5\zeta$ is used, in order to reduce the variance of the pseudoscalar loop estimates as discussed in Chapter 6. We also construct the connected correlator from the source plane to every other timeslice,

$$C_{\mathcal{PS}}(t,t_1) = \sum_x |G_i(x,t_1)|^2 \tag{11.7}$$

as described for the pion propagator in Chapter 5. We note that better determination of the pion correlation function is obtained through averaging over the combinations $C_{\mathcal{PS}}(t_2,t_1)$ and $C_{\mathcal{PS}}(t_1,t_2)$ which should be symmetric in t. We are then able to construct estimates of the correlation functions,

$$\begin{aligned} R(t = t_2 - t_1) &= \frac{N_f D(t)}{C(t)} \\ &= N_f \frac{\langle \mathcal{L}_{\mathcal{PS}}(t_1)\mathcal{L}_{\mathcal{PS}}(t_2)\rangle}{\langle C_{\mathcal{PS}}(t_1,t_2)\rangle} \end{aligned} \tag{11.8}$$

The factor of N_f is inserted by hand. We depict these two correlation functions in Figure 11.1.

The signal is dominated by the intrinsic variance associated with the disconnected loop operator. With regard to this we relax the convergence criterion of the solver program. The MR solver algorithm is known to converge non-monotonically such that for two few iterations systematic errors may be introduced. Thus, we examine the estimates of the trace of the inverse matrix (actually the even-odd preconditioned matrix) as a function of the residual, in order to determine at what point errors from the more approximate solution are vastly outweighed by the intrinsic fluctuations which we are attempting to correlate. We find that, stipulating a residual ($\frac{|MG-\zeta|}{|\zeta|}$ where ζ is the source), of 5×10^{-5} produces trace estimates accurate to around four orders of magnitude smaller than the fluctuations under investigation. This is consistent with observations by the SESAM collaboration [61] who used a slightly less accurate solve with a residual of 10^{-4} in their calculations of a different quantity, also involving disconnected loops, using a similar Z_2 method. This enables us to use many more Z_2 samples, gaining improved results for a similar computational time.

The computation was performed on a Cray T3D system on 256 processor elements. The computational cost of inversion with this target residual was measured on 32 processor elements both with MR inversion and Bi-Conjugate Gradient methods. The convergence of the MR solver was shortened from that using the residual which is usually employed (10^{-7}), by a factor of 2, and an improvement through the use of the Bi-Conjugate Gradient algorithm over MR, of around a 30% with the relaxed convergence (compared with a 40% improvement for the usual residual).

Table 11.1: Details of Lattices and Z_2 samples used to estimate disconnected loop correlators. $C_{SW} = 1.76$ for all sets.

β	$\kappa_s(\kappa_v)$	Lattice Dimensions	Independent(total) Z_2 samples per time plane.	Number of Lattices	Total No. of Inversions
5.2	0.1390	$12^3 \times 24$	20(40)	24	19200
5.2	0.1395	$12^3 \times 24$	32(64)	20	30720
5.2	0.1398	$12^3 \times 24$	32(64)	20	30720

We generate samples on three sets of dynamical gauges with $\kappa_s = \kappa_v$ as detailed in Table 11.1. These configurations are separated by approximately 200 update trajectories.

11.4 Results and Discussion

We were able to obtain a signal using this method, though it is apparent from the data that a higher statistics study is needed to obtain a reasonable signal in the region where the ratio will saturate demonstrating that unitarity is satisfied. We estimate from the data that around eight times the statistics would be required to determine the correlation functions in this region.

Also examined were the correlations of other disconnected loops with different quantum numbers, including, notably the vector, which would allow calculation of the flavour singlet vector meson spectrum. No signal was obtained for this quantity, or indeed for any other of the sixteen Γ matrix combinations, aside from the scalar and pseudoscalar operators.

To explore this, we examine the data obtained from each sample $\sum_{\text{sites}} \text{Tr}M^{-1}\Gamma$. We expect the variance of the measurements to originate from two sources; the error from the Z_2 method($\frac{\sigma^2_{Z_2}}{N_{\text{samples}}}$) and the fluctuations between gauges or timeslices (σ_{sig}) which is a property of the configurations used. Assuming the central limit theorem holds on the measurements made

Figure 11.2: The Ratio $R(t)$ vs. time in lattice units at the three κ values investigated.

$\kappa_s = 0.1390$

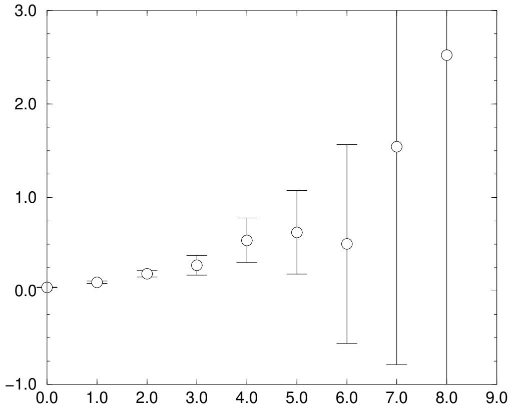

$\kappa_s = 0.1395$

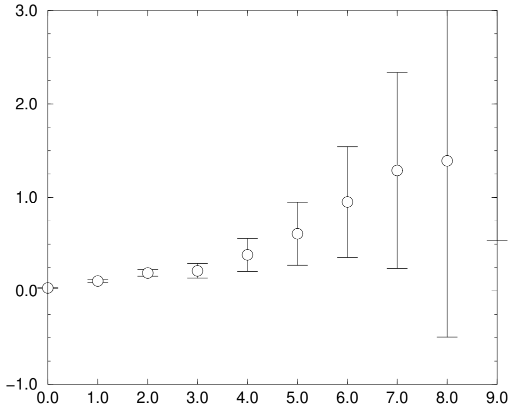

$\kappa_s = 0.1398$. The curves are bounds on the expected behaviour, from fits to $1 - Ae^{-\Delta mt}$ and are intended to show the expected region of saturation

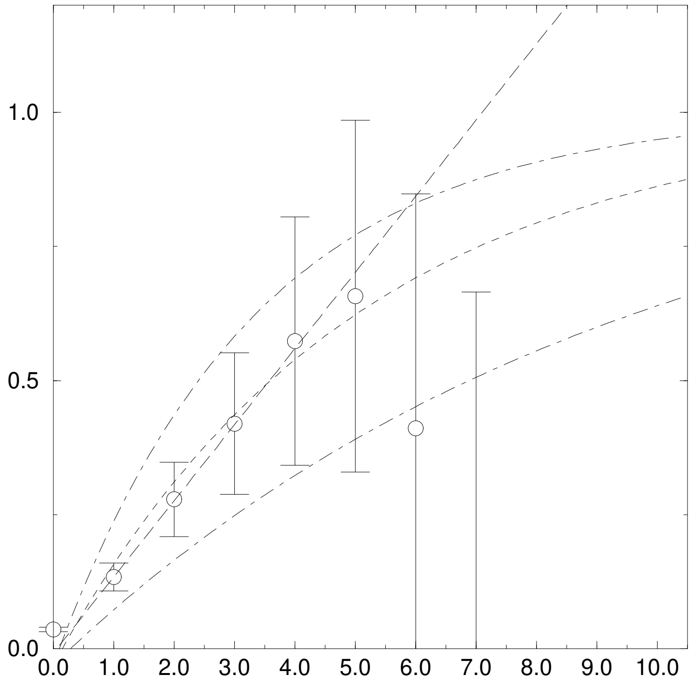

Parameters of the fit are given in Table 11.2. A linear fit indicates a slope of 0.14(6).

we expect,

$$\sigma_{S_1}^2 = \sqrt{\sigma_{Z_2}^2/N_{\mathrm{samples}} + \sigma_{\mathrm{sig}}^2} \tag{11.9}$$

We compare the measured errors of the disconnected loop operator overall (S_1) with the error on the on the quantity on a timeslice (S_2) arising from the Z_2 estimates of that quantity. These figures are given below for the pseudoscalar and vector case;

Operator	κ	S_1	S_2	$\sum_{\mathrm{sites}} \mathrm{Tr} M^{-1}\Gamma$
Pseudoscalar				
	0.13900	25.66	15.70	2.3
	0.13950	23.99	12.64	1.2
	0.13980	25.25	12.77	-1.8
Vector				
	0.13900	14.1	14.24	0.1
	0.13950	12.2	12.64	-0.8
	0.13980	11.5	11.43	-0.8

We see that the errors from the Z_2 estimation are dwarfed by the intrinsic noise of the signal for the pseudoscalar case. For the vector the errors are comparable, which is consistent with the lack of signal. With this in mind the optimal progression would be to reduce the number of Z_2 inversions per gauge by a factor of two or four and increase the number of gauges considerably. This suggests that the Z_2 method is reasonably successful and an appropriate method with which to study the η' meson.

In Figure 11.4 we plot effective masses of the η' from the ratio of the correlation functions (Equation 11.3) on adjacent timeslices. We perform a two exponential fit to the data using time values of $1 \to 5$. As the correlations do not reasonably extend beyond $t = 5$ there is realistically insufficient data for this to be a rigorous determination, and excited state contamination is largely uncontrolled. We present it only as an indication of what might be expected from a more comprehensive study. We do see some evidence of plateauing behaviour in the masses though there is the obvious concern that this may be attributable to the pion-like contribution to the correlation function with extra noise from the disconnected term. For this reason we plot the

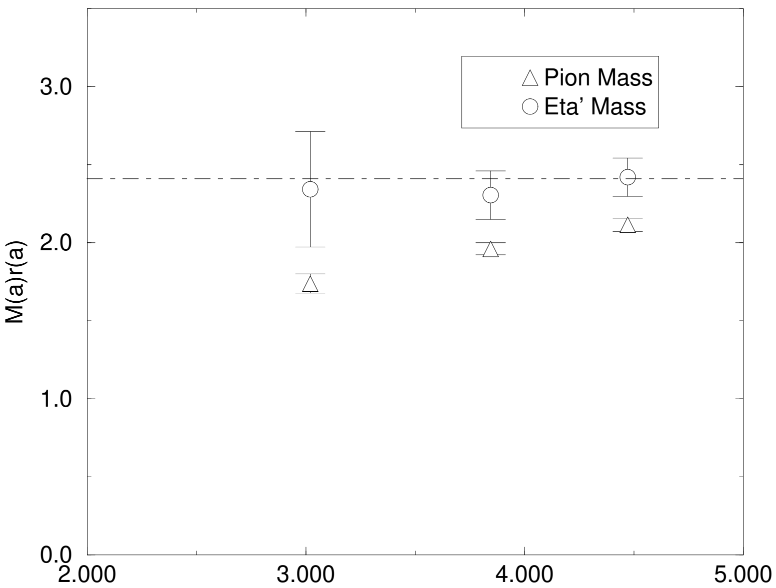

Figure 11.3: A comparison of the behaviour of the π and η' masses (from fits to ΔM) with variation in the quark mass. The abscissa is $(r_0 m_\pi)^2$. The errors on the η' are relative to the pion mass and should not be considered absolute. The experimental measurement of the η' mass is shown as a dotted line.

effective mass from the local pion operator signal on the same graph. This is consistently lower in size by around 0.1 in lattice units which indicates a splitting of the η' from the pion and is more pronounced for $\kappa = 0.1398$. This is in agreement with fits made to the exponential form, $R(t)$, which give estimates of the splitting Δm. We tabulate the mass estimates from both approaches in Table 11.2. It should also be noted that with increasing κ_s there is a shortening of the lattice spacing indicating that there is probably worse excited state contamination in the larger hopping parameters.

To illustrate this, in Figure 11.3 we plot the splitting between the pion mass determinations, and the η' mass from consideration of the estimates of Δm as dimensionless quantities, scaled by r_0, against the square of the dimensionless pion masses. In a quenched theory the relationship should be linear as we discussed in our treatment of the adjoint meson. This shows the pion mass falling in the limit of light quarks compared to the η' though with a large uncertainty in the behaviour in the latter.

In contrast to other studies, such as that of Kuramashi *et al.* [58], we have obtained less

Table 11.2: Estimates of the η' mass from exponential decay of the correlation function, $(M_{\eta'})$, and from fits to the functional form of $R(t) = 1 - Ae^{-\Delta M t}$, (ΔM). Fit ranges are from $t = 1 \rightarrow 5$. The comparative Pion masses, (M_π), and values of r_0 to scale the data are taken from [62].

κ	M_π	$M_\pi r_0$	$M_{\eta'}$	$M_{\eta'} r_0$	ΔM
0.13900	0.707(5)	2.115(42)	1.21(25)	3.05(76)	0.10(4)
0.13950	0.558(8)	1.961(38)	0.91(15)	3.12(51)	0.10(4)
0.13980	0.476(16)	1.738(61)	0.88(27)	3.21(98)	0.20(10)

accurate estimates of the relevant mass and a noisier signal. However, this is from far fewer measurements. Our determinations of the slopes of the ratio, $R(t)$ are consistent with their quenched calculation. Kilcup *et al.* have observed saturation in this ratio which we have not. This is unsurprising when we consider that our signal has degenerated to noise in the region that we expect saturation to occur. Their measurements employed sea quarks much closer to the chiral limit using the Kogut-Susskind formulation. Thus, they observe saturation at lower t-values (around $t = 4$) where correlations are more easily determined.

We have not been able to determine whether the simulation behaves as a dynamical one. That is the data points obtained are consistent with linearity in the quantity $R(t)$ (as shown for $\kappa_s = 0.1398$ in Figure 11.2) as is expected of a quenched theory. In such a scenario we may assert that the sea quarks are too heavy to make a significant contribution to the η' propagator.

Adding extended, fuzzed, operators to the correlation matrix would allow better control of the excited state contribution to the functions and may give a more reliable estimate even from a small statistics study. However a larger ensemble of gauge configurations is also needed. We refer to the observations of SESAM [61] who assert through their experiences that γ_5 disconnected loop type measurements require a minimum of 100 gauges for reliable determinations to be made. This is consistent with our own estimates of the statistics needed to observe correlations in the physically interesting region where dynamical quark effects may be seen.

Figure 11.4: Effective lattice mass of the η' from the ratio of correlation functions on adjacent timeslices. Also shown (dotted) are determinations of the effective pion mass from the local pion correlators for comparison. Errors on this latter quantity are not shown, but are small in contrast with the η' masses

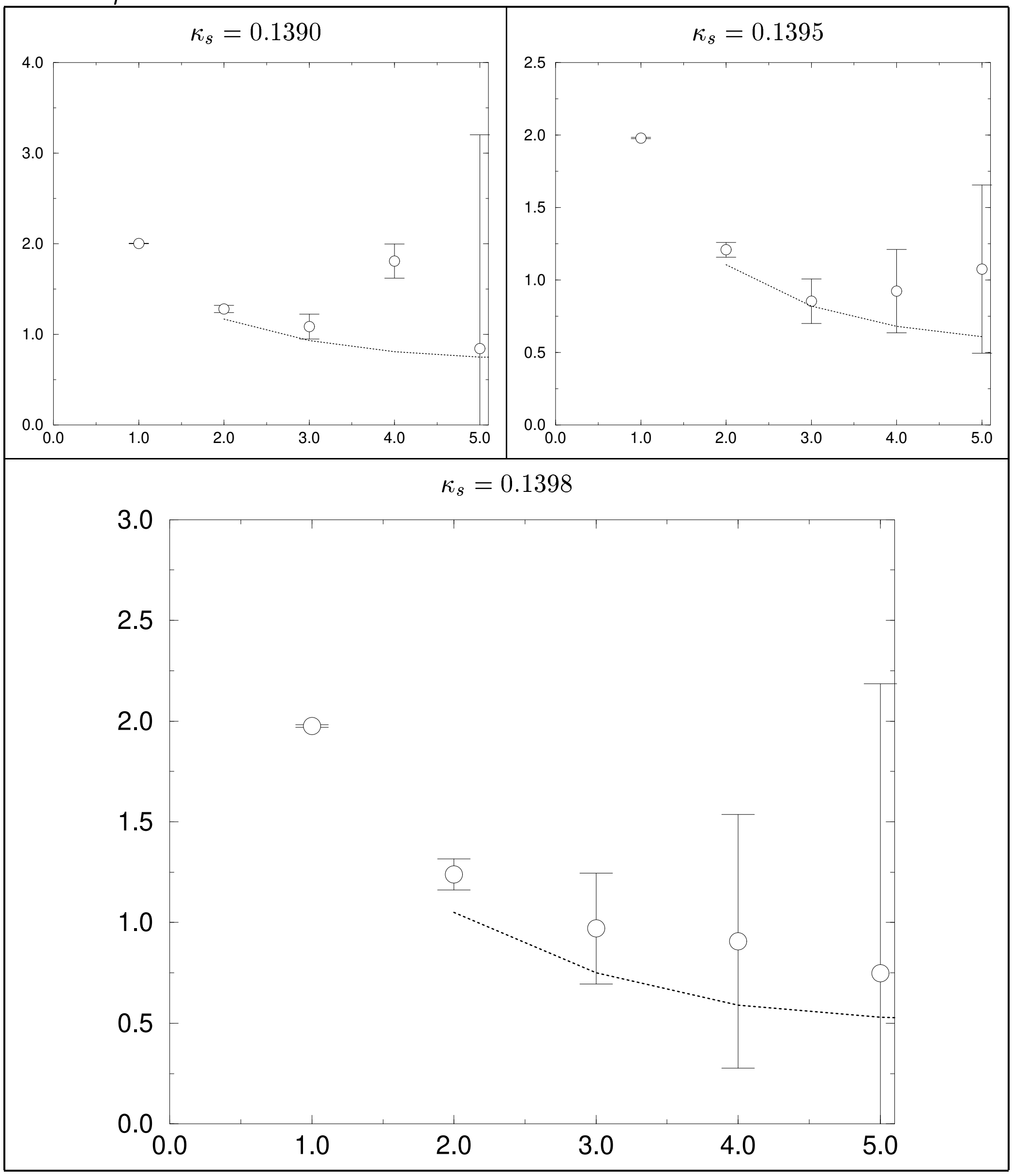

Chapter 12

Mesonic Mass Dependence on κ_{sea} in Full QCD

12.1 Introduction

In chapter 10, we discussed a method of determining the hadronic mass dependences on the valence quark mass. We differentiated the functional integral and then evaluated the resulting correlation function. This was applied to the b meson, and the vector and pseudoscalar mesons, with reasonable results from a low statistics study.

An obvious progression of this is to examine the same process in a dynamical simulation. Here hadronic masses depend both on the valence quark mass, κ_v, and on the simulation (or sea) quark mass, κ_s. There are obvious advantages to the successful implementation of this procedure, as dynamical systems are computationally expensive to generate and, with decreasing quark masses, become even more so. The chiral behaviour of such systems is as yet poorly understood, so that extra information predicting the behaviour of the system under a change of parameters is very useful. This should be compared with work by Irving *et al.* [55] who propose a general method of examining the relationship between lattice observables and the parameters of the action, applying this to Wilson fermions and changes in κ_s.

We will demonstrate that the ingredients of the correlations relevant to such a determination are disconnected loops similar to those with which we examined the η' in the previous chapter together with the usual two point correlators. We construct such interpolating fields as are required using the Z_2 noise method of Chapter 6. In fact all required components were computed at almost no extra computational cost simultaneously with those for the η' correlator. We evaluate the correlation functions on the same data sets as were used in the previous chapter, and see that the method is successful though in slight disagreement with existing measurements of the spectrum. The results indicate that higher statistics are necessary to determine such quantities with more accuracy than the finite difference method with which we compare our results. This however, employed a configuration sample of about five times larger than our own.

12.2 κ_s Dependence

In dynamical simulations the action is given by $S = S_{\text{Wilson}} + \bar{\psi}M\psi$ where M contains factors of the hopping parameter κ. The normalisation constant of the generating functional, Z, also contains the exponentiated action and thus has a κ dependence. Explicitly including all factors, the hadronic correlation function for a meson in dynamical QCD with N_f flavours of degenerate sea quarks is given by;

$$C(t = t_2 - t_1) = \frac{1}{Z(\kappa)} \int \mathcal{D}U\mathcal{D}\bar{\psi}\mathcal{D}\psi H^{\dagger}(t_1)H(t_2)e^{-\beta S_g - \Sigma_1^{N_f} \bar{\psi}M(\kappa)\psi} \tag{12.1}$$

For mesonic correlators, the simplest choice of H is a bilinear in the fields ψ with appropriate quantum numbers. We differentiate the functional integral *before* integrating out explicit fermion degrees of freedom, and thus formally, the interpolating fields, H, have no dependence on κ. This contrasts with the earlier case for the quenched b meson, where the fields were substituted with the κ dependent propagator, before the derivative was taken. We can thus take the derivative with respect to κ^{-1} to give,

$$\begin{aligned} \frac{dC(t)}{d\kappa^{-1}} &= \frac{1}{Z(\kappa)} \int \mathcal{D}[U,\bar{\psi},\psi]H^{\dagger}(t_1)H(t_2)\frac{de^{-S}}{d\kappa^{-1}} + \int \mathcal{D}[U,\bar{\psi},\psi]H^{\dagger}(t_1)H(t_2)e^{-S}\frac{d\frac{1}{Z(\kappa)}}{d\kappa^{-1}} \\ &= \frac{1}{Z(\kappa)} \int \mathcal{D}[U,\bar{\psi},\psi]H^{\dagger}(t_1)H(t_2)N_f\bar{\psi}\psi e^{-S} - \\ &\qquad \frac{1}{Z(\kappa)} \int \mathcal{D}U \left(\int \mathcal{D}[\bar{\psi},\psi]H^{\dagger}(t_1)H(t_2)e^{-S} \int \mathcal{D}[\bar{\psi},\psi]N_f\bar{\psi}\psi e^{-S} \right) \end{aligned} \tag{12.2}$$

In the derivative of the exponential we can use the same choice of normalisation of the fields, such that $\tilde{M} = \frac{1}{\kappa} + \tilde{D}$, as we did in Chapter 10 to simplify the procedure. We write this expression as;

$$\frac{dC(t)}{d\kappa^{-1}} = \sum_{t_i} \left(-C_3(t,t_i) + N_f D_3(t,t_i)\right) \tag{12.3}$$

The term C_3 is directly analogous to that described for the b meson in the quenched case, though the insertion is summed over the possible placement in either of mesons quark lines. The other contractions of the ψ fields in C_3 do not contribute if we consider the meson to be flavoursome e.g. $\langle \bar{\psi}_d \psi_u \rangle = 0$. C_3 is given, on the integration of fermionic fields as,

$$C_3(t,t_i) = \langle \mathrm{Tr}(G(0,t_i)G(t_i,t)\Gamma G(t,0)\Gamma) + \mathrm{Tr}(G(0,t)\Gamma G(t,t_i)G(t_i,0)\Gamma) \rangle \tag{12.4}$$

The second of the terms on the right hand side is shown in Figure 12.1(a). We identify the term $C_3(t,t_i)$ as being associated with the valence quark mass dependence which we derived in chapter 10. This is not directly accessible with the Z_2 method we are employing as it requires the storage of each propagator and we do not examine it further in this work. A small statistics measurement has been performed using the pseudofermion propagator method for comparative purposes and details of this are given in [56].

The term D_3 is the product of the 2 point function C with a disconnected loop, shown in Figure 12.1(b). The expectation of the disconnected loop is non zero and as such we consider fluctuations in this quantity about the measured average. Thus, the correlation function is constructed according to,

$$D_3(t,t_i) = \langle \mathrm{Tr}(G(0,t)\Gamma G(t,0)\Gamma)\mathrm{Tr}G(t_i,t_i) \rangle - \langle \mathrm{Tr}(G(0,t)\Gamma G(t,0)\Gamma) \rangle \langle \mathrm{Tr}G(t_i,t_i) \rangle \tag{12.5}$$

where there is an implicit summation over all spatial indices and the trace is over spin and colour degrees of freedom in the usual way.

We identify this remaining correlator as representing contributions to the change in the mesons mass with variation in the simulation quark mass κ_s. Moreover this variation is performed independently of the valence quark mass which should remain fixed for comparative purposes. This is best thought of as a probe into how the behaviour of the mass of an $s\bar{s}$ meson depends on the masses of the lighter quarks (u,d etc) whose vacuum loop processes influence the states propagation. Unfortunately whilst κ_v is of strange quark order, so also is κ_s.

With this in mind we examine this latter term. We proceed as we did in chapter 10, obtaining the compliment of Equation 10.10;

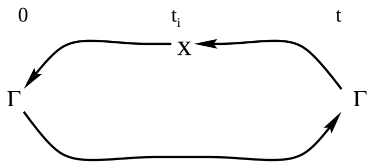

(a) 3 Point Connected Mesonic Correlator

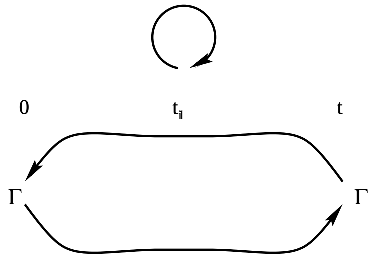

(b) 3 Point Disconnected Mesonic Correlator

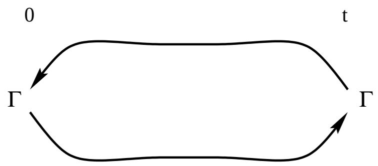

(c) 2 Point Mesonic Correlator

Figure 12.1: Diagrams involved in $\frac{dM}{d\kappa^{-1}}$. (a) $\rightarrow$ (c) are labelled C_3, D_3, and C in the text.

$$\frac{dC(t)}{d\kappa^{-1}} = c_0^2 \frac{dm_0}{d\kappa^{-1}} t e^{-m_0 t} + c_0^2 \frac{dc_0^2}{d\kappa^{-1}} e^{-m_0 t} + \ldots \tag{12.6}$$

and recovering;

$$\frac{dm_0}{d\kappa_s^{-1}}|_v = N_f X_D = N_f \frac{\langle D_3(t, t_i) \rangle}{\langle C(t) \rangle} \tag{12.7}$$

Where X_D is the matrix element corresponding to the disconnected diagram 12.1(b).

12.3 Correlation Functions

We focus on the vector and pseudoscalar mesons with a local interpolating field $H = \bar{\psi}\Gamma\psi$, with $\Gamma = \gamma_i, \gamma_5$ creating pi and rho mesons respectively. In order to compute the quantity of Equation 12.7 we are required to evaluate both the two and three point functions for each type of meson. We again employ the Z_2 noise method described previously, which enables us to calculate the disconnected loops required. Unlike noise volume methods, the use of timeslice sources also allows the simultaneous computation of the two point correlators between any two timeslices with accuracy comparable with other methods.

We elaborate on this point. The pseudoscalar two point function, which was also used in our examination of the η' state, is simply the square of the propagator to a timeslice t, and summed over spatial indices as described in Equation 5.18. This is calculated for every timeslice source and provides pion propagators between any two timeslices. The vector meson requires a multiplication with γ_i at source and sink (or $\gamma_5\gamma_i$ after using the propagator manipulation of Equation 5.17). This is somewhat awkward as the source is a noise and thus, individual Dirac components are not identifiable. We recall that in section 6.4.2 we introduced a second related source as a variance reducing measure. We can use such an appropriate related source,

$$\zeta' = V\zeta \tag{12.8}$$

so that the solution of the Dirac equation implies that,

$$G' = M^{-1}V\zeta \tag{12.9}$$

Thus we examine the product,

$$\begin{aligned}
\langle GG'X\rangle &= \langle M^{-1}\zeta(M^{-1}\zeta')^\dagger X\rangle \\
&= \langle M^{-1}\zeta\zeta^{*'}(M^{-1})^\dagger X\rangle \\
&= M^{-1}\langle\zeta\zeta^*\rangle V^\dagger(M^{-1})^\dagger X
\end{aligned} \tag{12.10}$$

and we can see that the appropriate choice of $V = X = \gamma_5\gamma_i$ gives the correct correlator for a vector meson with associated noise from the $\langle\zeta\zeta^*\rangle$ term.

The disconnected loops are given by M^{-1} which is estimated by $\frac{1}{N_S}\sum_{N_S}\zeta_i^* G_i$ for N_S samples of the Z_2 noise as discussed in Chapter 6. Thus the components needed are given by,

$$C_{\mathrm{P}}(t_s,t) = \frac{1}{N_S}\sum_{N_S}\sum_x \mathrm{Tr}G(x,t)G^\dagger(x,t) \tag{12.11}$$

$$C_{\mathrm{V}}(t_s,t) = \frac{1}{N_S}\sum_{N_S}\sum_x \mathrm{Tr}G(x,t){G'}^\dagger(x,t)\gamma_5\gamma_i \tag{12.12}$$

$$L_S(t) = \frac{1}{N_S}\sum_{N_S}\zeta_i(x)G_i(x,t) \tag{12.13}$$

These are computed for each gauge, source plane t_s, and sink plane t, and stored. The correlations functions are constructed from these as,

$$D_{P,3}(t-t_s,t_i) = \langle C_P(t_s,t)L_S(t_i)\rangle - \langle C_P(t_s,t)\rangle\langle L_S(t)\rangle \tag{12.14}$$

for the pseudoscalar case, and similarly for the vector. In the second term we have explicitly accounted for the non zero expectation of $L_S(t)$. The correlation $D_{P,3}$ takes the form of a correlation between fluctuations in $L_S(t)$, which is the chiral condensate, with those in the mesonic propagator. It is found that this is actually an anti-correlation with an increase in one of the quantities being linked with a decrease in the other. The strength of these fluctuations indicates the strength of the dependence of the meson mass on the quark mass which is, perhaps, surprising. The mesonic expectation in the denominator of Equation 12.7 is simply averaged over the gauge configurations and timeslices;

$$C(t-t_s) = \langle C_P(t_s,t)\rangle \tag{12.15}$$

In principal fuzzed sources could (and indeed should) be constructed at the source and sink to provide control over excited state contamination. In this study, which should be considered a preliminary investigation of the method to a higher statistics study, only local operators are employed. We employ fitting procedures described below to try to estimate the ground state components.

12.4 Results and Discussion

The ensemble employed is the same as that given in the last chapter in Table 11.1. Such that the derivatives are examined at three values of κ_s.

In order to control excited state contributions we perform a fitting procedure. We consider a high statistics study of the two point meson correlators [62] with fuzzed and local operators and perform two exponential fits to this data. This provides us with the appropriate overlap coefficients ($c_l^{(k)}$) for the local operators, which we expect to be identical to those arising from the local Z_2 correlators which we have used. Determinations of the ground and excited state masses were also obtained from this source. We used these values in a fit to the three point

Table 12.1: The matrix element, $\frac{dM}{d\kappa^{-1}}$ in $N_f = 2$ QCD, $\beta = 5.2$, from fits to the three point function. Meson masses are taken from [62]. Fits are made from $t = 4 \to 12$ and include data from asymmetric placement of t_i. In these cases data is used where the shortest propagating leg has a minimum length of 3.

$\kappa_s = \kappa_v$	M_{PS}	$\frac{dM_{\text{PS}}}{d\kappa^{-1}}$	M_{Vec}	$\frac{dM_{\text{Vec}}}{d\kappa^{-1}}$
0.1390	0.707	1.9(4)	0.901	1.8(3)
0.1395	0.558	3.1(6)	0.786	3.0(7)
0.1398	0.476	3.0(5)	0.706	2.7(6)

function. This has an identical form to that used for the b meson (Equation 10.17), though the only remaining free parameters are the matrix elements $X_{00}^{(d)}$, $X_{01}^{(d)} = X_{10}^{(d)}$ and $X_{11}^{(d)}$ for a two exponential fit. This provided higher estimates of the ground state - ground state matrix element from the naive ratio and appears to be a better procedure than that followed for the b meson where all fit parameters were determined from both the two and three point functions. This data is given in Table 12.1 in lattice units.

In Table 12.2 we give the raw ratios (of Equation 12.7) obtained for each of the κ used as a function of lattice time. We see that the magnitude of the quantity falls off at higher time values. We interpret this as an increase in magnitude of the denominator in the ratio D_3/C arising from contamination from states propagating in the opposite time direction. This causes a dip in the function at larger times where we expect a plateau to develop. For a lattice of time extent L_4, we expect equal contributions from propagation of the meson in each direction when $t = L_4/2$, resulting in an factor 2 discrepancy in the signal which is evident. We plot these functions in Figure 12.2 scaled by $S(t)$

$$S(t) = 1 + e^{-m_\pi(L_4+2t)} \tag{12.16}$$

Table 12.2: The ratio $\frac{D_3(t)}{C(t)}$ as measured (without factors of N_f etc.).

T	$\kappa_s = 0.13900$	$\kappa = 0.13950$	$\kappa = 0.13980$
2	-0.139(14)	-0.010(28)	-0.024(41)
3	-0.157(26)	-0.160(43)	-0.199(55)
4	-0.325(43)	-0.370(63)	-0.434(70)
5	-0.470(61)	-0.573(84)	-0.642(88)
6	-0.618(82)	-0.794(110)	-0.847(113)
7	-0.723(100)	-0.963(137)	-0.995(137)
8	-0.824(121)	-1.126(165)	-1.135(161)
9	-0.858(131)	-1.221(186)	-1.202(182)
10	-0.859(136)	-1.240(197)	-1.201(197)
11	-0.730(129)	-1.051(183)	-1.029(197)
12	-0.448(115)	-0.635(166)	-0.706(199)

as well as including a factor of 2 for N_f. A plateauing behaviour can clearly be seen indicating that a region where excited state contributions are controlled.

The sign of the raw signal indicates that the disconnected loop is in fact anti-correlated with the meson correlator. That is a large vacuum quark density appears to discourage mesons from propagating in the vacuum with an associated dip in mesonic correlation functions.

We can compare these estimations of the hadronic mass dependence with finite difference data which we take from the UKQCD dynamical fermion project [62], which is also the source of the gauge configurations used in the calculation. The finite differences between meson masses should be made at fixed valence quark mass as we have asserted that the disconnected loop correlator, D_3, corresponds to $\frac{dM}{d\kappa_s^{-1}}|_{\kappa_v}$. The UKQCD measurements provide values of $\frac{\Delta M}{\Delta \kappa^{-1}}$ which are given in Table 12.3. These values are obtained by averaging the finite differences between κ_s taken

Figure 12.2: Plateauing behaviour of $\frac{dM_{\mathrm{PS}}}{d\kappa^{-1}}$ from the ratio, $N_f S(t) D_3(t, t/2)/C(t)$ for the pseudoscalar meson.

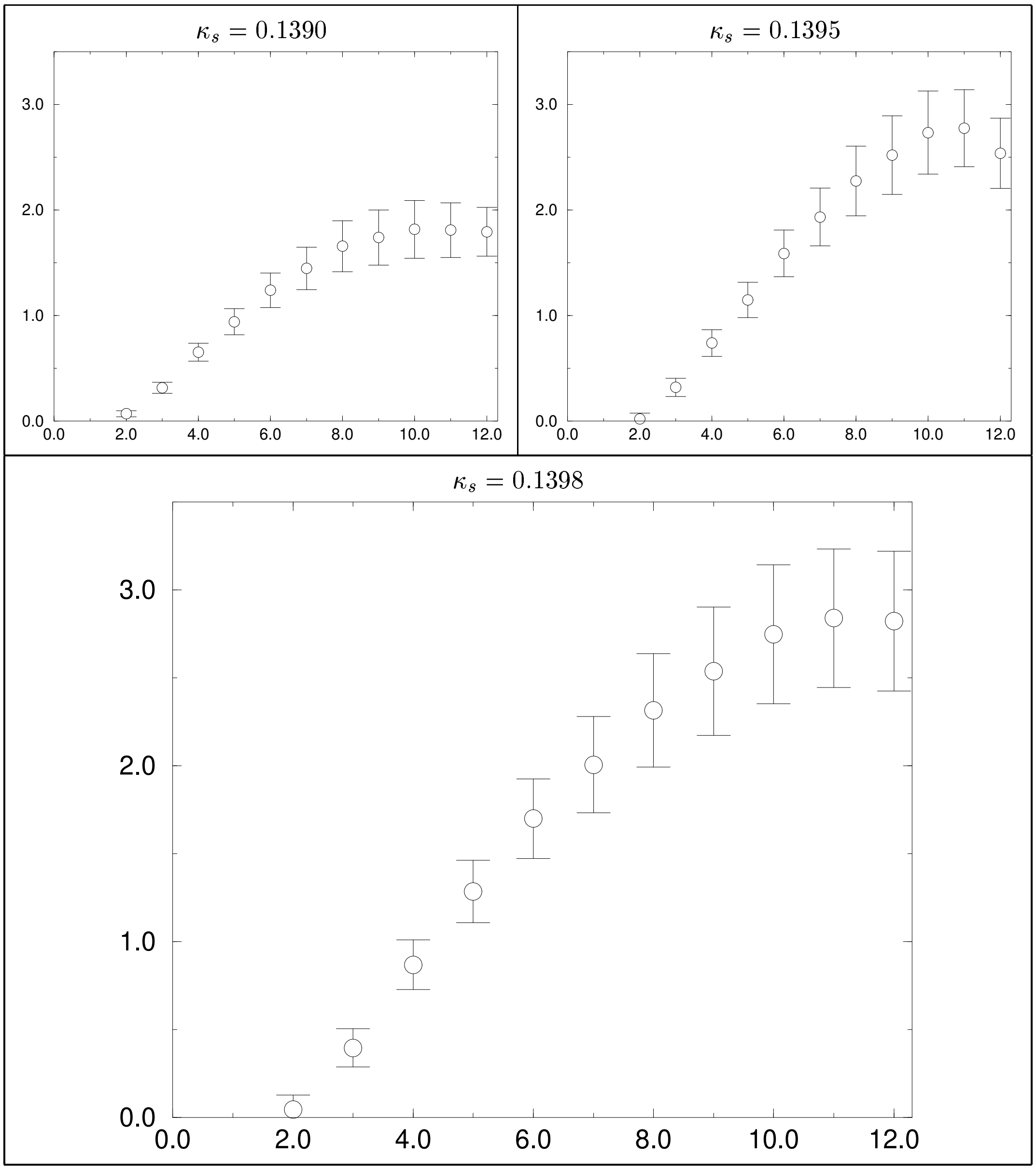

Table 12.3: Finite difference estimates of $\frac{dM}{d\kappa_s^{-1}}$.

κ_s	$\frac{\Delta M_{\rm PS}}{\Delta \kappa_s^{-1}}$	$\frac{\Delta M_{\rm PS}}{\Delta \kappa_s^{-1}}$	$r_0(a)$
0.1390	3.1(1)	3.4(5)	3.05(6)
0.1395	4.3(4)	4.0(1.2)	3.44(5)
0.1398	4.5(5)	-	3.65(3)

higher and lower than that of the measured three point function. The available κ_v are at 0.1390, 0.1395, 0.1398 for each κ_s, except for $\kappa_s = 0.1398$ with $\kappa_v < 0.1398$. For these latter cases data from $16^3 \times 24$ lattices is considered. No finite size effects have been observed between these volumes.

Our determinations of the quantities appear to be slightly low in all three cases by a factor of around 1.5 (or two standard deviations in the errors). So far we have only considered quantities in lattice units, which is appropriate, as we have applied the derivative to a discretised path integral and as such the sum rule is valid for the comparison of lattice observables, that is finite volume and lattice spacing errors should not feature in the calculation. We have used a smaller sample of gauge configurations to that on which the hadron masses were determined. It would seem that statistical fluctuations could be responsible for the discrepancy though it would be remarkable if the deviations were so similar on all three datasets. A higher statistics calculation may shed light on this. Other factors, such as the normalisation of the chiral condensate could also produce such a discrepancy, though these have been thoroughly checked against other measurements. Any incorrect normalisation of the meson propagator should cancel in the measured quantities.

We observe that the meson masses appear to depend rather strongly on κ_s, evident from both the finite differences, and our determinations of $\frac{dM}{d\kappa_s^{-1}}$. This however is somewhat misleading. Though the *lattice* masses vary quite strongly with κ_s, dimensionless ratios of lattice quantities

Table 12.4: The matrix element, $\frac{dM}{d\kappa^{-1}}$ in $N_f = 0$ Quenched QCD, $\beta = 5.7$. A factor of 2 is included to allow direct comparison with the $N_f = 2$ data in Table 12.1

κ_v	No. of Lattices	Ind.(tot.) Z_2 Samples	$M_{\rm PS}$	$\frac{dM_{\rm PS}}{d\kappa^{-1}}$
0.13843	20	16(32)	0.736	0.9(2)
0.14077	20	16(32)	0.529	1.2(4)

exhibit much smaller changes. The effect of dynamical fermions is primarily a renormalisation of the lattice spacing a, which is of course also an observable of the system. This is evident from the differing values of $r_0(a)$ corresponding to different κ_s at fixed β. The values of $r_0(a)$ are given in Table 12.3 and a more comprehensive discussion of this is given in [62], together with a plot of these quantities over a larger range of κ, whence these values.

The same correlation functions can be calculated in quenched QCD, though the interpretation of the result is ambiguous. It is interesting to determine whether a dynamical gauge configuration ensemble can be distinguished from a quenched one, that is, whether the vacuum quarks contribute to the spectrum. This has been performed using quenched lattices at $\beta = 5.7$. The same quantity as given in Table 12.1 is presented in Table 12.4 for these quenched gauge configurations.

It can be seen that these results are notably lower than those calculated in dynamical simulations. These results do infer that there are some distinctions between the quenched and dynamical gauges studied. r_0 at this lattice spacing is around 2.9 (see Table 8.3) indicating that the lattice spacing at $\beta = 5.7$ is slightly larger than any of the dynamical lattices we have studied together with different $O(a)$ corrections. However, the dynamical configurations with $\kappa_s = 0.1390$ are reasonably closely matched, both in lattice spacing, and in the ratio M_P/M_V. The fitted measurements of the ratio $2D_3/C$ is plotted in Figure 12.3 to illustrate the large difference in this quantity between the two types of configuration. We suggest that the calculation should be repeated on quenched gauges with simulation parameters tuned to match the lattice spacing

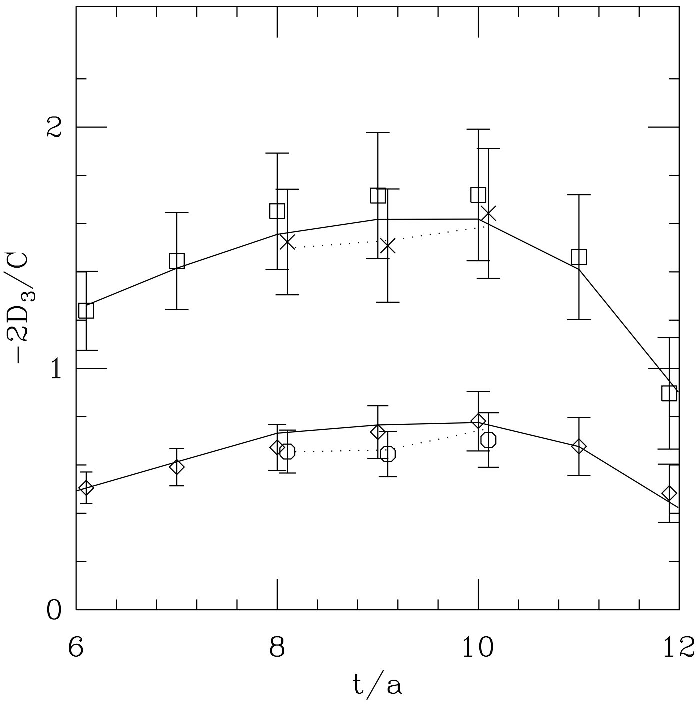

Figure 12.3: Contrast of the quantity $-2D_3/C$ between quenched (lower), and dynamical (upper) gauge configurations at similar (though not identical) physical lattice spacing. Also shown are fits made to the given quantity using symmetric(solid) and asymmetric(dotted) placement of the correlated disconnected loop.

and corrections of one of the dynamical ensembles, for example $\beta = 5.85$ which corresponds to a dynamical lattice of $\beta = 5.2$,$\kappa_s = 0.1395$, in order to explore the connection between between the quenched and dynamical cases.

We have introduced a method of determining dependence of hadronic masses under a change in the sea quark mass without resorting to generating gauges with differing simulation parameters. Our results appear to provide slightly low estimates of the derivative when compared to an existing calculation of the spectrum at the same simulation parameters and a superset of our configurations. We suggest a higher statistics calculation should be made in order to explore this discrepancy. The method also provides a method of contrasting quenched and dynamical gauges directly through the magnitude of the correlation of closed quark loops, which feature in the full QCD action, with hadron correlators. To date, little difference has been observed in the more obvious observables, such as string breaking in Wilson loops or in the η' correlation which we have discussed.

Appendix A

Γ Matrix Definitions

The Dirac matrices appear in the action for fermion fields. They are also used in the interpolating fields for spectroscopic purposes. In this work we employ a Euclidean basis for the path integral and resulting derived quantities. The Dirac matrices in a Euclidean basis are related to their Minkowski counterparts by a factor of $-i$ and the basis used in this work is given below.

$$\gamma_1 = i\begin{pmatrix} 0 & 0 & 0 & 1 \\ 0 & 0 & 1 & 0 \\ 0 & -1 & 0 & 0 \\ -1 & 0 & 0 & 0 \end{pmatrix}, \quad \gamma_2 = \begin{pmatrix} 0 & 0 & 0 & 1 \\ 0 & 0 & -1 & 0 \\ 0 & -1 & 0 & 0 \\ 1 & 0 & 0 & 0 \end{pmatrix}$$

$$\gamma_3 = i\begin{pmatrix} 0 & 0 & 1 & 0 \\ 0 & 0 & 0 & -1 \\ -1 & 0 & 0 & 0 \\ 0 & 1 & 0 & 0 \end{pmatrix}, \quad \gamma_4 = \begin{pmatrix} 1 & 0 & 0 & 0 \\ 0 & 1 & 0 & 0 \\ 0 & 0 & -1 & 0 \\ 0 & 0 & 0 & -1 \end{pmatrix} \tag{A.1}$$

and $\gamma_5 = \gamma_1\gamma_2\gamma_3\gamma_4$,

$$\gamma_5 = \begin{pmatrix} 0 & 0 & 1 & 0 \\ 0 & 0 & 0 & 1 \\ 1 & 0 & 0 & 0 \\ 0 & 1 & 0 & 0 \end{pmatrix} \tag{A.2}$$

Appendix B

Gaussian Integration

At many points in the derivation of the lattice formalism, the results of Gaussian integration over multidimensional integrals are employed. We use such results for both scalar fields, as in Chapter 6 where we use bosonic fields in the pseudofermion method, and Grassmann valued fields which are used to integrate out fermionic degrees of freedom in the partition function. Here we present simple proofs to support the various assertions in the main body of this work.

B.1 Scalar Fields

The general form of the integral which we wish to evaluate is given by the form

$$I = \int \left(\prod_{n=1}^{N} d^n x \right) e^{-\frac{1}{2} x_i M_{ij} x_j} \tag{B.1}$$

where x is an N dimensional vector and M a real symmetric matrix. We are free to make a change in variables and select that choice which diagonalises M,

$$\begin{aligned} M' &= RMR^{-1} \\ x' &= R^{-1} x \end{aligned} \tag{B.2}$$

We also must transform the integration measure, $d^N x$, this is given by the Jacobian,

$$J = \det \frac{\partial x'_i}{\partial x_j}^{-1} = \det(R)^{-1} \tag{B.3}$$

however as a unitary transformation $\det(R) = 1$. So we have

$$I = \int d^n x' e^{-\frac{1}{2}x_i^2 M'_{ii}} \tag{B.4}$$

The diagonal elements of M' are the eigenvalues of M, λ_i. If $N = 1$ the the integral is trivial and given by,

$$I_{1\times 1} = \int dx\ e^{-\frac{1}{2}\lambda x^2} = \sqrt{\frac{2\pi}{\lambda}} \tag{B.5}$$

Thus the multiple integral can be written as a product of such terms. More generally however the integral must be independent of the coordinate system and we can write,

$$I = \sqrt{\frac{(2\pi)^N}{\prod_{i=1}^N \lambda_i}} = \sqrt{\frac{(2\pi)^N}{\det M}} \tag{B.6}$$

B.2 Grassmann Fields

For fermion fields, such as the quark fields in lattice QCD, which appear with the near local quark matrix in the action, a similar approach is taken. However the fields are Grassmann valued and anticommute,

$$\{\zeta_i, \zeta_j\} = \zeta_i\zeta_j + \zeta_j\zeta_i = 0 \tag{B.7}$$

similarly for complex conjugated pairs. Thus integration over Grassmann valued variables is different,

$$\int d\zeta = 0 \quad , \quad \int d\zeta\zeta = 1 \tag{B.8}$$

The integral of interest is

$$I = \int \left(\prod_{n=1}^{N} d\zeta_n^* d\zeta_n \right) e^{-\zeta_i^* M_{ij} \zeta_j} \tag{B.9}$$

For brevity we suggest $F(M, \zeta^*, \zeta) = e^{\zeta_i^* M_{ij} \zeta_j}$. The evaluation of the integral is more complex than for the scalar case, and we roughly follow the example of Brown [63] as I feel this method give more insight into the nature of the Grassmann fields. Firstly from the anti-commuting nature of the fields we rewrite the product of measures

$$I = \left(\prod_{n=1}^{N} d\zeta_n^* d\zeta_n \right) = d\zeta_N^* \dots d\zeta_1^* d\zeta_1 \dots d\zeta_N$$
$$= d\zeta_1 \dots d\zeta_N d\zeta_{N+1} \dots d\zeta_{2N} \tag{B.10}$$

and the second line is simply a relabelling of the field variables. There are $2N!$ permutations of the ordering of these factors so that we may write.

$$\begin{aligned} I &= \int \left(\prod_{n=1}^{N} d\zeta_n^* d\zeta_n \right) F \\ &= \frac{1}{(2N)!} \epsilon_{a_1 \dots a_{2N}} \int d\zeta_{a_1}^* \dots d\zeta_{a_{2N}}^* F \end{aligned} \tag{B.11}$$

where ϵ is the totally antisymmetric Levi-Cevita tensor. As integration and differentiation of Grassmann variables is synonymous, we can write this as

$$I = \frac{1}{(2N)!} \epsilon_{a_1 \dots a_{2N}} \frac{\partial}{\partial \zeta_{a_1}} \cdots \frac{\partial}{\partial \zeta_{a_{2N}}} F \tag{B.12}$$

We now make a change of variables $\zeta_a' = R_{ba} \zeta_b$. The effect of this transformation of the derivatives is given by, $\frac{\partial}{\partial \zeta_a} = R_{ab} \frac{\partial}{\partial \zeta_b}$, so that,

$$\begin{aligned} I &= \frac{1}{(2N)!} \epsilon_{a_1 \dots a_{2N}} R_{a_1 b_1} \dots R_{a_{2N} b_{2N}} \frac{\partial}{\partial \zeta_{b_1}'} \cdots \frac{\partial}{\partial \zeta_{b_{2N}}'} F \\ &= \frac{\det(R)}{(2N)!} \epsilon_{b_1 \dots b_{2N}} \frac{\partial}{\partial \zeta_{b_1}'} \cdots \frac{\partial}{\partial \zeta_{b_{2N}}'} F \end{aligned} \tag{B.13}$$

so that $I(\zeta_a) = \det(R) I(R_{ba} \zeta_b)$. We return now to the original variables ζ, ζ^* and suggest the transform,

$$\begin{aligned} \zeta_k' &= M_{kl} \zeta_l \\ \zeta_k^{'*} &= \zeta_k^* \end{aligned} \tag{B.14}$$

suggesting that,

$$F' = e^{\zeta_k^{'*} \zeta_k'} \tag{B.15}$$

as the fields are Grassmann valued the exponent can be power series expanded and is truncated after 1 term, $e^{\zeta_k^{'*} \zeta_k'} = 1 + \zeta_k^{'*} \zeta_k'$. The integration is now (reasonably) trivial,

$$I = \int \left(\prod_{n=1}^{N} d\zeta_n^* d\zeta_n \right) e^{\zeta_i^* M_{ij} \zeta_j} = \det(M) \tag{B.16}$$

B.3 The Magic Moments

Though the above integrals give the results that we require in order to integrate out fermionic degrees of freedom in the path integral. We also require to evaluate the expectations of products of the fields from which we construct the interpolating fields for quark containing hadrons, and which we use for scalar fields in the estimation of the same quantities in the stochastic inversion method (Chapter 6).

In general we wish to evaluate integrals of the form,

$$I_N = \int \left(\prod_{n=1}^{N} d\zeta_n^* d\zeta_n \right) \zeta_{i_1}^* \zeta_{i_2} \dots \zeta_{i_{N-1}}^* \zeta_{i_N} e^{-\zeta_i^* M_{ij} \zeta_j} \tag{B.17}$$

which is the N-point function of Quantum Field Theory. The easiest way of proceeding is to add external sources to Equation B.9 to give

$$Z(\theta) = \int \left(\prod_{n=1}^{N} d\zeta_n^* d\zeta_n \right) e^{\zeta_i^* M_{ij} \zeta_j + \zeta_l^* \theta_l + \zeta_l \theta_l^*} \tag{B.18}$$

where θ are Grassmann valued parameters. This is the generating functional. We can formally complete the square in the exponent; $\zeta \to \zeta + \frac{1}{2} M^{-1} \theta$ giving

$$\begin{aligned} Z(\theta) &= \int \prod d\zeta^* d\zeta e^{\zeta_i^* M_{ij} \zeta_j + \theta_l^* M_{mn}^{-1} \theta_n} \\ &= e^{\theta_l^* M_{mn}^{-1} \theta_n} \det(M) \end{aligned} \tag{B.19}$$

We observe that Equation B.17 is generated by taking formal derivatives with respect to the source terms in Equation B.18 and setting the sources to zero;

$$\begin{aligned} I_N &= \left(\frac{\partial}{\partial \theta_{i_1}^*} \frac{\partial}{\partial \theta_{i_2}} \dots \frac{\partial}{\partial \theta_{N_2}} Z(\theta) \right)_{\theta, \theta^* = 0} \\ &= \det(M) M_{i_2 i_1}^{-1} \dots M_{N_2 N_1}^{-1} \end{aligned} \tag{B.20}$$

Appendix C

Explicit Irreducible Representations of O_h

In Chapter 9 we use operators projected into irreducible representations of the cubic group. The projection table following was employed in generating the operators and was taken from [64]. It includes parity transformations as denoted by the subscript h. The table should be used by considering a basic operator which is localised in time and a function of the fields in the spatial indices, here x, y, and z. The operator should be translated according to the each of the transformations given at the top of the table and the resulting set of objects summed with coefficients given in the body of the table for the representation of interest. Multi-dimensional representations have more than one row corresponding to each component of the representation.

Table C.1: Projection Table for the group O_h

Operator	x	y	y	-x	-x	-y	-y	x	y	z	z	-y	-y	-z	-z	y	z	x	x	-z	-z	-x	-x	z
Projection	y	x	-x	y	-y	-x	x	-y	z	y	-y	z	-z	-y	y	-z	x	z	-z	x	-x	-z	z	-x
$(x,y,z) \to$	z	-z	z	-z	z	-z	z	-z	x	-x	x	-x	x	-x	x	-x	y	-y	y	-y	y	-y	y	-y
Representation	Coefficient																							
A_1	1	1	1	1	1	1	1	1	1	1	1	1	1	1	1	1	1	1	1	1	1	1	1	1
A_2	1	-1	-1	1	1	-1	-1	1	1	-1	-1	1	1	-1	-1	1	1	-1	-1	1	1	-1	-1	1
E	0	0	0	0	0	0	0	0	1	1	1	1	1	1	1	1	-1	-1	-1	-1	-1	-1	-1	-1
	2	2	2	2	2	2	2	2	-1	-1	-1	-1	-1	-1	-1	-1	-1	-1	-1	-1	-1	-1	-1	-1
E	2	-2	-2	2	2	-2	-2	2	-1	1	1	-1	-1	1	1	-1	-1	1	1	-1	-1	1	1	-1
	0	0	0	0	0	0	0	0	1	1	1	1	1	1	1	1	1	1	1	1	1	1	1	1
T_1	1	0	0	-1	-1	0	0	1	0	0	0	0	0	0	0	0	0	1	1	0	0	-1	-1	0
	0	1	1	0	0	-1	-1	0	1	0	0	-1	-1	0	0	1	0	0	0	0	0	0	0	0
	0	0	0	0	0	0	0	0	0	1	1	0	0	-1	-1	0	1	0	0	-1	-1	0	0	1
T_1	0	1	-1	0	0	-1	1	0	0	0	0	0	0	0	0	0	1	0	0	1	-1	0	0	-1
	1	0	0	1	-1	0	0	-1	0	1	-1	0	0	-1	1	0	0	0	0	0	0	0	0	0
	0	0	0	0	0	0	0	0	1	0	0	1	-1	0	0	-1	0	1	-1	0	0	-1	1	0
T_1	0	0	0	0	0	0	0	0	1	-1	1	-1	1	-1	1	-1	0	0	0	0	0	0	0	0
	0	0	0	0	0	0	0	0	0	0	0	0	0	0	0	0	1	-1	1	-1	1	-1	1	-1
	1	-1	1	-1	1	-1	1	-1	0	0	0	0	0	0	0	0	0	0	0	0	0	0	0	0
T_2	1	1	-1	-1	1	1	-1	-1	0	0	0	0	0	0	0	0	0	0	0	0	0	0	0	0
	0	0	0	0	0	0	0	0	1	1	-1	-1	1	1	-1	-1	0	0	0	0	0	0	0	0
	0	0	0	0	0	0	0	0	0	0	0	0	0	0	0	0	1	1	-1	-1	1	1	-1	-1
T_2	0	0	0	0	0	0	0	0	0	-1	-1	0	0	1	1	0	1	0	0	-1	-1	0	0	1
	1	0	0	-1	-1	0	0	1	0	0	0	0	0	0	0	0	0	-1	-1	0	0	1	1	0
	0	-1	-1	0	0	1	1	0	1	0	0	-1	-1	0	0	1	0	0	0	0	0	0	0	0
T_2	0	0	0	0	0	0	0	0	1	0	0	1	-1	0	0	-1	0	-1	1	0	0	1	-1	0
	0	-1	1	0	0	1	-1	0	0	0	0	0	0	0	0	0	1	0	0	1	-1	0	0	-1
	1	0	0	1	-1	0	0	-1	0	-1	1	0	0	1	-1	0	0	0	0	0	0	0	0	0

Bibliography

[1] G. Zweig, Proceedings of the 4^{th} international conference on Baryon Resonances, University of Toronto Press, (1981), 439

[2] R. Feynman and A. Hibbs, Quantum Mechanics and Path Integrals, McGraw Hill (1965)

[3] E. Witten, Nucl. Phys. B156 (1979) 269
and
G. Veniziano Nucl. Phys. B159 (1979) 213

[4] G. Bali *et al.* UKQCD Collab, Phys Lett. B309 (1993)

[5] S. Weinberg, The quantum Theory of Fields, Cambridge University Press (1995)

[6] K. Osterwalder and R. Shrader, Comm Math Phys. 31 (1973) 83

[7] K. Wilson, Phys Rev D10 (1974) 2445

[8] H. Neilson and M. Niyomiya, Phys. Lett. 105B (1981) 219

[9] J. Kogut, L. Susskind, Phys. Rev. D11 (1975) 395
and
L. Susskind, Phys. Rev. D16 (1977) 3031

[10] K. Wilson, New Phenomenon and Subnuclear Physics, part A (1975)

[11] G. Lepage and P. Mackenzie, Phys. Rev. D48 (1993) 2250

[12] T. DeGrand, A. Hasenfratz, P. Hasenfratz, F. Neidermayer, Nucl. Phys B454 (1995) 587

[13] B. Sheikholeslami and R. Wohlert, Nucl Phys. B259 (1985) 572

[14] H. Shanahan *et al.* UKQCD Collab, Phys Rev D55 (1997) 1548

[15] K. Jansen *et al.* Alpha Collab, Phys Lett B372 (1996) 275
M. Luscher *et al.* Alpha Collab, Nucl Phys B478 (1996) 365
and
M. Luscher *et al.* Alpha Collab, Nucl Phys B491 (1997) 321

[16] P. Penanen and J. Peisa, Nucl. Phys. B (Proc. Suppl.) (1998) 63A-C

[17] A. Clarke and R. Disney, Probability and Random Processes, A First Course, John Wiley & Sons (1985)

[18] N. Metropolis *et al.* J. Chem. Phys. 21(1953) 1087

[19] N. Cabbibo and E. Marinari, Phys Lett. B119 (1982) 387

[20] M. Teper, Phys Lett 183B (1987) 345

[21] S. Sternberg, Group Theory and Physics, Cambridge University Press (1994)

[22] H. Rothe, Lattice Gauge Theories, An Introduction, World Scientific (1992)

[23] I. Montvay and G. Munster, Quantum Fields on a Lattice, Cambridge University Press (1994)

[24] Z. Sroczynski *et al.* UKQCD Collab. Nucl. Phys. B (Proc. Suppl.) 63 (1998) 949

[25] A. Frommer. Nucl Phys B (Proc. Suppl.) 53 (1997) 120

[26] G. deDivitiis, R Frezotti, M. Masetti, and R. Petronzio, Phys. Lett. B382 (1996) 393

[27] C. Michael and J. Peisa, hep-lat/9802015

[28] S. Dong and K. Liu, hep-lat/9308015

[29] W. Wilcox and B. Lindsay, hep-lat/9708028

[30] C. Whitney, Random Processes in Physical Systems, World Scientific Publishing, (1990)

[31] C. Michael and A. McKerrell, Phys Rev D51 (1995) 3745

[32] C. Michael, Phys Rev D49 (1994) 2616
and
C. Michael and A. McKerrell, Phys Rev D51 (1995) 3745

[33] C. Michael, Nucl. Phys. B259 (1985) 58

[34] G. Parisi, R. Petronzio, and F. Rapuano, Phys. Lett 128B (1983) 418

[35] I. Jorysz and C. Michael, Nucl. Phys. B302, (1988) 448

[36] N. Campbell, I. Jorysz and C. Michael, Phys. Lett. 167B (1986) 91

[37] C. Michael, Nucl. Phys. (Proc. Suppl.) B6 (1992) 417.

[38] M. Chanowitz and S. Sharpe, Phys Lett 126B (1983)

[39] R. Sommer, Nucl. Phys. B411 (1994) 839

[40] M. Guagnelli, R. Sommer, and H. Wittig, hep-lat/9806005

[41] A. Green, C. Michael and P. Spencer, Phys. Rev. D55 (1997) 1216.

[42] L. Griffiths, C. Michael, and P. Rakow, Phys. Lett. 129B (1983) 351

[43] S. Perantonis and C. Michael, Nucl. Phys. B347 (1990) 854.

[44] K. J. Juge, J. Kute, and C. J. Morningstar, hep-lat/9709132

[45] G. Farrar, and P. Fayed, Phys. Lett. 79B (1978) 442

[46] QCD 20 Years Later (Ed. P. Zerwas, H. Kastrup), World Scientific (1993) 505

[47] P. Lacock *et al.* UKQCD Collab, Phys. Lett. B401 (1997) 308

[48] A. De Rujula, H. Georgi, and S. Glashow, Phys. Rev. D12 (1975) 147

[49] W. Celmaster, H. Georgi, and M. Machacek, Phys. Rev. D17 (1978) 879

[50] H. P. Shanahan *et al.* UKQCD Collab, Phys. Rev. D55 (1997) 1558

[51] P. Rowland, Ph.D. Thesis, University of Edinburgh, (1998)

[52] G. de Divitiis, L. Del Debio *et al.* UKQCD Collab. hep-lat/9807032

[53] C. Michael, Nucl. Phys. B280 (1987) 13
and
C. Michael, Phys Rev D53 (1996) 4102

[54] H. Rothe, Phys. Lett. B355 (1995) 260

[55] A. Irving, J. Sexton *et al.* UKQCD Collab, Phys. Rev. D58 (1998) 114

[56] M. Foster and C. Michael, hep-lat/981021

[57] M. Fukugita, T. Kaneko and A. Ukawa, Phys. Lett. 145B (1984) 93

[58] Y. Kuramashi, M. Fukagita *et al.* Phys. Rev. Lett. 72 (1994) 3448

[59] L. Ventkataraman and G. Kilcup, hep-lat/9711006

[60] R. Frezotti, M. Masetti and R. Petronzio, hep-lat/9605044

[61] N. Eicker, U. Glassner *et al.* SESAM Collab. Phys. Lett. B389 (1996) 720,
J. Viehoff, SESAM Collab, hep-lat/9809073
and
J. Viehoff *et al.* Nucl. Phys. B (Proc. Suppl.) 63 (1998) 269

[62] C. Allton *et al.* hep-lat/9808016

[63] L. Brown, Quantum Field Theory, Cambridge University Press (1992)

[64] C. Michael, Acta Phys. Polon. B21 (1990) 119